POLITECNICO DI TORINO

TESI DI LAUREA MAGISTRALE IN INGEGNERIA AEROSPAZIALE

Numerical characterization of a supersonic ejector through RANS simulations

---

Candidato: Biagio Marco Venezia (309924)

Relatori: Prof. Gaetano Maria Di Cicca
Prof. Michele Iovieno
Prof. Miguel Alfonso Mendez

Co-relatore: Jan Van den Berghe

Tesi presentata in collaborazione con il
Von Karman Institute for Fluid Dynamics

Aprile 2025

Sommario

Gli eiettori supersonici sono dispositivi privi di parti in movimento che, grazie ai bassi costi di manutenzione e alla semplicità meccanica dei componenti, rappresentano una valida alternativa ai tradizionali compressori. La loro versatilità li rende adatti a varie applicazioni, tra le quali la refrigerazione, generazione di vuoto e sistemi di spillamento di aria. Il funzionamento dell'eiettore si basa su un flusso primario, caratterizzato da alte condizioni di ristagno, accelerato a velocità supersoniche per indurre l'aspirazione di un flusso secondario, con basse condizioni di ristagno. L'interazione tra i due flussi genera la combinazione di effetti di compressione, entrainment e miscelazione, che danno vita a fenomeni fluidodinamici complessi.

Lo studio presentato si sviluppa nel contesto del progetto EJEMOND, con l'intento di fornire una dettagliata analisi numerica (CFD) riguardo il comportamento del flusso interno all'eiettore, fornendo dati utilizzabili per il proseguo del lavoro di Jan Van de Berghe e del professore Miguel Alfonso Mendez, relativo alla definizione di modelli analitici di basso ordine.

Lo studio si pone l'obiettivo iniziale di valutare il migliore approccio per la definizione della griglia computazionale, confrontando l'approccio wall-modeled ($y^+ > 30$) con quello wall resolved ($y^+ < 5$). Dopo aver valutato il metodo che offre il miglior compromesso tra accuratezza numerica e costo computazionale, si estende la trattazione alla caratterizzazione del comportamento del flusso interno all'eiettore. Simulazioni RANS, relative ad una totalità di quattro campagne alle stesse condizioni degli esperimenti, vengono condotte utilizzando il software open-source openFOAM v9. Ogni campagna si caratterizza di un differente rapporto di pressione totale all'ingresso, permettendo l'analisi della risposta dell'eiettore a varie condizioni operative. I risultati ottenuti sono stati opportunamente esaminati per valutare l'impatto della variazione delle condizioni operative sulla topologia del flusso e sulle prestazioni dell'eiettore, supportando l'analisi numerica attraverso il confronto con i dati sperimentali.

Abstract

Supersonic ejectors are passive devices with no moving parts which, due to the low maintenance costs and mechanical simplicity of the components, represent an alternative to traditional compressors. Their versatility makes them suitable for a wide range of applications, including refrigeration, vacuum generation and bleed air systems. The functioning of the ejector is based on a primary flow, characterized by high stagnation conditions, accelerated to supersonic speeds to induce the suction of a secondary flow with low stagnation conditions. The interaction between the two streams results in a combination of compression, entrainment and mixing, which give rise to complex fluid dynamic phenomena. The presented study is conducted within the framework of the EJEMOD project, with the aim of providing a detailed numerical analysis (CFD) regarding the internal ejector flow behavior, supplying reliable data that support the ongoing research by Jan Van den Berghe and Professor Miguel Alfonso Mendez, related to the definition of low-order analytical models.

The study begins with an evaluation of the suitable meshing approach, comparing the wall-modeled ($y^+ > 30$) and the wall resolved ($y^+ < 5$) approach. After identifying the best compromise between numerical accuracy and computational cost, the investigation extends to a comprehensive characterization of the flow behavior inside the ejector. Reynolds Averaged Navier Stokes (RANS) simulations were conducted using the open-source CFD software openFOAM v9, with a total of four campaigns, matching the conditions of the experiments carried out in earlier work. Each campaign was defined by a different total inlet pressure ratio. The results assess the impact of the operating conditions on flow topology and ejector performance, supporting the numerical evaluation through a comparative analysis with the provided experimental database.

Contents

List of Figures

List of Tables

Nomenclature

Abbreviations

CAM	Constant Area Mixing
CFD	Computational Fluid Dynamics
CFL	Courant-Friedrichs-Lewy
CPM	Constant Pressure Mixing
ER	Entrainment Ratio
HAT	High Altitude Testing
LES	Large Eddy Simulation
NXP	Nozzle Exit Position
RANS	Reynolds Averaged Navier-Stokes
SED	Supersonic Ejector Diffuser
STED	Second–Throat Ejector-Diffuser
VKI	Von Karman Institute for Fluid Dynamics

Alpha-numeric symbols

β	Compound-flow parameter	$[-]$
$\underline{\boldsymbol{\tau}}$	Viscous stress tensor	[Pa]
$\underline{\boldsymbol{D}}$	Deformation gradient tensor	$[\cdot/\mathrm{t}]$
$\boldsymbol{q}$	Heat flux vector field	$\left[\mathrm{J}/(\mathrm{m}^2\ \mathrm{s})\right]$
$\boldsymbol{U}$	Velocity vector field	[m/s]
γ	Specific heat ratio	$[-]$
μ	Dynamic viscosity	[Pa s]
μ_{eff}	Effective dynamic viscosity	[Pa s]
μ_t	Turbulence or Eddy viscosity	[Pa s]
ν_t	Kinematic turbulent viscosity	$\left[\mathrm{m}^2/\mathrm{s}\right]$
ν_t	Kinematic viscosity	$\left[\mathrm{m}^2/\mathrm{s}\right]$
ω	Entrainment ratio	$[-]$
ω	Specific dissipation rate	[1/s]
ω	Turbulent dissipation	$\left[\mathrm{s}^{-1}\right]$
ρ	Density	$\left[\mathrm{Kg}/\mathrm{m}^3\right]$
τ_w	Wall shear stress	[Pa]
$\theta_{s,d}$	Secondary convergent - divergent half angle	$[^\circ]$
a_h	Thermal diffusivity	[kg/m s]
A_s	Sutherland coefficient	$\left[\mathrm{kg}\ \sqrt{\mathrm{K}}/(\mathrm{m}\ \mathrm{s})\right]$
c_p, c_v	Specific heat capacity at constant pressure/volume	[J/(K kg)]
e	Specific internal energy	[J/kg]
k	Free stream velocity	[m/s]
k	Thermal conductivity	[J/(m s K)]

k	Turbulent kinetic energy	$[\mathrm{m}^2/\mathrm{s}^2]$
L	Constant area mixing duct length	[m]
L_{tot}	Total ejector length	[m]
p^*	Sonic pressure	[Pa]
Pr_t	Turbulent Prandtl number	[−]
R	Specific gas constant	[J/(K kg)]
T_0	Stagnation temperature	[K]
T_s	Sutherland temperature	[K]
u^+	Dimensionless velocity	[−]
u_τ	Friction velocity	[m/s]
y^+	Dimensionless wall distance	[−]
$\dot{m}$	Mass flow rate	[kg/s]
A_1	Primary Nozzle exit area	$[\mathrm{m}^2]$
A_t	Primary Nozzle throat area	$[\mathrm{m}^2]$
l_m	Mixing duct length	[m]
M	Mach number	[−]
M_{eq}	Equivalent Mach number	[−]
p	Static pressure	[Pa]
p_0	Stagnation pressure	[Pa]
p_{out}	Back pressure	[Pa]
p^*_{out}	Critical back pressure	[Pa]
p^b_{out}	Breakdown back pressure	[Pa]

Operators

$\nabla(\cdot)$	Gradient
$\nabla\cdot(\cdot)$	Divergence
$\bar{\cdot}$	Time average
$\tilde{\cdot}$	Density-weighted average
$\underline{\cdot}$	Tensor
$\mathrm{tr}(\cdot)$	Trace

Subscripts

0	Reservoir condition
1	Primary stream
2	Secondary stream
d	Diffuser variables
m	Mixing duct
out	Outlet of the ejector
p	Primary stream
s	Secondary stream
t	related to turbulent variable
th	Primary nozzle throat
y	related to constant area mixing duct

1

Introduction

1.1 Context

Nowadays, industries in many sectors face increasing pressure from rising standards and regulations imposed by both governments and international associations. Among these, the predominant focus is on reducing environmental impact and fighting global warming. Companies and major industries are therefore required to develop technologies capable of complying with the limits imposed, with the additional challenge of optimizing production and maintenance costs. In this context, supersonic ejectors are emerging as technologically advanced and versatile devices, thanks to their applicability in multiple industrial sectors: from automotive, to refrigeration, up to the aerospace industry.

The supersonic ejector is a passive compression device with no moving parts. The main flow (called primary flow), characterized by high-stagnation conditions (high pressure and temperature), is accelerated to supersonic speeds through a converging or converging-diverging nozzle. This flow acts as a driving force for the secondary (low-pressure) flow, allowing intermediate pressure to be achieved through the transfer of energy and momentum. The two flows mix inside the mixing chamber, where the resulting flow is appropriately decelerated and compressed, due to phenomena such as shock waves and expansion waves, reaching intermediate conditions with respect to the inlet ones of the primary and secondary flow.

This thesis focuses in single-phase ejectors, developed within the context of the EJEMOD project (7),(8), serving as a natural continuation of Angiero's work (9) and the project conducted by Jan Van den Berghe and Professor Miguel Alfonso Mendez, with the aim of contributing to the characterization and low-order modelling of the ejector. The geometry of the ejector considered in this thesis is based on the work of Angiero, who experimentally and numerically compared a converging and a converging-diverging configuration of the

primary nozzle. A convergent-divergent configuration was adopted for this study.
After the thesis of Angiero, further experimental campaigns have been carried out and the numerical simulations need to be verified against real-life experiments. However, the high flow velocity (and consequently high Reynolds numbers) and the thin thicknesses of the boundary layer (required for a fully resolved mesh characterization with $y^+ < 5$) represent a significant computational cost. The main goal of this thesis is to find a compromise between mesh accuracy and computational cost. This will be accomplished through a comparison between fully resolved meshes ($y^+ < 5$) and wall modeled meshes ($y^+ > 30$). Once defined which mesh fits the stated requirements, subsequently, using OpenFOAM, CFD numerical simulations were conducted to characterize the internal flow and possibly propose new design concepts. The numerical campaigns refer to boundary conditions similar to those of experimental campaigns 3, 6, 7 and 8, characterized by different inlet pressure ratios and conducted by Van den Berghe. The comparison between experiments and simulations focuses on predicting the performance of the ejector and evaluating the pressure profiles for each campaign. The ultimate goal of these numerical simulations is to provide support to the validation of a 1D analytical model compatible with the operation of an ejector at supersonic speeds, already started by Jan Van den Berghe and Professor Miguel Alfonso Mendez. The structure of the thesis is organized as follows:

- **Chapter 1**: General Introduction and contextualization of the work.
- **Chapter 2**: Review of the studies conducted on the subject, with a focus on geometry, ejector operation and general characterization of internal flow under varying conditions.
- **Chapter 3**: Numerical setup of the CFD simulations in OpenFOAM, including mesh generation and mesh convergence study concerning the comparison between wall-modeled and wall-resolved approach.
- **Chapter 4**: Results, with particular attention to the variation of the internal flow according to the different campaigns and to the comparison with the available experimental data.
- **Chapter 5**: Conclusions, with a summary of the work carried out and final considerations on future prospects.

2

Literature review

2.1 Ejector details

2.1.1 Ejector applications

In recent years, interest in supersonic ejectors has grown considerably, due to their simple construction, low production costs, and no moving parts, which significantly reduces maintenance costs compared to traditional compressors.
The first studies and applications date back to the nineteenth century (10), with their use in steam engines of locomotives, while today they are used in various sectors, from **refrigeration** to **aeronautical** and **space propulsion**, up to the generation of **vacuum** and **mixing** of fluids in the chemical industry.
Vacuum generation via supersonic ejectors occurs when the secondary flow is minimized or totally blocked (zero-secondary flow ejector) (11). The transition from supercritical to subcritical regime leads to a progressive reduction of secondary pressure until vacuum is created. The application of SED (Supersonic-Ejector-Diffuser) or STED (Second–Throat ejector-diffuser) allows the achievement of extremely low pressures in the test chamber, simulating high-altitude conditions for rocket engines (HAT) (12), (13).
One of the areas in which the application of supersonic ejectors has become more widespread, replacing the traditional compressor, is **refrigeration**, thanks to the reduction of maintenance costs related to the device and the reduction of environmental impact. The operating principle of the ejector is exploited to accelerate a suitably heated flow to supersonic speed, by means of the primary nozzle, generating a low pressure area that induces the suction of the secondary flow, from the evaporator, into the mixing chamber. Once the mixing has occurred, the resulting flux is then channeled into the condenser to repeat the cycle. The main contribution of the ejector lies in the reduction of maintenance costs as it is

a passive device, and in the reduction of the environmental impact due to the demand for low-cost thermal energy to heat the primary flow (waste heat or exhaust gases, solar energy) reducing CO_2 emissions (14), (15), (16).

The study of the behavior of supersonic ejectors in **bleed-air systems** for aircrafts is covered by the **EJEMOD (Engine bleed JEt pumps continuous behaviour MODelization) project** (7). The aim of the project is to fully understand the functioning of ejectors, both in steady (on-design and off-design conditions) and transient mode, through the contribution of CFD numerical campaigns and experimental campaigns, with the aim of developing 0D/1D numerical models.

In this regard, the work reported in this thesis is not related to a specific application in the field of bleed-air systems, as it is a more general vision analysis aimed at studying the flow behavior in a single-phase ejector. This study aims to provide a substantial numerical database by conducting RANS simulations to obtain additional information regarding the internal flow field within the ejector, comparing the numerical data with the results obtained from experimental campaigns. Since the interest is to run as many simulations as possible, an assessment is made to determine whether a wall-resolved approach is necessary or whether a wall-modeled approach would be sufficient, thereby achieving a considerable computational cost saving. Furthermore, it is important to highlight that, in contrast to the works of Schillaci et al. (8) and Angiero (9), a converging-diverging geometry is chosen for for the primary nozzle.

A possible application of the supersonic ejector in the context of a bleed-air system for aircraft cabin conditioning is reported. By placing the ejector between the engine and the cabin, the hot and compressed air from the engine compressor reaches the inlet of the primary nozzle. Suitably accelerated by the primary nozzle, it generates a low-pressure area at the primary nozzle outlet that acts as suction of the secondary low-pressure flow, i.e. the air coming from the external environment. The contribution of the ejector allows for a reduction in the amount of bleed-air extracted from the engine, thereby improving its efficiency. In addition it leads to a substantial reduction in the thermal load on the air conditioning system by mixing between the bleed-air from the engine with the cold external air. Schillaci et al. (8) developed a 0D numerical model for the description of air ejectors, though their study assumes convergent primary nozzle.

2.1.2 Ejector characterisation

In this section we will proceed with the presentation of the **ejector geometry** , emphasizing in particular the interaction between the three main components: primary nozzle, secondary nozzle and mixing duct. Depending on the variation of the inlet conditions (primary and secondary stagnation conditions and back pressure), the primary and secondary flow interact differently (under-expanded or over-expanded flow), thus causing a variation in the **flow regime**. The performance of the ejector is typically evaluated as the ratio between the mass flow rate of the secondary and the mass flow rate of the primary, which strongly depends on the value of the back pressure and the ratio of the total pressures at the inlet of the two nozzles.

2.1.2.1 Ejector geometry

The design is composed of a primary nozzle, which can be presented as simply convergent or convergent-divergent. Its characteristics allow the achievement of supersonic speeds for the primary flow, generating a suction area at the nozzle outlet and driving a secondary flow introduced through a secondary nozzle. Between the two flows occurs an exchange of momentum and energy, they start mixing properly as they pass through what is known as mixing duct, generally a duct with a constant area of axisymmetric configurations. The mixed flow then passes through the diffuser, in which there is a total pressure recovery trying to match the pressure outside the outlet as much as possible.

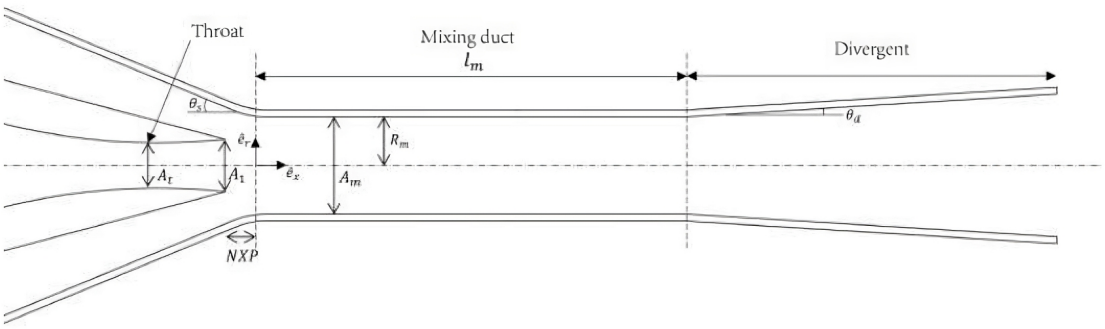

Figure 2.1: Common ejector design showing all the components (1).

Figure (2.1) represents a common ejector design, showing all the components mentioned above. As can be seen in the visualization, the **primary nozzle** is characterized by a

convergent-divergent geometry, defining the throat section with A_t and how primary nozzle outlet A_1. The geometry of the **secondary nozzle** is defined by the angle θ_s that defines the slope of the nozzle, which is the parameter that influences the introduction of the secondary flow into the mixing chamber. The mixing area is divided into the **mixing chamber** and the **mixing duct**, in which the mixing chamber is the area between the outlet of the primary nozzle and the inlet of the mixing duct. The characterization of the latter depends directly on the NXP (Nozzle exit position) parameter, i.e. the distance between the outlet of the primary nozzle and the inlet of the mixing duct, a fundamental parameter for the performance of the ejector. The subscripts in $'m'$ represent the parameters related to the mixing duct. The final part of the ejector is composed of the diffuser, characterized by θ_d that influences the recompression/expansion of the flow resulting from mixing.

From the comparison between experimental and numerical results carried out in various studies, it leaned towards the choice of a convergent-divergent geometry for the primary nozzle, identifying it as the preferred one for the acceleration of the supersonic primary flow (17). The adoption of the mixing chamber preceding the constant mixing duct was proposed by the study by Keenan et al. (18) and by Kumar et al. (19) showing the difference and the impact it has on performance compared to the normal configuration, before mixing chamber.

In this regard, the difference between **CAM (constant area mixing)** and **CPM (constant pressure mixing)** is discussed.

The **CAM** geometric configuration primarily involves in the elimination of the NXP parameter, as the outlet of the primary nozzle communicates directly with the inlet of the constant area mixing duct. The two fluids begin to interact directly in the constant-area duct, where momentum exchange between the streams occurs at variable pressure. The high velocity gradients characteristic of the two streams result in high speeds mixing, creating accentuated turbulence that leads to considerable energy dissipation. Pressure losses during mixing are considerable, increasing energy dissipation and leading to lower mixing efficiency.

The **CPM** configuration is distinguished by a greater construction complexity, essentially due to the addition of the converging mixing chamber located between the outlet of the two nozzles and the inlet of the mixing duct. In this section occurs the first interaction between the two flows, reducing the velocity difference, tending to uniform it. This enhances the entrainment of the secondary flow by the primary, reducing turbulence and

optimizing the momentum exchange. Unlike the CAM concept, the mixing occurs at constant pressure, thus reducing pressure losses and energy dissipation, resulting in a higher energy efficiency. The ability to achieve higher performance, with maximum energy efficiency, allows the CPM configuration to operate even at higher compression ratios, making it preferable for most industrial processes.

For the study proposed in this thesis, the geometry chosen is of **CPM** design.

However, the CAM configuration remains a valid alternative for simple, low-cost applications, where performance maximization is not a primary objective. On the other hand, the CPM configuration is highly sensitive to geometric errors, and its efficiency is closely related to geometric parameters, such as the shape and length of the converging mixing chamber (therefore the NXP parameter). Generally NXP is considered as the distance between primary nozzle outlet and mixing constant area duct inlet and the mixing chamber inlet is the origin of the reference system, as shown in figure (2.1).

Numerous studies have evaluated the influence of this parameter. The characterization of **NXP** (relative length and diameter) has been screened by Debroeyer et al (20) and Lamberts et al.(21), highlighting its direct impact on ejector performance. The choice of the correct geometry passes through experimental and numerical data, obtained through RANS and LES simulations, with the latter more accurate, as it guarantees a better definition of turbulent fluctuations, energy and momentum exchange. In particular, research on the balance of wall friction and shear stresses between the two flows plays a fundamental role, influencing the overall efficiency of the ejector. Working at supersonic speeds, shock-train formation is a reality, so it is necessary to evaluate the shock-boundary layer interaction with the intention of mitigating viscous dissipation. A correct choice of **NXP** and **mixing duct length (l_m)**, leads towards a maximization of the mass flow rate ratio on-design and off-design.

The effect of the mixing duct length (l_m) is investigated by Baguet et al. (1). Through simulations with Ansys Fluent, it has been observed that the increase in (l_m) defines a gain in performance counteracted by increased pressure losses mainly due to friction on the wall. In the case examined, they determined that the optimtal length of the mixing length is a compromise of effective mixing, maximization of the mass flow rate ratio, and minimization of losses due to friction on the wall. The same applies to the diffuser design, for which the shape of the angle of divergence θ_d and the length of the latter are parameters of primary interest to avoid flow separation and to reduce pressure losses caused by friction on the wall (Lamberts et al. (21)).

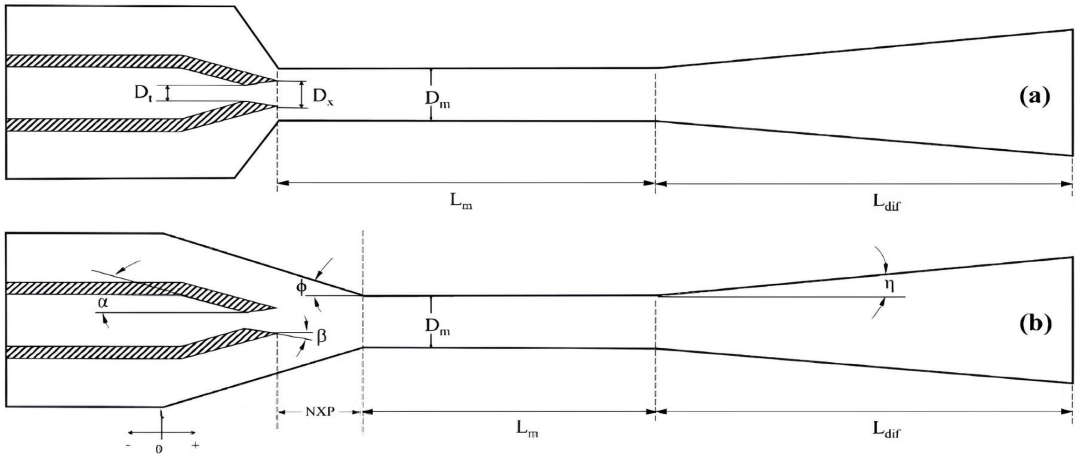

Figure 2.2: (a) Constant area mixing (CAM); (b) constant pressure mixing (CPM) (2).

2.1.2.2 Ejector operation and performance

The goal is to drive as much secondary flow as possible with minimal energy transfer and at the highest back pressure. The key parameter for performance evaluation is defined as:

$$\omega = \frac{\dot{m}_s}{\dot{m}_p} \tag{2.1}$$

The **entrainment ratio (ER)**, denoted by ω, is defined as the ratio between the secondary mass flow rate ($\dot{m}_s$) and the primary mass flow rate ($\dot{m}_p$). As discussed in Section (2.1.2.1), the variation of the NXP and the length of the mixing duct significantly influences the mixing between the two flows, thereby affecting the performance of the ejector. The operating conditions are determined by the stagnation conditions at the inlet of the two nozzles (total pressure and total temperature) and by the back pressure, which is the pressure at the outlet of the ejector.

The total pressures of the primary and secondary nozzles respectively are denoted by $p_{0,1}$ and $p_{0,2}$, the back pressure is denoted as p_{out}. Considering that at the outlet of the ejector the flow has a very low Mach, the static pressure at the outlet can be considered equivalent to the total pressure ($p_{out} \approx p_{0,out}$).

From the knowledge of these parameters, it is possible to construct the characteristic curve for the performance of the ejector based on the change in the entrainment ratio (ER) with the back pressure.

Figure (2.3) shows the characteristic curve for a fixed $\frac{p_{0,1}}{p_{0,2}}$ and presents on the x-axis the

ratio between the back pressure and the total pressure of the secondary nozzle ($\frac{p_{out}}{p_{0,2}}$), while on the y-axis the entrainment ratio defined with ω.

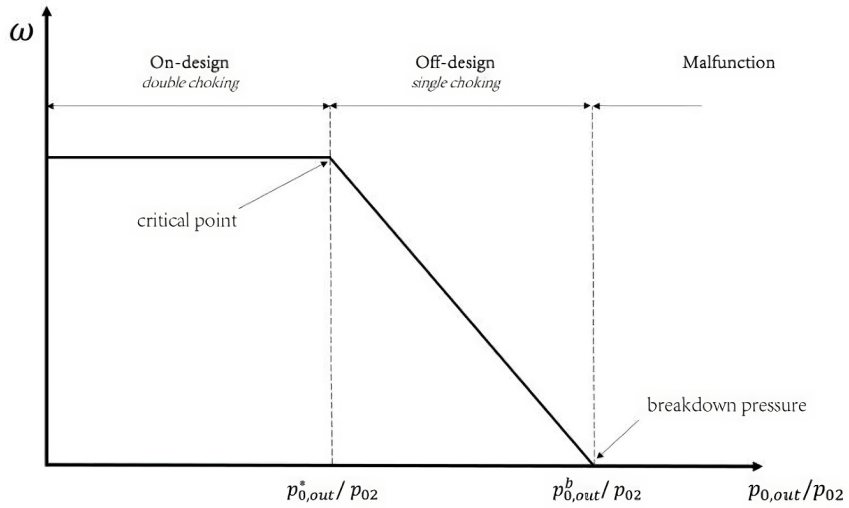

Figure 2.3: Characteristic curve of the ejector perfromance (1).

The primary nozzle is always considered to be in a choking condition, so the primary mass flow rate is maximal. The three areas of operation are defined by the variation of the secondary mass flow rate with the back pressure: the **on-design** condition, the **off-design** condition, and the region related to the **malfunction** of the ejector.

The **on-design condition** is also defined as double choking because also the secondary mass flow rate is maximal. The ratio between the mass flow rates therefore remains constant, defining the plateau of the curve that emphasizes the on-design operation, in which, as the back pressure p_{out} varies, there are no changes in the entrainment ratio.

This is true until the **critical back pressure** identified with p^*_{out}, which defines the transition from on-design to off-design operation. The improvement in performance lies precisely in the attempt to increase the value of the critical back pressure as much as possible, allowing on-design operation for a wider range of back pressure.

As specified in the previous section, a change in the length of the constant area mixing length (l_m) results in an increase in the critical back pressure and the on-design entrainment ratio. It is possible to have a similar result by changing the operating conditions at the inlet of the two nozzles (2), (22).

Figure (2.4) shows how the characteristic curve varies according to the ratio $\frac{p_{0,1}}{p_{0,2}}$.

In terms of entrainment ratio and critical back pressure, an increase in primary total pres-

sure has an opposite effect to the operating regime (on-design and off-design). In both cases, the critical back pressure increases; relative to ω, it decreases in on-design while in off-design the slope of the curve is reduced, thus increasing the value of ω. However, increasing secondary total pressure has a positive effect on performance, as it guarantees the increase in both ω and p^*_{out}.

From the figure (2.4) it can be seen that the increase in the total pressure ratio generates a shift to the right and to the bottom, hence obtaining a higher critical back pressure, but a lower entrainment ratio. it defines a clearer transition from on-design to off-design, the plateau of the on-design area is increasingly clear, and for a greater range of back pressure and the slope of the curve in off-design seems to be less pronounced. The **off-design condition** is characterized by a decreasing linear dependence of ω on $\frac{p_{out}}{p_{0,2}}$. This is because once the critical back pressure value is exceeded, the secondary nozzle is no longer choked and $\dot{m}_s$ will depend on the downstream conditions.

The rejection of the secondary mass flow rate increase as the back pressure increases until **malfunction conditions** are reached, defined by $\frac{p^b_{out}}{p_{0,2}}$ which is called the **breakdown pressure** in the figure (2.3). Under these conditions, the secondary mass flow rate reaches negative values, indicating that there is a flow reversal in the secondary nozzle.

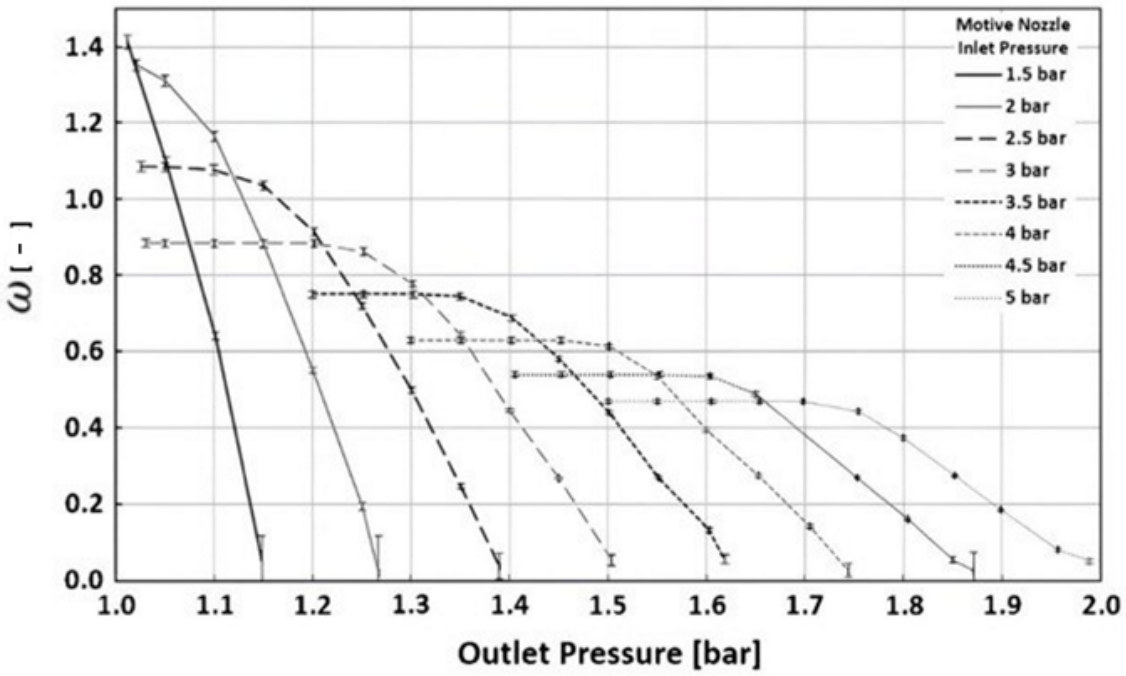

Figure 2.4: Change in performance as the $\frac{p_{0,1}}{p_{0,2}}$ ratio changes (3).

2.1.2.3 Internal ejector flow regime

In the previous paragraph, it was highlighted how the geometry and the operating conditions influence the global performance of the ejector. The global performance is directly linked to the local internal flow field, which also depends on the geometry and the operaitng condtions. A detailed understanding of the internal flow phenomena is required for optimizing the performance of ejectors. Variations in geometric parameters and/or operating conditions that occur in the ejector will cause a different interaction between the primary and induced flow, outlining different flow structures within the ducts.
Bouhanguel's doctoral thesis (4) gives a clear insight into how the flow structure can vary within two main components such as the primary nozzle and the mixing duct.
Assuming that the preferred choice regarding the geometry of the **primary nozzle** is **convergent-divergent**, it is necessary to take into account three key pressures in the specification that directly affect the flow regime inside the nozzle: the pressure at the inlet of the primary nozzle, the pressure at the outlet of the primary nozzle and the pressure of the mixing chamber.
In particular, based on the variation of the primary nozzle inlet pressure, three different flow regimes can be highlighted and shown in figure (2.5).

A) In the case of low primary nozzle inlet pressure, the flow reaches the sonic condition near the throat, continuing to increase its velocity in the diverging part. The supersonic velocity in the divergent will cause the formation of a normal shock, after which the flow will exit the primary nozzle in the subsonic regime. This condition, which allows sonic conditions to be reached in the throat but doesn't allow supersonic speeds to be maintained along the diverging section, is called the **umprimed nozzle**.

B) By increasing the primary nozzle inlet pressure, the cases of over-expanded flow and under-expanded flow are deduced. The increase in the inlet pressure of the primary nozzle allows the maintenance of a supersonic speed at the outlet of the primary nozzle. If the outlet pressure in the primary nozzle is lower than the pressure of the mixing chamber, then it will be in the case of **over-expanded flow**, characterized by the succession of oblique shocks.

C) If the output of the primary nozzle remains supersonic and with the continuous increase of the inlet pressure of the primary nozzle, in the event that the outlet

pressure of the primary nozzle reaches values higher than the pressure in the mixing chamber, then we speak of **under-expanded flow**.

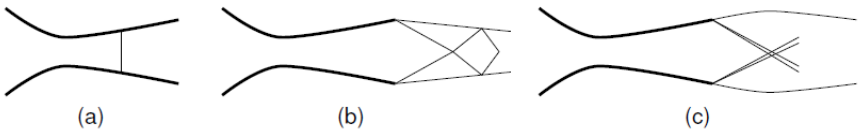

Figure 2.5: Flow structures in the primary nozzle: (a) unprimed nozzle flow; (b) over-expanded flow; (c) under-expanded flow (4).

The three previous cases have outlined how the possible flow regimes and the relative internal structure of the primary nozzle depend solely on the upstream conditions and geometry. From the analysis of the interaction between the flow coming out of the primary nozzle and the secondary flow fed into the mixing chamber by means of the secondary nozzle, it is possible to characterize the possible flow regimes that are revealed in the ejector. The interaction between the two flows is not easy to study, but is the basis of the efficiency of the ejector, defining the mode of energy and momentum exchange between the two flows.

The point of contact between the two flows, where they begin to mix, defines the so-called **shear mixing layer**, characterized by high velocity gradients and strong turbulence.

Turbulence is to be considered as one of the main factors for facilitating mixing, but at the same time it turns out to be one of the protagonists in the introduction of energy losses. The study by Matsuo et al. (23) has shown how this common layer between the two flows continues to grow, until defining in the mixing duct which is called as **critical section**, subsequently examined with the other cases of the various flow regimes.

Among the fluid dynamic phenomena that occurs there are also **shock-train** and **shock-boundary layer interaction**.

In the mixing zone, a succession of oblique shock-waves will be generated that interact with the boundary-layer and the walls of the duct, facilitating mixing but at the same time generating high- and low-pressure zones that affect the radial profile of the Mach. In the event that such interactions are quite robust, boundary-layer separation could be caused, substantially reducing the efficiency and stability of mixing.

Bouhanguel (1) refers to the study proposed by Matsuo et al. (23), defining any flow structures within the ejector (figure (2.8)):

A) FS-state (fully developed supersonic flow): It occurs for high values of primary nozzle inlet pressure and low secondary mass flow $\dot{m}_2$. The primary flow will

expand completely in the mixing chamber, pulling the secondary flow which will reach supersonic speeds.

B) CS-state (secondary choked flow): Direct consequence of the regime previously shown. In the event that the expansion of the primary flow is less pronounced and the secondary flow is sucked in larger quantities, the constant growth of the shear mixing layer defines a minimum section in the mixing duct, called as **thermodynamic throat** or **critical section** ((23), (24)). This condition defines the **choked condition** for the secondary flow, which will reach sonic speeds in this section. Subsequently, at this point, the two flows will proceed at supersonic speeds.

C) ST-state (Shock-between-throats flow or Supersonic saturated regime): The secondary flow will no longer be choked, so it remains subsonic while the primary flow maintains its supersonic regime but at lower pressure. This results in the formation of a pseudo-shock in the mixing chamber, between the outlet of the primary nozzle and the inlet of the constant area mixing duct.

D) DC-state (Doubly choked flow or Supersonic regime with double choking): In the case of ejector geometries characterized by low values of the mixing chamber section, the formation of two pseudo-shocks is observed due to the fact that the primary flow is choked both in the throat of the primary nozzle and in the throat of the ejector. The two pseudo-shocks will therefore occur immediately after the exit of the primary nozzle and the second near the diffuser inlet.

Depending on the variation of operating conditions, the internal flow within the ejector evolves in different ways, exhibiting more or less complex phenomena. As observed by Crocco (25) and confirmed by Matsuo at al. (26), the transition of the flow from supersonic to subsonic does not occur through the formation of a single normal shock wave, but through a more gradual and complex transition, essentially characterized by the succession of oblique shock waves or λ-waves. This structure is known as pseudo-shock region, which strongly depends on the duct geometry, the inlet Mach number and the thickness of the boundary layer. It essentially consists of an initial part, referred to a shock train, and a downstream region characterized by turbulent mixing, with a gradual increase in pressure. This complex shock structure is generated by the interaction between the shock wave and the boundary layer, leading to an increase in the thickness of the boundary layer, thus forming a virtual throat. The formation of this virtual throat allows for the acceleration

of the flow downstream of the first shock, thus generating a sequence of compression-acceleration of the flow.

Matsuo et al. (26) provide a clear framework of how the pseudo-shock structure can vary depending on the Mach number, which was confirmed by Weiss et al. (27) as the dominant variable for characterizing and determining the length of the shock train.

For Mach number around 2 and therefore a relatively thick boundary layer, a phenomenon known as normal shock-train is generated. It is characterized by the succession of λ-waves, essentially formed by a normal shock in the central portion of the duct (defined as pseudo-shock front in figure (2.8) which bifurcates into two oblique shocks near the wall. This typology is characteristic of case (c) and (d) of figure (2.8). For higher Mach number, what is defined as 'χ-shape' or oblique shock-train is generated. The initial oblique shock interacts with the boundary layer causing its separation, and propagates through successive areas of compression and expansion.

Generally, downstream of the shock-train, if the interaction with the boundary layer has been strong enough, a turbulent mixing zone is generated, where the flow may not be entirely subsonic.

The shock wave system characterizing the pseudo-shock causes a greater total pressure loss compared to a single normal shock, further accentuated by the turbulent mixing that occurs downstream of the shock-train. Furthermore, its presence could cause instability due to the interaction between shock waves and boundary layer, which induce irregular oscillations, as observed by Gnani et al. (28).

Matsuo et al. (23) analyzed how the variation of flow regimes within the ejector impacts its performance, providing a correlation with the ejector geometry.

The best performance is achieved in the **FS case**, with a sudden increase in the **CS case**, to be considered, however, as an optimal/ideal case that is difficult to achieve. Therefore, it is necessary to try to increase the ratio between the throat section of the ejector and the throat section of the primary nozzle ($\frac{A_m}{A_t}$) as much as possible, opting for the maximization of the secondary flow $\dot{m}_2$.

The terrible performance of the **DC case** advises to keep an eye on the relationship between the pressure of the primary inlet and the ambient pressure of the mixing chamber ($\frac{p_p}{p_m}$), since the formation of the double throttling and the two pseudo-shocks are the main cause of energy losses along the ejector.

The maximization of performance is achieved with optimal values of the cross-section ratio (increasing the secondary flow, FS/CS case) and the pressure ratio (trying to avoid the

formation of double pseudo-shocks, DC case).

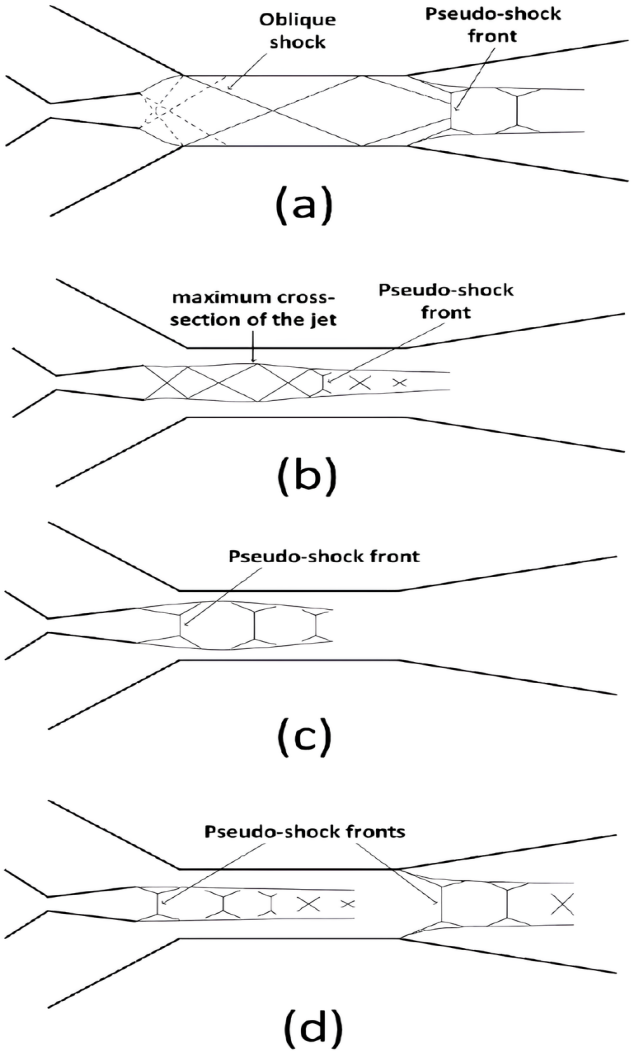

Figure 2.6: Flow structures in the ejector: (a) Fully developed supersonic flow; (b) Secondary choked flow; (c) Supersonic saturated regime; (d) Supersonic regime with double choking (2).

2.1.2.4 Choking of the secondary flow

If the study of primary flow choking has been relatively simple, a separate discussion must be introduced for the choking of the secondary flow.
The consideration of a primary nozzle of convergent-divergent geometry with supersonic velocities is characterized by the achievement of the sonic condition at the throat. The primary flow will therefore depend only on the upstream conditions and not on the downstream ones, since the signal cannot go upstream.
The interaction between the primary supersonic flow and the secondary flow generates difficulties in the study of the latter flow, increased by the formation of the shear layer, therefore strong velocity gradients and accentuated turbulence, which makes it difficult to understand the velocity and pressure profiles, and by the shock-boundary layer interaction.
In this regard, various analytical models, that explain the choking of the secondary flow with changing the upstream and downstream conditions, have been presented which are mainly based on two theories.
The **Fabri-choking theory** developed by Fabri et al. (24) and the more recent **Compound-choking theory** (6).

Fabri-choking theory

Considering the choked primary flow, at the outlet it will expand at supersonic speeds. The expansion of the primary flow and the acceleration of the secondary flow result in the formation of a minimum section in the constant area mixing duct, called **aerodynamic throat** or **hypothetical throat**.
Starting from the consideration of this aerodynamic throat, the Fabri-choking theory assumes that in that section the secondary flow reaches a sonic condition, identifying it as the starting point from which the mixing at constant pressure between the two flows begins (Huang et al. (29)).

Compound-choking theory

Bernstein et al. (30) presented for the first time an alternative theory to the Fabri-choking, for the definition of the choking condition of 2 or more flows. At the basis of the compound-choking theory lies the consideration of n streams, in the case of the supersonic ejector there will be 2, the primary and the secondary stream.
Unlike the Fabri theory, the system can be choked even if the secondary flow is subsonic, with the imperative, however, that the outflow from the mix between the two flows should

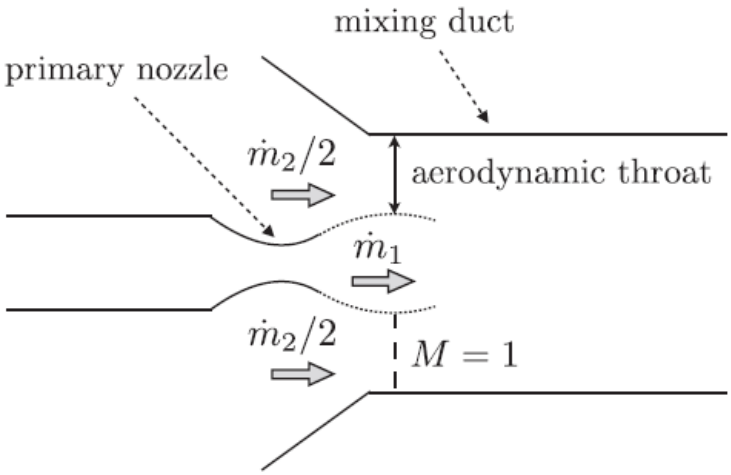

Figure 2.7: Fabri-choking model with the visualization of the aerodynamic throat (5).

be sonic.

Even this theory, however, cannot disregard necessary assumptions such as:

1. The flows in place are ideal gases, with constant thermodynamic properties.
2. One-dimensional, steady, and isentropic flows.
3. Total conditions can vary between streams, but not static conditions. As Bernstein et al. (30) define, choking can occur only at the minimum area point, the nozzle throat.

From the derivation of the compound-wave velocity, and taking into account the fact that the static pressure is constant between n streams, it is possible to define two parameters that define the choking condition, $\boldsymbol{\beta}$ and $\mathbf{M}_{\mathrm{eq}}$.

$$\boldsymbol{\beta}(\mathbf{x}) = \sum_{\mathbf{t=1}}^{\mathbf{n}} \frac{\mathbf{A_t}(\mathbf{x})}{\boldsymbol{\gamma}} \left(\frac{\mathbf{1}}{\mathbf{M_t^2}(\mathbf{x})} - \mathbf{1} \right) \tag{2.2}$$

$$\mathbf{M}_{\mathrm{eq}}(\mathbf{x}) = \left(\frac{\boldsymbol{\gamma}\,\boldsymbol{\beta}(\mathbf{x})}{\mathbf{A}(\mathbf{x})} + \mathbf{1} \right)^{\mathbf{-1/2}} \tag{2.3}$$

In fact, the value of these indicators shows the compound conditions:

$\boldsymbol{\beta} > \mathbf{0}$: Compound-subsonic flow.

$\boldsymbol{\beta} = \mathbf{0}$: Compound-sonic flow.

$\boldsymbol{\beta} < \mathbf{0}$: Compound-supersonic flow.

(Same conditions for $\mathbf{M}_{eq}$: $\mathbf{M}_{eq} < \mathbf{1}$, $\mathbf{M}_{eq} = \mathbf{1}$, $\mathbf{M}_{eq} > \mathbf{1}$).
The subscript 't' in the definition of the parameter β (formula (2.2)) represents the point at the throat, thus the throat section A_t and Mach at the throat M_t, respectively.
The main overcoming with respect to the Fabri theory lies in the fact that in order to consider the entire system as choked, it is not necessary that both flows are sonic, but if one of the two is supersonic, the other can occur in a subsonic regime, but guaranteeing the sonic condition of the mixed flow resulting between the two initial flows.

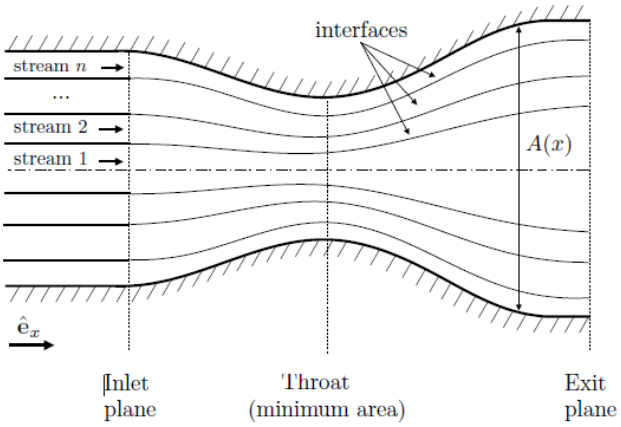

Figure 2.8: Compound-choking model with the visualization of the n streams (6).

Among the various assumptions of the two theories, some are perhaps too strong and could create problems in the real description of the phenomenon. Both theories have a limited validity due to their assumptions. The compound flow theory has been shown to be more general than the Fabri theory (31), but the assumption of uniform static pressure is too strong due to the shock trains. Furthermore, it has been observed by Lamberts et al. (5) about the Fabri-choking theory proved adequate for the description of flow behaviour for specific conditions.
It is difficult to say which of the theories best describes the solution of interest, but in this regard the various studies carried out have shown an analogy between the two theories with the pressure ratio between the pressure at the primary inlet and the pressure at the primary nozzle ($\frac{p_{0,1}}{p_{0,2}}$).
There is no direct link between the variation of the pressure ratio and the corresponding theory but, proven by the agreement between numerical and experimental results, at low pressure ratios the compound-choking theory would seem more suitable to describe the problem, while at higher values the Fabri-theory seems to achieve greater precision ((1),

(5), (29), (6)). The transition from one theory to another seems to take place at a pressure ratio $\frac{p_{0,1}}{p_{0,2}} > 5$.

In reality, this finds a physical explanation, since based mainly on the pressure value at the primary inlet there is a variation in the flow regime at the nozzle outlet and consequently in the mixing duct, an effect well identified by Lamberts et al. (5).

The characteristics of the flow inside the ejector, emphasizing the interactions between the two flows and identifying the shock waves, can be visualized with Schlieren images.

In the case of low back pressure values, it is possible to appreciate the choking condition of the secondary flow, defined as on-design condition.

High pressure values at the inlet of the primary nozzle generate a greater expansion at the outlet of the nozzle, favoring the achievement of sonic speeds for the secondary flow. The expansion waves reflect from the axis as oblique shock wave, upon contact with the shear layer, reflected as normal shock wave in the secondary flow, downstream of which the flow will proceed at a subsonic regime. The normal shock wave is then reflected once again as an oblique shock in the primary flow. The interaction between the oblique shock waves and the normal shock in the secondary generates what is called as **"Y-shock wave pattern"** (or Fabri pattern), characteristic of Fabri theory.

The Schlieren technique, which refers to the variation of density gradients, allows the formation of the "Y" pattern to be perfectly visualized (figure (2.9)), coinciding with the formation of the minimum passage section for secondary flow, i.e. the so-called aerodynamic throat.

The occurrence of this situation is a clear indication of the fact that Fabri-choking is taking place, in fact facilitating the definition of the position of the choking section, which can also be identified by observing the value of the Mach of the secondary flow, precisely when it reaches the unit value.

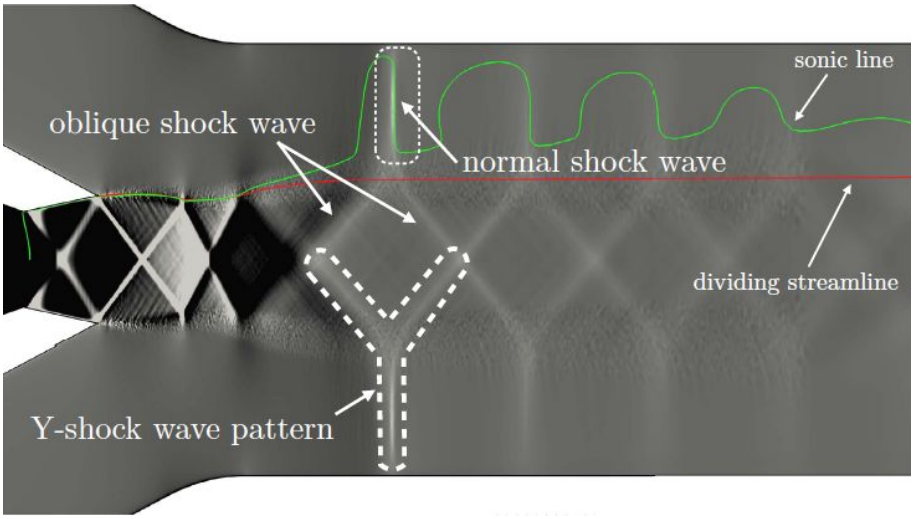

Figure 2.9: Y-shock wave pattern visualization via Schlieren imaging (5).

2.2 Turbulence modeling

2.2.1 Turbulent model

In averaging the Navier–Stokes equations (RANS) for turbulent flows, it is necessary to determine a closure model that can describe the additional terms represented by Reynolds stresses. Thanks to the turbulence model, additional equations, or closure equations, are provided, which, starting from the definition of some turbulent variables, allow the modeling of eddy viscosity. For most turbulence models, the Boussinesq hypothesis is used, with the assumption that turbulence is isotropic, which allows to represent the Reynolds stresses as directly proportional to the mean velocity gradient, determining their turbulent viscosity.

The paper by Bartosiewicz et al. (17) provides a detailed analysis of the prediction of the flow behavior inside the ejector, evaluating the use of six different turbulence models. The models were used in the case of a single flow and in the case where there was an induced secondary flow. The models with the highest performance turned out to be the $k-\varepsilon-RNG$ and the $k-\omega-SST$. The latter overcomes the limitations of the $k-\omega$ model (efficient for predicting turbulence in the boundary layer, less accurate in the wake region and outside the boundary layer), combining the $k-\varepsilon-RNG$ model with the $k-\omega$ model using a blending function F_1 (32). The use of this blending function (variable from 1 to 0) allows for a good prediction of turbulent phenomena both inside the boundary layer and outside.

The definition of turbulent kinematic viscosity (ν_t) is obtained from the ratio between k

and ω, respectively, the turbulent kinetic energy and the turbulent dissipation, determined from two additional equations. This treatment of the turbulent kinematic viscosity is valid for models such as $k-\omega$ (two-equations model), it is not for models such as Spalart-Allmaras (one-equation model).
The performance evaluation showed that both models approximate the experimental data well in all operational phases, on-design, off-design including the point of malfunction. Bartosiewicz showed that the $k-\omega-SST$ model is the most accurate for the prediction of the non-mixing length, so the description of the mixing process. This conclusion is similar to that of Mazzelli et al. (3).
From the comparison between experimental and numerical data, it has meanwhile been shown that 3D simulations are more accurate in describing off-design regimes than 2D ones. In addition, it was confirmed that the $k-\omega-SST$ model is the most efficient in the description of the flow inside the ejector, effective for supersonic flows with the presence of shock waves and adverse pressure gradients, and with a clear precision compared to the others in predicting the mass flow rate, therefore the entrainment ratio of the entire system. A detailed review of the use of various turbulence models is provided by Besagni et al. (33).
In view of what is recalled by the present studies, the $k-\omega-SST$ turbulence model has been chosen for this discussion, considered as a good closure model for the case study under consideration.

2.2.2 Wall-resolved VS wall-modeled

The treatment of turbulent flows is certainly one of the most complex challenges in computational fluid dynamics (CFD). In particular, the management of flows close to walls is a crucial aspect, since the characteristics of the boundary layer significantly influence the overall flow behavior. Turbulence models for CFD simulations have different characteristics: some, such as the Spalart-Allmaras model and the $k-\omega$ model, are particularly effective in describing the flow near the wall, but show less accuracy in the regions further out of the boundary layer. Others, such as $k-\varepsilon$, require specific treatments for the flow near the wall. In this regard, two different approaches are adopted in the generation of meshes.
The **wall-resolved** method, characterized by a high number of cells close to the wall, allows the total resolution of turbulent boundary layer. This approach requires a fine grid, $y^+ < 1$, to accurately capture the velocity gradient in the laminar sublayer.

The **wall-modeled** method uses a lower number of cells in the vicinity of the wall, describing their flow behavior with semi-empirical models, using wall functions. In this case, the values of y^+ are usually in the range of 30 and 300-500. Besagni et al. (34) provided an overview of the application of different turbulence models for CFD modeling of a supersonic ejector. The study highlights the use of two mesh configurations: a medium mesh composed of about 70,000 elements, defined as a **SWF mesh (Standard Wall Function)** with $30 < y^+ < 300$ and a fine mesh composed of about 280000 elements, which allows the resolution of the viscous sublayer $y^+ < 1$, adopting an **EWT (Enanched Wall Treatment)**. The main purpose is to balance the computational cost of numerical simulations with the reduction of grid error, optimizing the evaluation of the parameters of interest. The results show that when global quantities are evaluated, such as the entrainment ratio (ER) and local quantities such as pressure profiles, the difference between the two meshes is negligible. The medium mesh is distinguished by the already high accuracy and significantly lower computational cost than the fine mesh.
In a subsequent publication concerning the complete validation and efficiency of ejector components, Besagni et al. (33) compared a fine mesh of 645000 elements necessary to achieve grid independence and a medium mesh of 51000 elements. The wall-resolved mesh provides a better match with local experimental data, such as pressure profiles at the wall and shock waves, offering a detailed representation of phenomena in the boundary layer region. The wall-modeled mesh proves to be adequate for global analyses, providing results with an ER error less than 1%, while maintaining a low computational cost. It is therefore evident that the choice between a wall-modeled approach and a wall-resolved approach depends on the specific objectives of the analysis. If the priority is capture the velocity gradient in the viscous region, resolving the turbulent dynamics near the wall, a fine mesh with $y^+ < 1$ is the optimal choice. However, given the direct relationship between the number of nodes and the Reynolds number, the use of a fine mesh is only sustainable for low Reynolds streams; otherwise, the computational cost becomes prohibitive (35). In case the main interest is to outline the global parameters, estimating the turbulent dynamics at the wall with models, a coarser mesh characterized by a lower number of cells on the wall ($30 < y^+ < 300 \div 500$) could be the best choice, guaranteeing a considerable reduction in terms of computational cost. Other studies, such as those by Croquer et al. (36) and Han et al. (37), confirm that the marginal gain in accuracy offered by a wall-resolved mesh does not always justify the associated high computational cost. In particular, the wall-modeled mesh was preferable for extended numerical campaigns, conducted as operating conditions

changed, providing consistent results in terms of ER, wall pressure profiles, and distribution of the Mach number along the central axis.
In the case study presented in this thesis, meshes with different degrees of refinement will be evaluated (3.2.2), with the aim of defining a configuration capable of accurately representing the characteristics of the flow inside the ejector, while minimizing the computational cost, similarly to what was carried out by the previous studies. The identified optimal mesh will be used for the conduct of subsequent numerical campaigns.

3

Numerical analysis

This chapter state the numerical characterization of the ejector, achieved through the use of unsteady RANS simulations. Initially, are briefly recalled the Navier-Stokes and the compressible Reynolds-Averaged Navier-Stokes (RANS) equations. Moving on to the meshing phase, the different wall refinement strategies developed for the definition of wall-modeled meshes and wall-resolved meshes are described in detail. The resulting ranges of y^+ at the walls are therefore reported.

In the pre-processing phase, the solver and the computational model used to perform the simulations are introduced, with particular attention to the fluid properties and the boundary conditions imposed on the patches.

In order to assess which mesh achieves a numerical accuracy while ensuring a substantial reduction in computational cost, key parameters such as velocity profiles, Mach number distribution at the center-line, relative error of mass flow rates and computational cost are analyzed. The dedicated mesh convergence study section reports the evaluation of these parameters, identifying the selected mesh for conducting the entire numerical campaign. For the numerical analysis reported by this study, the open source OpenFOAM v9 free software is used.

OpenFoam uses the **finite-volume method (FVM)** for the solution of Navier-Stokes equations, discretizing the flow domain in a finite number of control cells, applying the conservation of fluid dynamic physical quantities to the centroid of each cell. FVM is preferred for the solution of large sets of differential equations associated with complex flows because of the easy management of complex boundary conditions and the relatively low computational cost (38), (39).

The solver used is the unsteady compressible-density-based flow solver ***swirllessRhoCentralFoam***, derived from the original *rhoCentralFoam*. The difference lies that the adapted

solver does not solve for the velocity in the tangential ($'z'$) direction, which remains equal to zero ($u_z = 0$), ensuring no-swirl.(31). It is a solver for compressible flows, based on Kurganov-Tadmor central-upwind schemes (40). It is suitable for the simulation of supersonic flows, with the ability to capture shock waves, expansions, flow discontinuities, and shock-boundary layer interactions (41).

3.1 Compressible RANS equations

The fundamental equations that govern the motion of fluids are based on the 3 principles of conservation of physics. From the consideration of viscous stresses and heat conduction, the Navier-Stokes equations in Eulerian frame of reference can be introduced.

- **Conservation of mass**
  Conservation of the mass of a fluid.

$$\frac{\partial \rho}{\partial t} + \nabla \cdot (\rho \mathbf{U}) = 0 \tag{3.1}$$

  where ρ represents the mass density, $\mathbf{U}$ is the velocity vector of the fluid.

- **Conservation of momentum**
  Conservation of momentum, or Newton's second law, defines that the change in the momentum of a fluid is equal to the sum of the forces acting on it.

$$\frac{\partial (\rho \mathbf{U})}{\partial t} + \nabla \cdot (\rho \mathbf{U}\mathbf{U}) = -\nabla p + \nabla \cdot \underline{\boldsymbol{\tau}} \tag{3.2}$$

  denoting the pressure by p and the viscous stress tensor with $\underline{\boldsymbol{\tau}}$.
  Following the characteristic hypothesis of Newtonian fluids, the viscous stresses are proportional to deformation rates.

$$\underline{\boldsymbol{\tau}} = 2\mu \underline{\boldsymbol{D}} + \boldsymbol{\lambda}(\boldsymbol{\nabla} \cdot \boldsymbol{U})\underline{\boldsymbol{I}} \tag{3.3}$$

  The correlation between dynamic viscosity μ and λ can be represented by the relation $\boldsymbol{\lambda} = \mu_{bulk} - \frac{2}{3}\mu$, where μ_{bulk} is the volume viscosity that exhibits a damping factor for fluid expansion. Considering the simplification deriving from Stokes' hypothesis,

in which $\mu_{bulk} = 0$, the equation is rewritten in the following way.

$$\boldsymbol{\lambda} = -\frac{2}{3}\mu \tag{3.4}$$

With the addition of Stokes' hypothesis, the viscous stress tensor $\underline{\boldsymbol{\tau}}$ is defined as follow:

$$\underline{\boldsymbol{\tau}} = 2\mu\underline{\boldsymbol{D}} - \frac{2}{3}\mu(\nabla \cdot \boldsymbol{U})\boldsymbol{I} = 2\mu\left[\underline{\boldsymbol{D}} - \frac{1}{3}(\nabla \cdot \boldsymbol{U})\boldsymbol{I}\right] \tag{3.5}$$

where $\boldsymbol{D}$ is the deformation gradient tensor, defined as $\underline{\boldsymbol{D}} = \frac{1}{2}\left[\nabla\boldsymbol{U} + (\nabla\boldsymbol{U})^T\right]$ and $\mathrm{tr}(\underline{\boldsymbol{D}}) = (\nabla \cdot \boldsymbol{U})$.

- **Conservation of energy**

  Conservation of energy, or first law of thermodynamics, defines that the change in energy is equal to the sum of the heat added and the work done on the particle.

$$\frac{\partial(\rho E)}{\partial t} + \nabla \cdot [\mathbf{U}(\rho E)] + \nabla \cdot \boldsymbol{q} + \nabla \cdot [(p\mathbf{I} - \underline{\boldsymbol{\tau}})U)] = 0 \tag{3.6}$$

  where E, defined as $E = e + \frac{1}{2}|\mathbf{U}|^2$, is the total energy per unit mass, e is the specific internal energy and $\mathbf{I}$ is the unit tensor.

  The flux of heat $\boldsymbol{q}$ can be defined as a function of the thermal conductivity k and the temperature T, using the Fourier's law.

$$\boldsymbol{q} = -k\nabla\mathbf{T} \tag{3.7}$$

RANS

The **RANS (Reynold-averaged-Navier-Stokes)** equations are partial differential equations derived from the NS equations. They describe the mean flow behavior, characterizing the fluid variables into an average component and a component that account for turbulent fluctuations.
There are two methods for defining the mean flow variables, the time-average method and the so-called Favre's average, i.e. a density-weighted average. The discussion below will take into account Favre's density-weigthed averages.
A generic variable f is defined, that can be divided into a mean component $\tilde{f}$ and a second component that identifies the relative fluctuations f''.

$$f = \tilde{f} + f'' \tag{3.8}$$

The mean component, expressed as Favre's density-weigthed average, is written as:

$$\tilde{f} = \frac{\overline{\rho f}}{\overline{\rho}} \tag{3.9}$$

The mean quantities conservation equations are written below in terms of Favre's density-weighted average (42):

- **Conservation of mass**

$$\frac{\partial \bar{\rho}}{\partial t} + \nabla \cdot (\bar{\rho}\tilde{\mathbf{U}}) = 0 \tag{3.10}$$

- **Conservation of momentum**

$$\frac{\partial(\bar{\rho}\tilde{\boldsymbol{U}})}{\partial t} + \nabla \cdot \left[\tilde{\mathbf{U}}(\bar{\rho}\tilde{\mathbf{U}})\right] + \nabla p - \nabla \cdot (\underline{\boldsymbol{\tau}} + \underline{\boldsymbol{\tau_t}}) = 0 \tag{3.11}$$

The so-called Reynolds stress tensor $\boldsymbol{\tau_t}$ identifies the contribution of turbulence. In this regard, the Boussinesq approximation for the modeling of the turbulent stress tensor is introduced (43). Boussinesq defines the turbulent stress tensor as function of the turbulent dynamic viscosity μ_t, outlining an effective viscosity μ_{eff} as the sum of the dynamic viscosity and the turbulent viscosity.

$$\mu_{eff} = \mu + \mu_t \tag{3.12}$$

Using Favre's density-weigthed average, the turbulent stress tensor takes the following form:

$$\underline{\boldsymbol{\tau_t}} \approx 2\mu_t \underline{\tilde{\boldsymbol{D}}} - \frac{2}{3}\mu_t(\nabla \cdot \tilde{\boldsymbol{U}})\boldsymbol{I} - \frac{2}{3}\overline{\rho}k\boldsymbol{I} \tag{3.13}$$

Where $\underline{\tilde{\boldsymbol{D}}}$ is the mean deformation gradient tensor and k represents the turbulence kinetic energy.

- **Conservation of energy**

$$\frac{\partial(\overline{\rho}\tilde{E})}{\partial t} + \nabla \cdot \left[\tilde{\mathbf{U}}(\overline{\rho}\tilde{E})\right] - \nabla \cdot (\alpha_{eff} + \nabla\tilde{h}_s) + \nabla \cdot (\overline{p}\tilde{\boldsymbol{U}}) = 0 \tag{3.14}$$

where α_{eff} is the effective thermal diffusivity ($\alpha_{eff} = \alpha + \alpha_t$) and $\tilde{h}_s$ is the sensible hentalpy, defined as $\tilde{h}_s = \tilde{E} + \frac{\overline{p}}{\overline{\rho}} - \frac{1}{2}\tilde{\boldsymbol{U}} \cdot \tilde{\boldsymbol{U}}$.

From the definition of the turbulent stress tensor (3.13), the RANS equations require a closure model for the definition of the turbulent dynamic viscosity, also called eddy viscosity μ_t. That evaluation is supported by turbulence models that add additional transport equations.
The turbulence models were briefly discussed in the section [2.2.1]. In this section it has been it has been clarified how the $k - \omega - SST$ model shows itself as the one that performs best in the prediction of local flow quantities and stream mixing prediction. For the study in question, the $k-\omega-SST$ turbulence model was therefore chosen as closure model.

3.1.1 Meshing phase

The generation of meshes is performed using a Python script, providing significant advantages in defining and evaluating different cell discretization strategies near the wall. This approach offers direct control over the ejector geometry and grid discretization, allowing for precise handling of varying wall cell refinement levels by sectorizing regions of interest. By including the *import gmsh* module at the beginning of the script,mesh files in **.msh** format can be generated and converted, making them compatible with **GMSH**, a three-dimensional mesh generator (44),(45).

Before proceeding with the meshing strategies,the size of the ejector and the dimensionless length used for both x and y axes are recalled. The ejector under investigation has a total length of $L_{tot} = 0.740$ m, with the origin of the axes positioned at the primary nozzle outlet, coinciding with the inlet of the convergent mixing chamber. The dimensionless length considered for both the x and y axes is $L = 0.686$ m. This length measures the distance between the primary nozzle outlet and the ejector outlet. The constant area mixing duct starts at $x/L = 0.02$, while the diffuser inlet is located at $x/L = 0.567$.

The first meshing step involves defining the key geometric parameters of the ejector components. The external nodes in the space, representing the geometric coordinates of the device, are initially positioned and connected by oriented lines. It is crucial to ensure consistent numbering of points and correct orientation of lines, as the direction of cell progression depends on the orientation of these lines.

The adopted meshing procedure is structured as follows: initial segmentation of the mesh into six regions, definition of the physical entities and mesh files generation.

The six respectively defined regions are in brief the ejector components, so the two inlets, the mixing duct divided into a converging section and a constant-area duct, the diffuser and a junction area between the diffuser outlet and the ejector exit. Each of these regions is further divided into sub-surfaces, facilitating targeted cell progression strategies based on the area of interest.

Then we move on to the definition of physical entities, so physical surfaces are identified to assign boundary conditions according to their function.

The Python script enables the generation of .msh files in 2D, 2D axisymmetric and 3D format.

The **2D axisymmetric** file is created by defining the 2D geometry in the (x,y) plane and then extruding it by rotating $\pm 2.5°$ around the x-axis. The physical entities, so the patches specified later in OpenFOAM's boundary file, are structured as follows.

The base surface *'bottom'* lies in the (x,y) plane, the other physical surfaces are generated with the rotational extrusion around the x-axis (*'primary inlet'*, *'secondary inlet'*, *'outlet'*, *'wall'*, *'sym'* and *'top'*). The *'top'* surface represents the final extruded surface, *'top'* and *'bottom'* in fact constitute the two wedge boundaries of the axisymmetric 2D geometry. The *'sym'* entity corresponds to sirface lying on the x-axis.

Once the .msh file is generated, it is converted into an OpenFOAM-readable format using the *gmshToFoam* command, and mesh details are specified in the *constant/polyMesh* directory.

A total of four different meshes were generated and analyzed. Two meshes employ a wall-modeled approach, ensuring $y^+>30$ and the other two meshes follow a wall-resolved approach, maintaining $y^+<5$; the intended wall refinement was obtained following an iterative process. All generated meshes consist of quadrilateral cells, making them structured. The primary difference between the meshes lies in how cells are refined in the normal direction to the wall. To ensure grid uniformity across adjacent sections, thereby minimizing errors, a progressive refinement is also introduced in the x direction. This is particularly relevant at the transition from the primary nozzle outlet to the converging mixing area inlet.

To smoothly control refinement and maintain a gradual transition, Python-defined progression functions were utilized, and different progression types were applied depending on the target refinement region.

For the refinement of cells in the normal direction to the wall, the script uses an hybrid approach. Taking into account the total number of elements in the normal direction as an input parameter, an uniform region extends from the centerline to a few cells below the wall, followed by a progressive refinement in the near-wall region.

For the adaptation of adjacent regions, a special progression function along the x-direction is used, ensuring smooth transitions between regions and cell uniformity, preventing abrupt changes in grid spacing. The function adapts the cell spacing at the inlet of the next region based on the spacing at the outlet of the previous region.

The figure (3.1) illustrates the ejector geometry and twp zoomed-in view, that correspond to the medium wall-modeled mesh and the fine wall-resolved mesh. The zoomed-in view is provided to highlight differences in wall refinement and the region where the primary and secondary flows first interact.

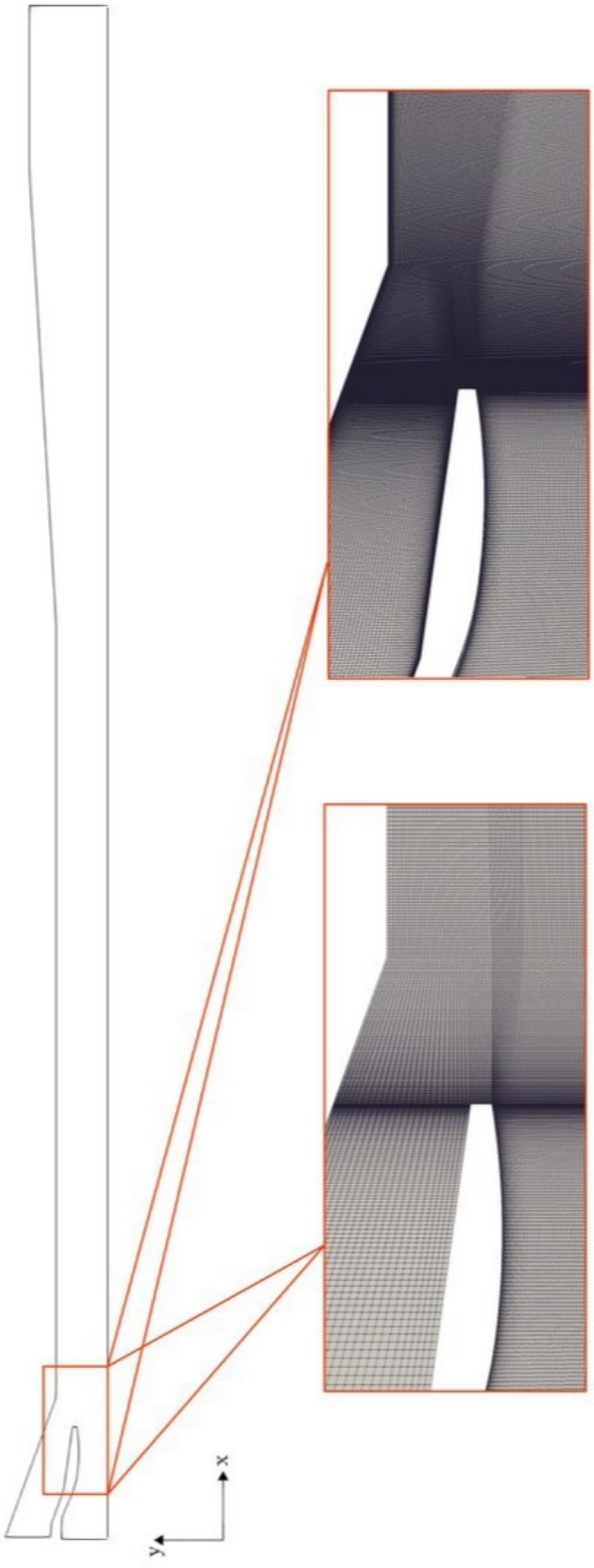

Figure 3.1: Ejector geometry and zoomed-in mesh view: (left) medium wall-modeled mesh, (right) fine wall-resolved mesh

The wall-resolved approach requires that the first wall adjacent cells lie entirely within the viscous sub-layer, which enables the accurate resolution of near wall fluid dynamics and friction forces. At the same time, this demand implies very small cell sizes near the wall, leading to higher computational cost. To balance accuracy and computational efficiency, the wall-modeled approach was also evaluated, with a wall resolution that ensures $y^+ > 30$. This method lowers computational costs, but but relies on predefined wall functions to evaluate the shear stress at the wall. The characteristics of the meshes are reported below.

Mesh	**Prim. Nozzle**		**Sec. Nozzle**		**Mixing Duct**		**N° elements**
	Nx	Ny	Nx	Ny	Nx	Ny	
Coarse	116	46	131	38	880	94	93034
Medium	195	63	132	25	1035	96	114945
Medium Res.	195	63	163	50	1081	125	155560
Fine	195	63	295	94	1883	187	392136

Table 3.1: Mesh characteristics

Table (3.1) presents the mesh configurations used in this study, detailing the distribution of elements in the different sections of the ejector.

Using the *checkMesh* command in OpenFOAM, a thorough analysis of mesh quality can be performed. This includes extracting details about the composition of the mesh elements (in this case, all meshes consist of 99% hexahedral cells) and, more importantly, evaluating critical parameters such as maximum aspect ratio and non-orthogonality levels. These factors are essential to ensure the accuracy, stability, and convergence velocity of the numerical simulation.

In detail, the medium wall-modeled mesh exhibits excellent quality, with a maximum aspect ratio of 19.5, a maximum non-orthogonality of 24.5° and an average non-orthogonality of 4.39. However, the fine wall-resolved mesh shows an increase in the maximum aspect ratio to 39.4, primarily due to cell elongation in refined regions. The non-orthogonality remains relatively unchanged, with an average of 5.6. For both meshes, the maximum skewness remains below 0.65, indicating cell distortion. Generally, a skewness value below 0.9 is considered acceptable.

To analyze wall refinement, two cases from Campaign 8 [4] were considered: an on-design

case characterized by high flow velocity inside the ejector and an off-design case characterized by lower velocity conditions. Starting from the coarse mesh, regions that required higher wall refinement were identified (table (3.2)). For all subsequent meshes, wall refinement in the primary nozzle was increased, aiming to bring the y^+ range closer to 30, which is suitable for wall-modeled approaches. This region was particularly refined by choosing to maintain $y^+ > 30$, to limit the number of cells and their size, taking into account the very high velocity characteristic of this zone. A similar mesh refinement strategy for the primary nozzle area was used by Baguet et al. (1). The cell distribution in the coarse mesh shows that y^+ values in the secondary nozzle are within the buffer layer, indicating the need to improve the wall-modeled mesh (table (3.3)).
For the wall-resolved meshes, the same wall refinement was maintained in the primary nozzle, since the boundary layer in this region is laminar or weakly turbulent, making this refinement level acceptable. However, for the secondary nozzle and the mixing region, a fully resolved approach was adopted, ensuring that $y^+<5$ in this region (tables 3.4, 3.5).

Coarse	
Wall	**y^+ range [-]**
Primary nozzle	70 - 150
Secondary nozzle	10 - 20
Mixing area	30 - 100
Diffuser	25 - 40

Table 3.2: y^+ range for the Coarse wall-modeled mesh

Medium	
Wall	**y^+ range [-]**
Primary nozzle	30 - 48
Secondary nozzle	30 - 50
Mixing area	30 - 100
Diffuser	30 - 50

Table 3.3: y^+ range for the Medium wall-modeled mesh

Medium Resolved	
Wall	**y^+ range [-]**
Primary nozzle	30 - 48
Secondary nozzle	0.1 - 1
Mixing area	0.1 - 2
Diffuser	2 - 3.5

Table 3.4: y^+ range for the Medium wall-resolved mesh

Fine	
Wall	**y^+ range [-]**
Primary nozzle	30 - 48
Secondary nozzle	0.01 - 1
Mixing area	0.01 - 1
Diffuser	1 - 2

Table 3.5: y^+ range for the Fine wall-resolved mesh

Figures (3.2), (3.3) illustrate the y^+ distribution in the first cell layer at the wall of the mixing duct. The non-dimensional domain extends from the inlet of the converging mixing area to the ejector outlet. A peak in y^+ values is observed between 0.55 and 0.6, corresponding to the diffuser entrance.

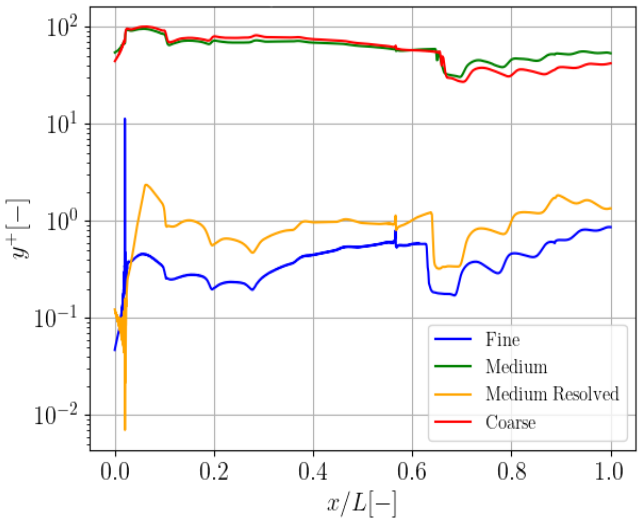

Figure 3.2: Comparison between the meshes for the y^+ values in the mixing region (Campaign number 8, on-design case with $p_{out} = 105000$ Pa)

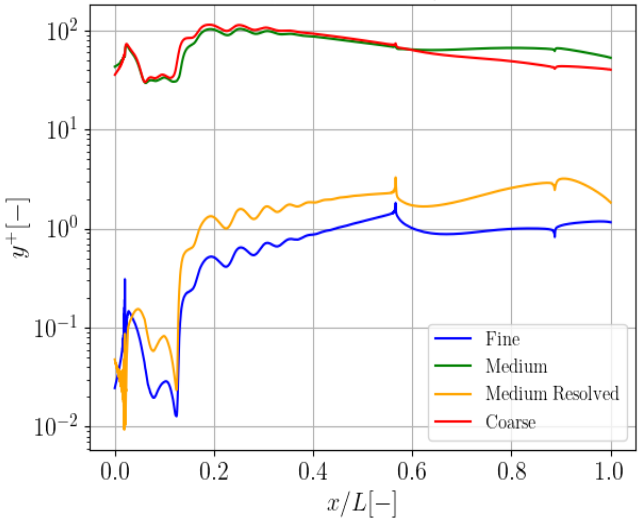

Figure 3.3: Comparison between the meshes for the y^+ values in the mixing region (Campaign number 8, off-design case with $p_{out} = 210000$ Pa)

3.2 Pre-processing

This section will reveal the pre-processing phase. Once the geometry of the component was defined, four different meshes were generated using Python scripts, converting the generated files into .msh files (GMSH). These are two pairs of meshes, two meshes based on the wall-modeled approach and two other meshes based on the wall-resolved approach, which in fact differ in a different discretisation of the cells near the wall. The mesh details, related to the two different approaches, and appropriate zoomed views of the grid, are provided in the section [3.1.1].
The choice of the optimal mesh to be used in the processing phase goes through a mesh convergence study that tries to highlight the best solution that satisfies the accuracy of the numerical results and the reduction of computational cost.

3.2.1 Solver and Computational method

As anticipated in the initial part of this chapter [3], the solver used for the production of numerical results is *swirlessrhoCentralFoam*, it enjoys the characteristics of the classic *rhoCentralFoam*, with the removal of the z-component that allows cancellation of the swirl. The details of the computational method are specified in the *system/fvSchemes* directory (46).
The solver uses the finite volume (FVM) method for meshes composed of essentially contiguous polyhedral cells, thus dividing the domain into control volumes. The alignment of the cells with respect to the system of axes can vary according to the area of interest and the faces of each cell can be characterized as internal, common to contiguous cells, or external, in which case the face belongs to the single cell and constitutes the external domain.
The FVM places the fluid dynamic quantities at the centroid of the respective control volume, and expresses the differential equations as volume integrals over the volume of the cell. For the transformation of volume integrals into surface integrals, Gauss' theorem is used, dealing with the terms of divergence and gradient, linearly interpolating the values from the centroid of the cell to the center of the faces. In this regard, in order to ensure that interpolation takes place only between neighboring cells, the choice of the flux scheme goes to the central-upwind method of Kurganov and Tadmor (40), (47). Second-order semi-discrete non-staggered schemes that guarantee stability and accuracy, avoiding oscillations in the vicinity of discontinuities, shown to be effective for capturing shock waves.
Returning to the interpolation of variables, the *fvSchemes* file specifies the linearity of the

interpolation, but combines it with the Van Leer limeter schemes for the variables (ρ, U, T) (42).
The solver in question, considering the used schemes, focuses mainly on the search for spatial accuracy; in this regard advanced methods for time integration are avoided, discretizing the time derivatives with an esplicit Euler scheme (48).

3.2.1.1 Fluid properties

The characteristics and properties of the fluid used are specified in a specific folder called ***thermophysicalProperties***. OpenFoam uses a thermophysical model that provides the thermophysical properties of the fluid as a function of pressure and temperature (49).
The ***thermophysicalProperties*** dictionary therefore provides all the details of the fluid. The thermotype sub-dictionary therefore reports the models used for the description of the system, classifying the type, the transport, the species, the equation of State, mixture and thermodynamics. The compressibility setting is done by defining the *hePsiThermo* model type as well as a compressibility-based model.
Taking into account that the fluid used is air, it is necessary to define that it is a single-phase fluid, indicating the *puremixture* model. The *mixture* subdictionary is divided into three areas, the first concerning the fluid *specie*, a second defined as *thermodynamics* and a third defined as *transport*. The details of the fluid species are indicated by the number of moles *nMoles* and the molecular weight of the air with *molWeight*.
The *thermodynamic* model is responsible for the evaluation of enthalpy and entropy, considering that the fluid in question is air, a calorically perfect gas, characterized by a constant value of the specific heat ratio $\gamma = \frac{c_p}{c_v} = 1.4$. The specific heat at constant pressure is specified as the input value $c_p = 1004.5$ J/(kg K) and the heat of formation H_f is equal to 0 J/kg as it is not a fluid obtained by a chemical reaction. The equation of state of an ideal gas is used:

$$p = \rho \, R \, T \tag{3.15}$$

R = 287.058 J/(kg K)represents the specific gas constant.
The *transport* model is specified for the evaluation of thermal diffusivity a_h, thermal conductivity k and dynamic viscosity μ; the chosen model for transport is based on Sutherland's law.

$$\mu = A_s \frac{\sqrt{T}}{1 + T_s/T} \tag{3.16}$$

The definition of the dynamic viscosity μ passes from the specification of the coefficient A_s and the Sutherland temperature T_s, for air the two coefficients have the following value: $A_s = 1.458 \cdot 10^{-6}$ and $T_s = 110.4$ K(50).

3.2.1.2 Boundary conditions

Any problem of computational fluid dynamics starts with the definition of initial and boundary conditions, which play a fundamental role in the numerical algorithm. As already announced, the meshes are defined using Python scripts that generate the .msh file that is readable in GMSH. The physical regions specified in the script and saved in the .msh file, using the *gmshToFoam* command are read by the software that generates a special file called *boundary* (*constant/polyMesh/boundary*).

The boundary file shows the different characteristic patches of the mesh in question. In the aforementioned case study these are: **primary** and **secondary inlet**, **outlet**, **wall**, **top** and **bottom**. It is necessary to assign the corresponding type to each patch; from the definition of the type of the patch the geometric or topological characteristics related to that specific area of the mesh are related.

Recalling that the meshes generated and used for numerical simulations are of the 2D axisymmetric type to reduce the computational cost, the corresponding patches of **top** and **bottom** must necessarily be assigned the *wedge* type. This type is specified in the case of two planes placed on opposite sides of the domain, ensuring the cyclic flow (using the solver *swirlessrhoCentralFoam* the component $u_z = 0$) between the two faces and the treatment of the geometry as axisymmetric and not three-dimensional. It also differs in the use of a cylindrical and non-cartesian coordinate system, characteristic of the *symmetryPlane* pacth type. In z-direction there is only one cell and the wedge angle is $\pm 2.5°$.

The patch that defines the outer **wall**, which identifies a physical or solid wall, must be identified with a boundary condition of type *wall*.

For the two **inlets** and the **outlet** there are no particular restrictions on the definition of the type of the patch, they are defined as *prim inlet*, *sec inlet* and *outlet*.

Both the two inlets and the outlet, from a geometric/structural point of view, are placed perfectly perpendicular to the x direction, and the name of the type of patches represents a reference for the direction of the flow, from left to right, entered into the inlets and expelled

from the outlet.
Once the patches have been defined in the *boundary* file, the variables to be provided as inputs must be suitably specified, which for the case in question refer to velocity, temperature, pressure, turbulent kinetic energy and specific turbulent dissipation rate. For each input variable, certain boundary conditions will be specified based on the patch of interest.

- **Velocity**

  Imposing the *ZeroGradient* condition on both the two inlets and the outlet enforces the normal velocity gradient to be zero, which means that the velocity value at the respective boundaries is directly extrapolated from the nearest inner cells.
  This imposition is quite valid in the case of accelerated flows, such as in the case of the ejector, in which the velocity is determined starting from the pressure gradient between the inlet and outlet. The use of *ZeroGradient* condition is also suggested for simulations in which a fixed pressure value is imposed on the inlet and outlet, with the speed that will adapt to the respective pressure gradient.
  The *noslip* condition is imposed on the wall for a correct simulation of viscosity and the boundary layer.

- **Temperature**

  The temperature definition uses the *fixedvalue* condition for both inlets, in which the value relative to the total temperature of both incoming flows is specified.
  The imposition of the *ZeroGradient* condition on the outlet, similar to what is stated for the velocity, allows the internal flow to determine the temperature value.
  The *ZeroGradient* condition on the wall restricts its gradient to be zero and sets the adiabatic condition to the patch.

- **Pressure**

  Unlike the previous variables, in the case in question of the ejector, characterized by the acceleration of the flow, fixed pressure values are specified at the two inlets and at the outlet. In this way, the determination of the velocity of the flow inside the

ejector and the consequent temperature distribution depend directly on the characteristic pressure gradient between the inlet and the outlet. Therefore, in conditions where the speed is not known a priori, the pressure values at the inlet and outlet are imposed as fixed, paying attention to the case in question, whether it is inflow or outflow.

In the case of inflow, not knowing the velocity value of the incoming flow a priori, the boundary type *totalpressure* is imposed. Using the total pressure formula, the simulation solution returns the velocity and static pressure values.

The boundary condition of type *totalpressure* is therefore imposed on the primary and secondary inlets, specifying its value as fixed. The mode of operation depends directly on the specification of the input values

The static pressure value at the outlet is then set, specifying the *waveTransmissive* boundary. The application of this boundary condition allows pressure waves to flow freely to the boundary, without spurious reflections (51). The behavior of the pressure at the outlet is directly influenced by the application of two key parameters, namely *fieldInf* and *lInf*.

fieldInf is the field at infinity, therefore the pressure value towards which the solution must tend to stabilize.

lInf indicates a so-called relaxation length, i.e. it ideally represents the distance after which the field adjusts to the value specified in *fieldInf*.

In general, this parameter defines how quickly the pressure value tends to approximate the value of *fieldInf*, calculating the strength of the reflecting wave. It is difficult to identify a fixed *lInf* value, as it depends on the conditions of the simulation in progress and on the characteristics of the flow inside the ejector.

However, it can be said that high values of *lInf* guarantee a considerable reduction in wave reflection but at the same time do not assign a constraint to the pressure value to which to tend, causing considerable pressure deviations.

Low values of *lInf* impose a strong constraint on the pressure value, minimizing the deviation from the value reported in *fieldInf*. At the same time, they cause an increase in wave reflection, posing a risk to the success of the simulation.

An intermediate value of *lInf* of 0.01 was chosen for the case study. For the wall, a boundary condition of the *ZeroGradient* type is reported, characteristic of impermeable walls.

- **Turbulent kinetic energy**

A condition of type *turbulentIntensityKineticEnergyInlet* is specified to both inlets, providing the value of the turbulent intensity that was chosen for the simulation of 5% (9).

$$k = 1.5\ (I|\mathbf{u}|)^2 \tag{3.17}$$

The turbulent kinetic energy is directly proportional to the turbulence intensity I and velocity.
The *ZeroGradient* condition is applied to the outlet: $dk/dx = 0$.
The condition *kLowReWallFunction* is applied to the wall, which represents a constraint to determine the turbulent kinetic energy k, based on the Reynolds number value. Specifically, the definition of turbulent kinetic energy k depends on the definition of the y^+ value, varying according to the position of the first cell near the wall, if in the viscous sub-layer or in the logarithmic region.
By evaluating the value of y^+ and y^+_{lam}, which represents the value of y^+ for which the intersection between the viscous and inertial region take place, the prediction of the value of k varies. The value is obtained from a blending function between the value defined for the viscous sub-layer k_{vis} and the value k_{log} defined for the logarithmic region. Depending on the region, different definitions and parameters are used as defaults (52).

- **Specific turbulent dissipation**

The turbulent dissipation frequency ω is defined based on different conditions depending on the specific boundary patches in the computational domain. At the primary and secondary inlets, the *turbulentMixingLengthFrequencyInlet* condition is applied. This condition defines ω as a function of the turbulent kinetic energy (k), utilizing the concept of the mixing length (L); for any inlet the mixing length is given by $L = 0.07 \cdot D$, where D represents the hydraulic diameter (43).

$$\omega = \frac{k^{0.5}}{C_\mu^{0.25}\ L} \tag{3.18}$$

The empirical constant C_μ has a predefined value of 0.09.
At the outlet, a *ZeroGradient* boundary condition is imposed, ensuring that the gradient of ω in the streamwise direction is zero: $\frac{\partial \omega}{\partial x} = 0$.
On the wall, the imposition of the *omegaWallFunction* condition allows the definition of ω as a blending between the one defined in the viscous sub-layer (ω_{vis}) and the one defined in the logarithmic layer (ω_{log}), based on the value of y^+. If $y^+ < y^+_{lam}$ the specific turbulent dissipation ω_{vis} is defined following the hyperbolic variation proposed by Wilcox (53).
Additionally, in logarithmic layer, the production of turbulent kinetic energy (G) is modeled, while it is assumed to be zero in the viscous sub-layer.

- **Other conditions**

Further conditions are defined in the 0/ directory, particularly for turbulent thermal diffusivity (α_t) and turbulent kinematic viscosity (ν_t).
Turbulent thermal diffusivity (α_t) is calculated as the ratio between the turbulent dynamic viscosity (μ_t) and the turbulent Prandtl number (Pr_t), with $\mathrm{Pr}_t = 0.85$, by imposing the condition *compressible::alphatwallfunction* on the patch wall.
The definition of the turbulent kinematic viscosity (ν_t) is governed by the *nutkWallFunction* boundary condition applied to the wall. This function incorporates key empirical coefficients, including the empirical model constant C_μ, the Von Karman constant (k) and the wall roughness parameter (E). The turbulent kinematic viscosity is computed through a blending function that interpolates between its values in the viscous sublayer and the logarithmic layer. The value of y^+ is modeled as follows (43):

$$y^+ = C_\mu^{1/4}\, y\, \frac{\sqrt{k}}{\nu_w} \tag{3.19}$$

where the parameters are set as follows: $C_\mu = 0.09$, $k = 0.41$ and $E = 9.8$.

3.2.1.3 Simulation control

As already specified above, the simulations conducted are unsteady using compressible density-based solvers, characterized by supersonic flow and the formation of complex structures such as shock waves. To ensure control and stability of the simulation, a restriction is placed on the **CFL** number by means of the **Courant-Friedrichs-Lewy** condition, attesting it to a maximum value. The CFL number is a key parameter for CFD simulations and determines the time step of the simulation, in relation to the flow velocity and the minimum grid size. Its value strictly depends on the type of simulation conducted.
In this case, in order to guarantee the numerical stability of the simulation, ensuring an appropriate propagation of pressure waves and the capture of shock waves, a maximum CFL number value of 0.5 has been defined.
These details are specified in the *system/controlDict* file, which also includes a control for the simulation time step, *adjustableRunTime*. Thanks to this option, the time step of the simulation dynamically adapts according to the flow velocity and cell dimensions, respecting the condition of maximum Courant number. For the defined meshes and, in general, in all the simulations performed, the determination of the maximum CFL≈ 0.5 defined an average time step of about $2 \cdot 10^{-8}$.
This restriction on the CFL and therefore the consequent definition of a low time step undoubtedly increase the computational cost of the simulations, but it is necessary for the stability and numerical accuracy of the simulation. It depends on the explicit solver being used; conversely the commercial code Fluent use an implicit solver that allows reaching of high CFL numbers, thus running simulations faster. As previously announced, an unsteady solver is used for the CFD calculations. To check the convergnce of the simulation, the relative error of the mass flow rates ($\varepsilon_{\dot{m}}$) between input and output has been analyzed in detail, defining the convergence if this error remained $< 0.5\%$ (9).

$$\varepsilon_{\dot{m}} = \left| \frac{\dot{m}_{\text{in}} - \dot{m}_{\text{out}}}{\dot{m}_{\text{in}}} \right| < 5 \cdot 10^{-3} \tag{3.20}$$

In particular, this is considered for cases in which there is no presence of unsteady shock in the diffuser. The simulation may not achieve complete convergence in cases with unsteady shocks in the diffuser, as pressure waves continously propagate, attempting to approach the uniform static pressure value set by the boundary conditions at the outlet. The assumption of $linf = 0.01$ might be too restrictive, resulting in strong pressure wave reflection.

3.2.2 Mesh convergence study

After introducing the different meshes in section [3.1.1], this section presents a **mesh convergence study**, which is fundamental to ensuring that the physical phenomenon is accurately represented and that simulation results are independent of mesh resolution.
The primary objective of this study is to determine the optimal mesh, striking a balance between numerical accuracy and computational efficiency, which will be used across all four numerical campaigns.
Additionally, this section will compare the wall-modeled and wall-resolved approaches, discussing their respective advantages and limitations, and justifying the choice of the most suitable approach.
For this comparison, four key parameters have been analyzed, as they are crucial for both simulation accuracy and mesh selection:

- Velocity profiles
- Mach number along the centerline
- Relative error in mass flow rate
- Computational cost

3.2.2.1 Velocity profiles

The two wall-resolved meshes maintain $y^+ < 5$ throughout most of the mixing chamber. This wall refinement allows the resolution of the boundary layer, capturing the viscous sublayer and turbulent fluctuations without the use of models. It is therefore expected that the resulting velocity profile optimally approximate the theoretical curve.
In the case of meshes with wall-modeled approach, the boundary layer is not directly solved, resorting to the use of wall functions, that rely on a loarithmic law for the approximation of the velocity profile.
The use of such functions are typical for the treatment of incompressible flows with negligible pressure gradients. The theoretical assumptions of such functions may constitute a reason for conflict in the presence of high compressibility, strong pressure gradients, or flow separation, leading to potential inaccuracies in the approximation. As a result, the computed velocity profile may deviate from the proper trend of the theoretical curve, particularly in presence of shock-induced separations and strong velocity gradients.

Figure (3.4) depicts the Mach number fields for the case in question, directly shown the two points of the domain chosen for the extraction of the speed profiles. The points were chosen because they were considered to be in areas of the domain where the separation between the two flows should no longer be evident. The following definitions are used to define dimensionless speed and dimensionless wall distance:

$$u^+ = \frac{u}{u_\tau} \tag{3.21}$$

$$y^+ = \frac{y\, u_\tau}{\nu} \tag{3.22}$$

where u_τ is defined as $u_\tau = \sqrt{\frac{\tau_w}{\rho}}$.
Figures (3.5)(3.6) show the velocity profiles at two points in the x domain, specifying the trends related to each mesh configuration. As anticipated, meshes characterized by the wall-resolved approach are able to approximate the theoretical profile, identified by the black dotted line, in a rather precise way. For wall-modeled meshes, the discrepancy between the velocity profiles of the meshes and the theoretical one is visible. The first value, attested to the first cell near the wall, is close to the theoretical profile but otherwise the curve shows a deviating trend. The reason for this behavior can be addressed in the wall function used by openFOAM. The law at the wall used for the estimation of the shear stress on the wall (3.23), for a point placed in the logarithmic layer, seems not to be completely suitable for the compressible case in question. Being directly proportional to turbulent kinetic energy, its characterization is likely to also depend on the turbulence model ($k - \omega - SST$ is recommended for $y^+ < 1$).

$$\tau_w = \rho\, C_\mu^{1/4}\, \sqrt{k}\, \frac{U_x(y)}{u^+} \tag{3.23}$$

In general, from the evaluation of the other results compared between the four meshes, the flow seems not to be very sensitive to friction on the wall.

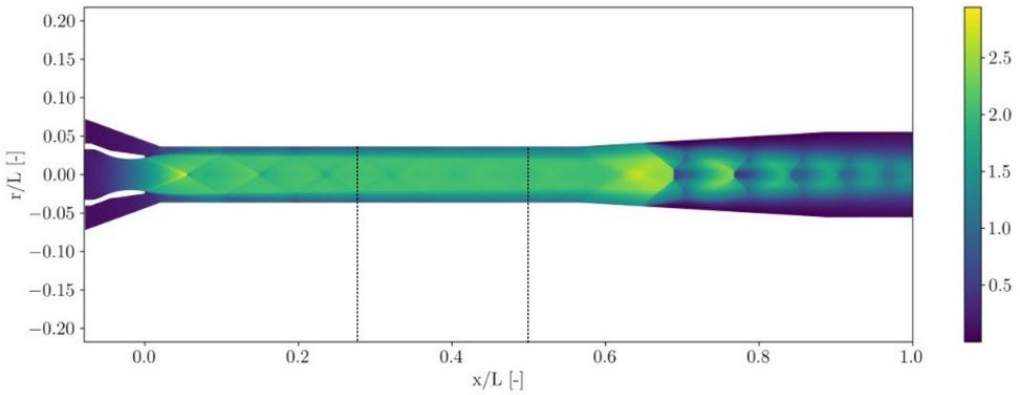

Figure 3.4: Mach field and x/L points for the velocity profile extraction (Campaign number 8, on-design case with $p_{out} = 105000$ Pa)

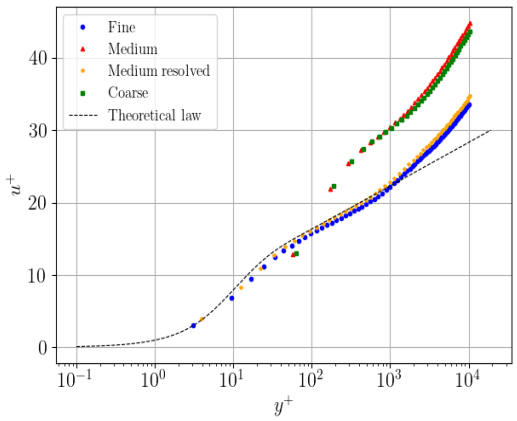

Figure 3.5: Velocity profiles for each mesh at $x/L = 0.279$ (Campaign 8, on-design case with $p_{out} = 105000$ Pa)

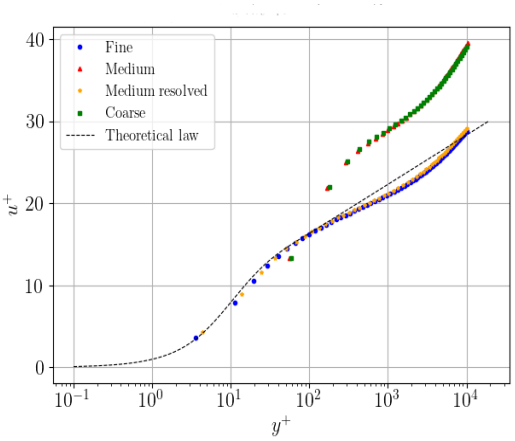

Figure 3.6: Velocity profiles for each mesh at $x/L = 0.497$ (Campaign 8, on-design case with $p_{out} = 105000$ Pa)

3.2.2.2 Center line Mach

The operating conditions of the ejector involve supersonic flow, characterized by complex flow phenomena such as shock waves and shock waves-boundary layer interactions. To evaluate whether the numerical simulation has accurately captured the density discontinuities resulting from shocks, expansions, and possible flow separations, the Mach number distribution along the centerline is examined.

The distribution of Mach number along the central line provides information about flow behavior and shock waves pattern, so significant oscillations or damping in Mach number within certain regions of the mesh may indicate insufficient refinement, suggesting the need

for further grid optimization.

The analysis of the results reveals that the Mach profiles obtained with different mesh resolutions are nearly identical, confirming that all meshes provide a sufficiently accurate representation of the Mach number gradient.

The only noticeable discrepancy occurs toward the end of the x domain for the on-design case (figure (3.7)), which is attributed to an unsteady shock in the diffuser that does not affect the overall evaluation of the mesh.

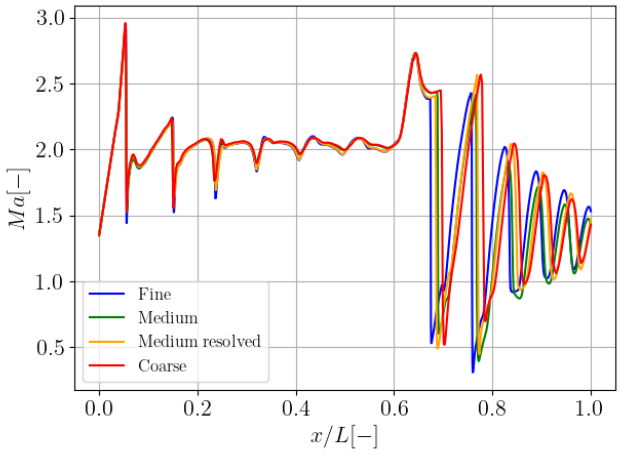

Figure 3.7: Comparison between the meshes for the Mach number (Ma) along the centerline (Campaign number 8, on-design case with $p_{out} = 105000$ Pa)

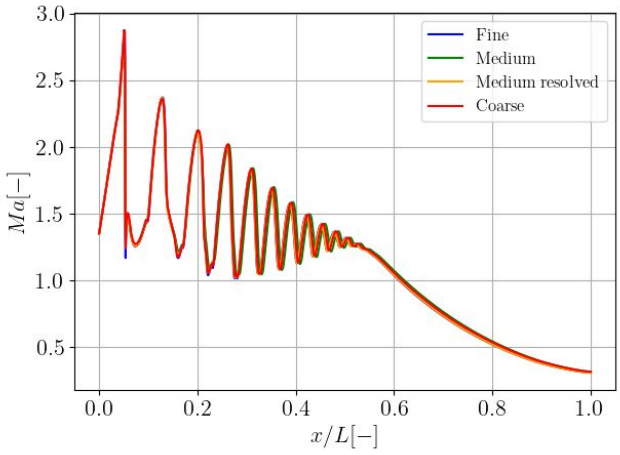

Figure 3.8: Comparison between the meshes for the Mach number (Ma) along the centerline (Campaign number 8, off-design case with $p_{out} = 210000$ Pa)

3.2.2.3 Mass flow rate relative error

The evaluation of the mass flow rate at the inlet and outlet is a fundamental parameter for verifying simulation convergence and identifying potential discretisation issues within the mesh. Once the mass flow rate conservation error between inlet and outlet has been confirmed to remain below 0.5% (section [3.2.1.3]), this section focuses specifically on the relative error associated with each mesh.

The error is calculated relative to the fine mesh, which is assumed to have the lowest grid error due to its high level of refinement.

The tables (3.6), (3.7) present the percentage errors related to the mass flow rates at the two inlets and the corresponding entrainment ratio ER.

In the on-design case, the relative errors across all meshes remain below 0.5%, indicating

Mesh	$\dot{m}_1$ **[kg/s]**	$\dot{m}_2$ **[kg/s]**	**ER [-]**	$\varepsilon_{\dot{m}_1}$ **[%]**	$\varepsilon_{\dot{m}_2}$ **[%]**	ε_{ER} **[%]**
Coarse	0.6885	0.2099	0.3048	5.2×10^{-2}	0.304	0.357
Medium	0.6888	0.2087	0.3029	5.81×10^{-4}	0.266	0.265
Medium Resolved	0.6888	0.2088	0.3032	1.45×10^{-3}	0.190	0.189
Fine	0.6888	0.2092	0.3037	0	0	0

Table 3.6: Relative error of the mass flow rates considering the mesh refinement (Campaign number 8, on-design case with $p_{out} = 105000$ Pa)

Mesh	$\dot{m}_1$ **[kg/s]**	$\dot{m}_2$ **[kg/s]**	**ER [-]**	$\varepsilon_{\dot{m}_1}$ **[%]**	$\varepsilon_{\dot{m}_2}$ **[%]**	ε_{ER} **[%]**
Coarse	0.6884	0.1645	0.2390	5.6×10^{-2}	0.715	0.772
Medium	0.6888	0.1626	0.2360	5.81×10^{-4}	0.483	0.482
Medium Resolved	0.6888	0.1612	0.2341	1.45×10^{-3}	1.309	1.308
Fine	0.6888	0.1634	0.2372	0	0	0

Table 3.7: Relative error of the mass flow rates considering the mesh refinement (Campaign number 8, off-design case with $p_{out} = 210000$ Pa)

that even coarser meshes provide a sufficiently accurate approximation of the internal flow behavior of the ejector.

In the off-design case, an increase in relative error is observed across all mesh configurations.

In particular, the medium wall-resolved mesh shows an anomalous deviation, diverging from the convergent trend observed in the on-design case. Overall, the medium wall-modeled mesh shows excellent accuracy in determining the mass flow rate, with a lower relative error compared to other meshes, maintained below 0.5%, and achieving results very close to those of the fine mesh, although it has a significantly lower number of elements.

3.2.2.4 Computational cost

After evaluating how well the different meshes approximate the internal flow characteristics of the ejector, it is essential to balance accuracy with computational efficiency. The computational cost is closely tied to the total number of mesh elements and the level of refinement near the walls.

The increased computational cost is primarily due to the highly refined cells near the walls, particularly in the wall-resolved meshes. Wall-resolved approaches require significantly smaller cells, leading to an exponential increase in computation time compared to wall-modeled meshes.

Numerical stability is maintained by enforcing a constraint CFL ≈ 0.5, supported by *adjustableRunTime*, which dynamically adapts the time step based on local velocity and cell size.

The following table (3.8) summarizes the total number of elements, number of processor cores used, and total CPU time for each mesh configuration.

Mesh	**N° elements**	**Cores**	**Total CPU time [s]**
Coarse	93034	3	$\approx 4.32 \times 10^5$
Medium	114945	3	$\approx 4.77 \times 10^5$
Medium Resolved	155560	5	$\approx 8.20 \times 10^5$
Fine	392136	13	$\approx 9.50 \times 10^5$

Table 3.8: Computational cost evaluation for each mesh

The mesh chosen for conducting numerical campaigns is the **medium wall-modeled** mesh, considering it as the one that guarantees high accuracy in representing the flow inside the ejector assisted by a substantial reduction in computational cost.

Among the meticulous review of the key parameters, it was shown that the curves associated with each respective mesh represent in a perfectly similar way the distribution of

Mach at the centerline. The confirmation of the goodness of the chosen mesh is supported by the convergence study carried out for the relative error of the mass flow rate and, therefore, of the entrainment ratio, always remaining below 0.5% for both cases examined. The wall-modeled approach is also rewarded by the evaluation of computational cost, which is one of the relevant parameters to keep an eye on. The substantial reduction in the total number of elements, and therefore a greater size of the cells, translates into a net halving of the total CPU time, thus allowing the parallelization of more case studies to be simulated thanks to the occupation of a smaller number of cores. Despite the use of wall functions that do not well approximate the trend of the velocity profile, against the excellent approximation for finer meshes, from the considerations made above, the choice still tends towards the medium wall-modeled mesh. It guarantees high accuracy in the evaluation of global parameters, such as Mach and ER, as well as the parameters of main interest for comparison with the experimental campaigns conducted.

4

Results

After justifying the choice of the optimal mesh, showing the main parameters considered in the selection process, the next step concerns the numerical evaluation of the flow behavior in the ejector, comparing the data with those obtained from similar experimental campaigns. The entire experimental campaign was conducted by Tani Angiero and Jan Van den Berghe, who initially compared the application of a primary nozzle with a simply convergent configuration to a convergent divergent type, as described in Angiero's thesis (9). The facility and the components used, with the appropriate calibration and evaluation of the uncertainties, are described in Angiero's thesis.

Considering the configuration of convergent divergent primary nozzle, a total of 20 experimental campaigns were carried out, varying the operating conditions appropriately, specially by adjusting the total pressure ratio at the inlet. Among these, four experimental campaigns were selected, characterized by a different ratio of total pressure at the inlet. From the highest to the lowest ratio, the selected campaigns are: campaign 8 ($\frac{p_{0,1}}{p_{0,2}} = 4.582$), campaign 3 ($\frac{p_{0,1}}{p_{0,2}} = 3.553$), campaign 7 ($\frac{p_{0,1}}{p_{0,2}} = 2.668$) and campaign 6 ($\frac{p_{0,1}}{p_{0,2}} = 1.928$) are listed. For each of these campaigns, RANS simulations were therefore conducted in openFOAM, under the same conditions as the respective experimental campaign, and boundary conditions as stated in the section [3.2.1.2].

This chapter aims to evaluate the results obtained from the numerical simulations, examining the functioning of the ejector under various operating conditions, and comparing the obtained data with the experimental database provided.

4.1 Numerical campaigns

This section serves as an introduction to the selection of inlet conditions related to the numerical campaigns conducted, for which the same approach has been used. Taking into account the experimental database provided [5], only on-design cases were taken into account for the selection of the inlet conditions. An average value of these cases was determined regarding the total pressure and total temperature at the inlet of the two nozzles. The conditions applied to the individual patches are detailed in the section [3.2.1.2].
Below are reported the details for the inlet conditions.

Campaign	$p_{0,1}$ **[Pa]**	$p_{0,2}$ **[Pa]**	$T_{0,1}$ **[K]**	$T_{0,2}$ **[K]**	$p_{0,1}/p_{0,2}$ **[-]**
8	471427	102877	287	287	**4.582**
3	352675	99243	288	288	**3.553**
7	244661	91961	288	287	**2.668**
6	183931	95376	288	288	**1.928**

4.2 Post-processing

This post-processing section is divided into two main parts: **flow topology** and **comparison with experimental data**. For the flow topology study, the variations of the flow characteristics inside the ejector under different operating conditions are examined. This discussion is also complemented by a brief preliminary analysis of mixing within the constant-area mixing duct.
The comparison with experimental data, mainly emphasizing the evaluation of the ejector performance, and how it varies with the operating conditions. In conclusion, pressure profiles along the wall of the constant-area mixing duct are reported, as support for the treatment of the flow behavior inside the ejector.

4.2.1 Flow topology

The analysis of flow topology in supersonic ejectors is essential for understanding the internal fluid dynamics of the system.
The dimensions of the ejector and the dimensionless length used for both x and y axes are reported in section [3.1.1]. It is briefly recalled that the origin of the axes coincides with the primary nozzle outlet, the constant area mixing duct begins at $x/L = 0.2$, while the diffuser inlet is located at $x/L = 0.57$. The numerical analysis was conducted through 2D axisymmetric RANS simulations in OpenFOAM, with boundary conditions matching those of the experimental tests [3.2.1.2]. To visualize the flow behavior, the Mach number fields were reported and analyzed, providing a clear evidence of the shock-expansion waves structures inside the ejector. For each campaign, the analysis focuses on the variation of the flow behavior with increasing back pressure, from on-design to off-design conditions, extending to malfunction scenario, i.e. reversed flow. In a second step, the four campaigns were compared, pointing out how the flow behavior varies with the variation of the total pressure ratio ($\frac{p_{0,1}}{p_{0,2}}$) at the inlet.
The two main theories describing the flow behavior inside the ejector and the limitations related to both, have been briefly introduced in the literature section [2] . The Fabri-choking theory predicts the formation of an aerodynamic throat, where the secondary flow reaches sonic conditions as a result of the expansion of the primary flow. This theory is mainly applicable for high total pressure ratios at inlet (typically $\frac{p_{0,1}}{p_{0,2}} > 5$), while it shows significant limitations for low pressure ratios, i.e. in cases where the primary flow is over-expanded (1). On the other hand, the compound-choking theory does not require both flows to reach sonic conditions for the system to be considered chocked ($M_{eq} > 1$

or $\beta < 0$). However, the assumption of constant static pressure, on which this theory is based, is strongly limiting due to the presence of shock-trains, making it more suitable for the analysis of under-expanded primary flows. The numerical cases analyzed show distinct flow configurations depending on the total pressure ratio at the inlet, for each campaign is shown the Mach number field of three on-design cases and two off-design cases. Campaign 8, characterized by a total pressure ratio $\frac{p_{0,1}}{p_{0,2}} = 4.582$, shows analogies with the hypotheses of the Fabri-choking theory. From figure (4.1)), relative to the on-design case (a), the Mach fields highlight the formation of the "Y-wave pattern". In this configuration the primary flow, after acceleration through the primary nozzle, expands according to a Prandtl-Mayer expansion wave. This expansion is reflected by the axis to an oblique shock, which, once in contact with the shear layer, generates a normal shock in the secondary flow. The subsequent interaction of the normal shock with the wall and its reflection with the shear layer results in the formation of a second oblique shock, defining the "Y-wave pattern" [2.1.2.4]. The primary flow is always choked and reaches the sonic condition near the throat of the primary nozzle, accelerating further in the diverging part. The supersonic region extends along the entire mixing duct, up to an initial part of the diffuser where a strong oblique shock occurs, generating a secondary shock-train that compresses the flow downstream.

The increase in back pressure causes a progressive reduction in the length of the supersonic region, with the formation point of the oblique shock shifting upstream. For low p_{out} in on-design cases the oblique shock formation initially takes place in the middle of the diffusion (case (a), figure (4.1)), but as the back pressure increase, it moves upstream, up to the constant area mixing duct (case (c), figure (4.1)). For off-design cases, the secondary flow is no longer choked, and the shock-train originating from the primary nozzle outlet, gradually dissipates along the ejector due to viscous phenomena, becoming weaker as the back pressure increases. Another evidence of the figures is undoubtedly that for on-design cases, the flow seems to maintain constant characteristics from the primary nozzle inlet up to a certain position in the mixing duct. This confirms the typical behavior of a chocked system, in which downstream back pressure variation cannot propagate upstream due to the presence of sonic conditions.

In Appendix A (figure (5.1)), the static pressure fields are also provided to support the description of the flow topology. The static pressure fields (p) allows for the easy identifications of interactions between shock-waves and expansion-waves that occur along the duct. Shock-waves appears as sharp static pressure discontinuities, due to the rapid compression and deceleration of the flow. The intensity of the color gradient is an indication of the

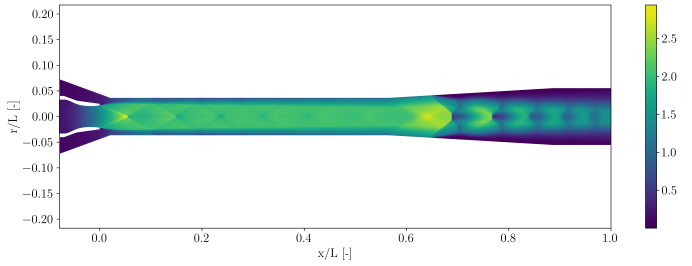

(a)

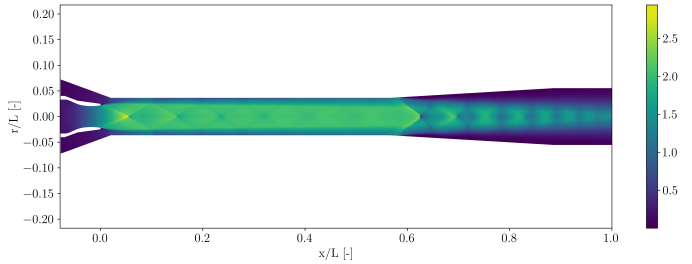

(b)

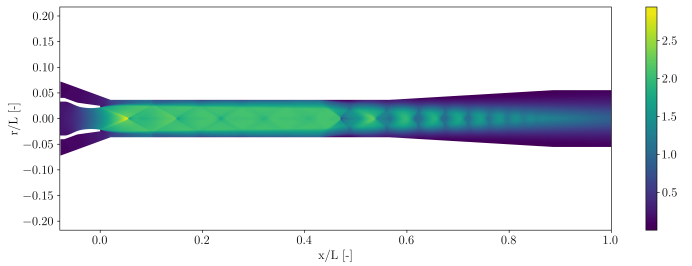

(c)

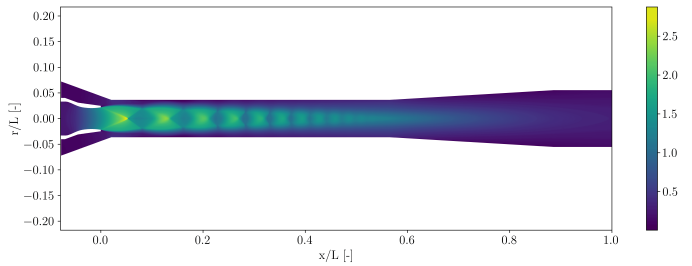

(d)

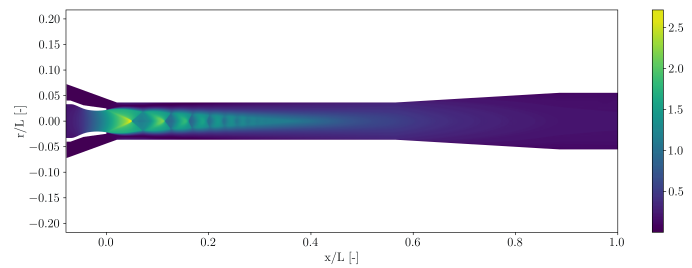

(e)

Figure 4.1: Mach number fields, Campaign 8. (a) $p_{out} = 105000$ Pa, (b) $p_{out} = 130000$ Pa, (c) $p_{out} = 165000$ Pa, (d) $p_{out} = 210000$ Pa, (e) $p_{out} = 230000$ Pa

shock strength. The expansion-waves, on the other hand, show a continuous acceleration of the flow, underlined by a gradual decrease in pressure. Especially in the on-design case of $p_{out} = 105000$ Pa, the gradual decrease in pressure identifies the expansion that occurs at the exit of the primary nozzle. The expansion is reflected by the axis in an oblique shock, which subsequently forms the "Y wave pattern". The localization of the shocks is allowed by the visualization of the abrupt color gradient. Regarding the shock in the diffuser, its strength is notably evident, as indicated by regions with very high static pressure gradients.

The turbulent kinetic energy field (k) is also reported in the Appendix A (figure (5.5)). For on-design cases, particularly at low back pressure, the primary flow shows no signs of turbulence for most of the mixing duct, identifying how turbulent structures develop essentially in the shear layer. Meanwhile, high values of k are identified near the secondary shock-train that takes place in the diffuser, indicating as the flow becomes entirely turbulent. As the back pressure increases, turbulence intensity within the shear layer also increases, and a weak turbulence begins to develop in the boundary layer. Due to the combined influence of boundary and shear layers, for on-design cases with high back pressures, the transition of the secondary flow from laminar to turbulent is highlighted, about halfway through the mixing duct.

Campaign 3 ($\frac{p_{0,1}}{p_{0,2}} = 3.55$) exhibits flow characteristic similar to those of Campaign 8, characterized by a slightly under-expanded primary flow and a lower total pressure ratio at the inlet. The "Y-wave pattern", which was faintly observed in Campaign number 8, completely disappears from the Mach number fields for Campaign 3, highlighting the limitation of Fabri-choking theory and showing instead analogies with the compound-choking theory concept. The primary flow is less under-expanded than the Campaign 8, so the expansion at the primary nozzle outlet is minor, leading to a slower flow inside the ejector, therefore slightly lower Mach values. As the Mach number decreases, the Mach angle (μ=$\sin^{-1}(\frac{1}{\mathrm{M}})$) increases, reducing the stretching of the 2D structures inside the ejector (4.2)).

The numerical Campaigns 7 and 6, characterized by low total pressure ratios at the inlet, exhibit over-expanded primary flow, where the primary nozzle exit flow is marked by the formation of Mach diamond structure. The Mach number fields in figure (4.3) (case (a)), for an on-design condition, show two oblique shocks at the primary nozzle exit, which merge into a normal shock, forming a Mach diamond. The oblique shock interacting with the shear layer undergoes expansion reflection, generating a sequence of shock-expansion waves along the along the mixing duct. The supersonic structure of this case contracts and experiences a gradual velocity reduction as the p_{out} increases. From the static pressure

fields (figures (5.3)), for this on-design case, the formation of the Mach diamond is more distinctly observed. It can be seen how the two oblique shocks converge in a normal shock, generating the Mach diamond. Moreover, as previously noted from the relative Mach field, it is evident how the oblique shock, after interacting with the shear layer, reflects as an expansion wave, highlighted by the gradual variation in the color gradient. For all cases, on-design and off-design, it is clearly shown that the pressure recovery, approaching the value of p_{out}, predominantly occurs within the diffuser.
The turbulence kinetic energy field analysis (figure (5.7)) shows how, in the first on-design cases, the turbulent structure is more developed than in previous campaigns, increasing further with rising back pressure.
In Campaign 6, over-expansion effects become even more evident, as the static pressure of the primary flow at the nozzle exit is significantly lower than that of the mixing chamber, with the generation of a curved-normal shock at the outlet of the primary nozzle. This phenomenon causes a significant reduction in velocity, while still maintaining supersonic condition along the mixing duct, but at lower Mach numbers. The associated kinetic energy dissipation negatively impacts ejector performance, reducing its overall efficiency.
Therefore, numerical analysis highlights the need to identify an "optimal" total pressure ratio at the inlet to ensure a balance between efficiency and flow stability. In cases of over-expanded primary flow, the mixing between primary and secondary flow is generally more effective, due to the lower velocity of the primary stream. Lower Mach number values allow for a greater shear layer growth, improving momentum exchange and turbulent mixing between the two flows (54). However, conditions of excessive over-expansion, characterized by the formation of curved-right shocks, can lead to a significant reduction in the efficiency of the ejector due to energy dissipation.
Conversely, in cases of under-expanded primary flow, the continuous expansion of the primary flow at the primary nozzle exit results in a narrower secondary cross-section, reducing the secondary mass flow rate and increasing in the velocity gradient between the two streams. The analysis suggests that the optimal total pressure ratio at the inlet should be positioned between these two extremes.
However, the identification of the optimal operating condition is highly dependent on the specific application of the ejector. If the goal is to maximize the entrainment ratio within a narrow operating range, it is preferable to operate at low total pressure ratios at inlet. If, on the other hand, a more stable configuration with reliable performance over a wide back pressure range is required, it is more advantageous to use higher total pressure ratios, which ensure greater system robustness.

This analysis requires further evaluations regarding the ejector performance the mixing between the two flows, to provide more data for identifying the optimal operating condition. The goal is to define the best trade-off between performance optimization ($\omega = \frac{\dot{m}_2}{\dot{m}_1}$) and the ability to maintain high performance over a wide range of back pressures.

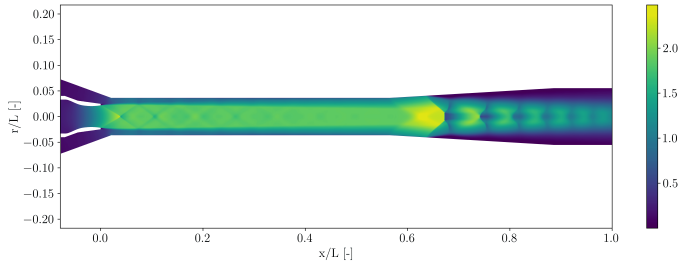

(a)

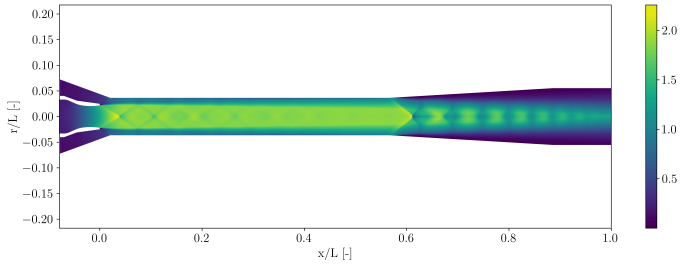

(b)

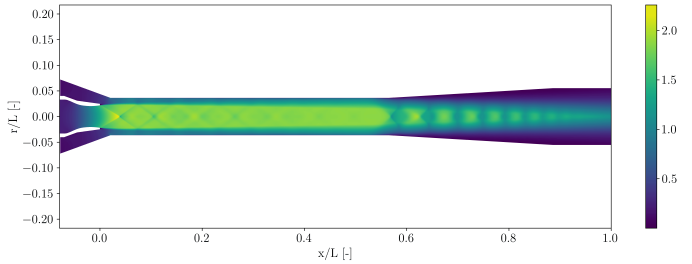

(c)

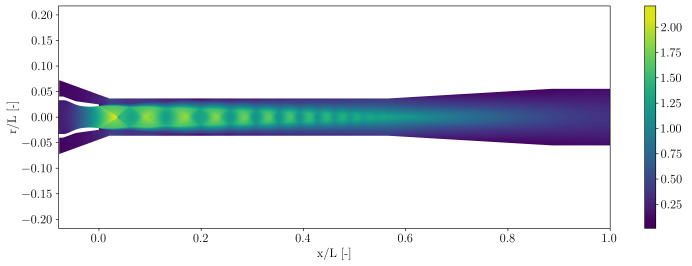

(d)

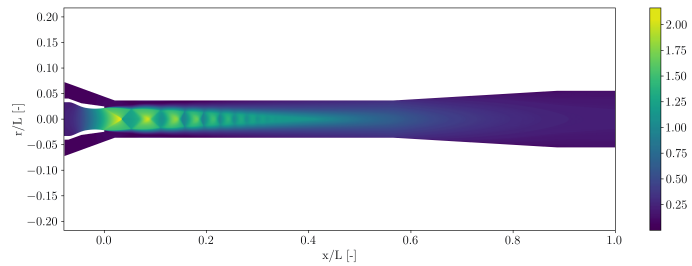

(e)

Figure 4.2: Mach number fields, Campaign 3. (a) p_{out} = 96061 Pa, (b) p_{out} = 114344 Pa, (c) p_{out} = 124199 Pa, (d) p_{out} = 166862 Pa, (e) p_{out} = 182526 Pa

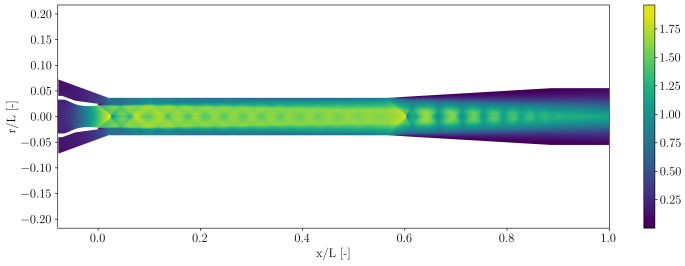

(a)

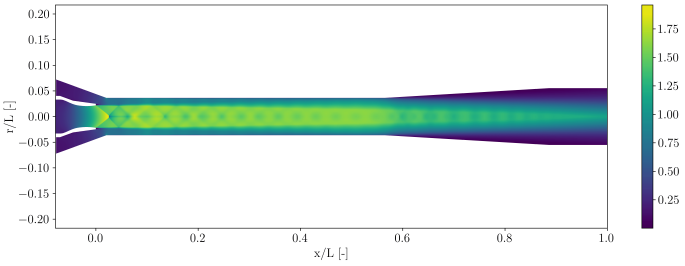

(b)

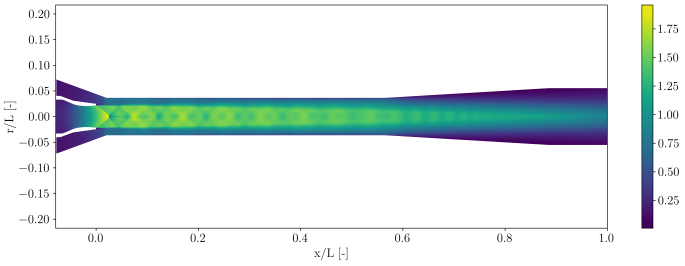

(c)

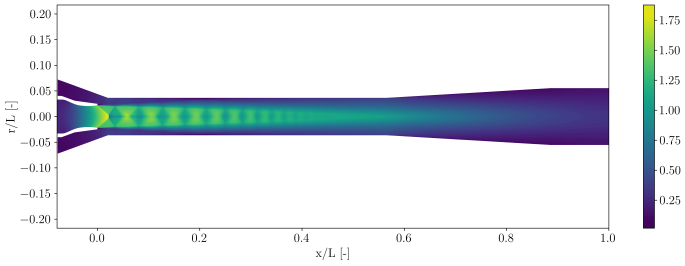

(d)

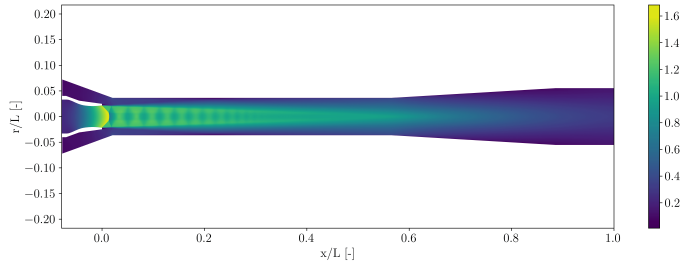

(e)

Figure 4.3: Mach number fields, Campaign 7. (a) $p_{out} = 94506$ Pa, (b) $p_{out} = 97895$ Pa, (c) $p_{out} = 108774$ Pa, (d) $p_{out} = 132498$ Pa, (e) $p_{out} = 144868$ Pa

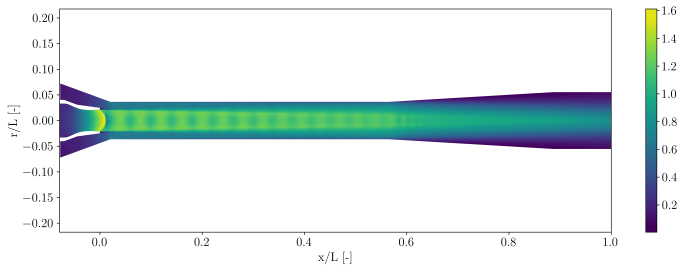

(a)

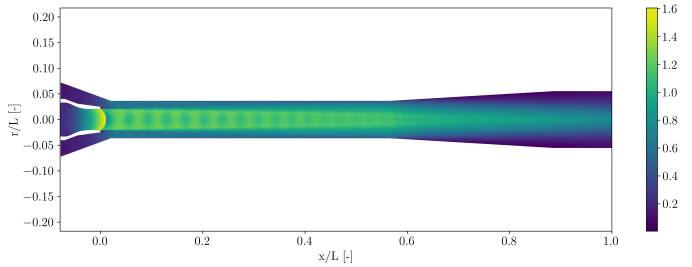

(b)

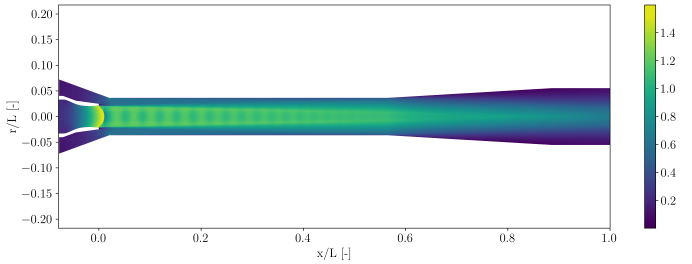

(c)

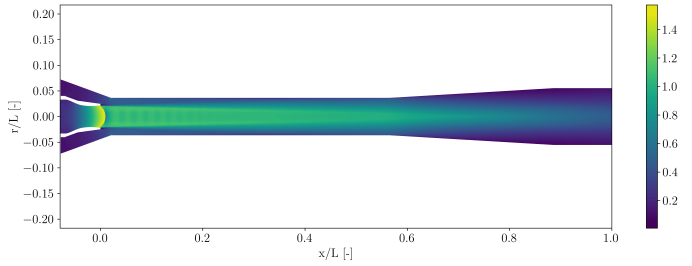

(d)

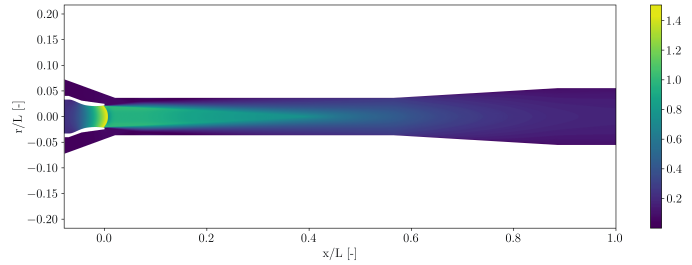

(e)

Figure 4.4: Mach number fields, Campaign 6. (a) $p_{out} = 98472$ Pa, (b) $p_{out} = 101260$ Pa, (c) $p_{out} = 104083$ Pa, (d) $p_{out} = 111392$ Pa, (e) $p_{out} = 126207$ Pa

4.2.2 Preliminary mixing analysis

The evaluation of mixing is one of the main interests related to the study of supersonic ejectors. A key aspect of this analysis is estimating the location where the two flows begin to mix, in order to evaluate the total length required for complete mixing. With understanding of these parameters, the geometry of the constant area mixing duct can be optimized, avoiding excessive length that would also lead to additional losses along the duct.

A preliminary evaluation of the ejector mixing analysis is carried out by considering the velocity profiles and their evolution along the mixing duct. Figure (4.5) shows split view of the ejector geometry, in the upper part the Mach fields of the case (figure (4.1) case (a)) and in the lower half the distribution of the velocity profiles along the ejector domain. The average velocity near the duct axis is approximately 500 m/s, serving as a reference for the velocity values depicted in the profiles.

The representation of the Mach fields and velocity profiles highlights that, in the initial part of the mixing duct, the primary and secondary flows exhibit very marked velocity differences, with a high gradient indicating their initial separation. Continuing along the duct, the velocity difference between the two streams progressively smooth out, leading to the formation of more regular profiles, up to a point where the mixing can be assumed completed. A first empirical estimate, based on the observation of the velocity profiles, indicates that the point of regularization of the profiles is around $x/L = 0.13$.

To provide a more detailed assessment of the interaction between the two flows, the growth of the shear layer and the boundary layer along the mixing duct was analyzed. Determining the exact point at which these layers interact provides more details of the mixing process and a more precise estimation of the length needed to complete the mix.

Given the absence of a clear free stream, due to the growing shear layer, the definition of boundary layer thickness, based on $U(y)=0.99U_\infty$, cannot applied in this context.

To characterize the extent of the boundary layer and the shear layer, a qualitative method was adopted, based on the evaluation of the total pressure gradient along the normal direction ($\frac{\partial p_t}{\partial y}$). The shear layer, which essentially represents the interface between the two flows and their mixing, is characterized by high levels of turbulent kinetic energy (k) and significant variations in total pressure.

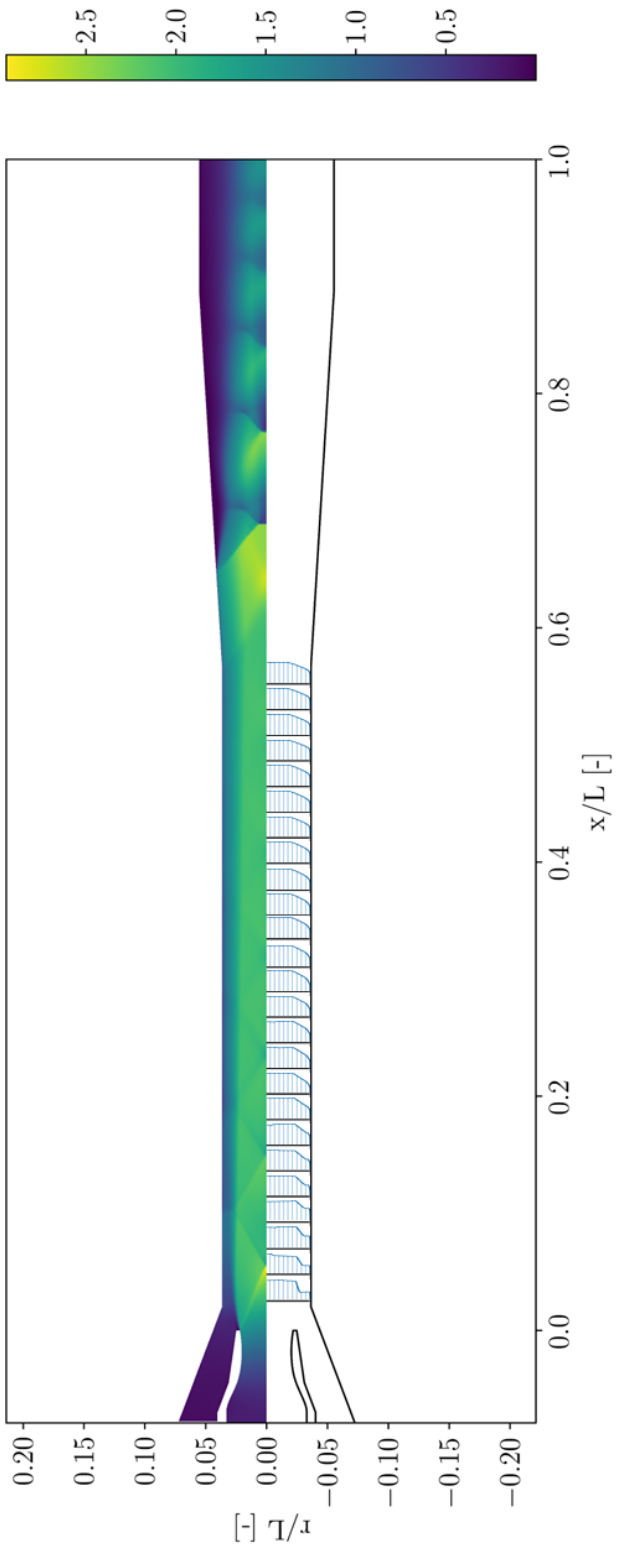

Figure 4.5: Velocity profiles, Campaign 8 $p_{out} = 105000$ Pa

The boundary layer is also mainly influenced by viscous effects. In both cases, the total pressure gradients are particularly high.

The total pressure progressively decreases from the axis to the wall, assuming a negative gradient in the shear layer and boundary layer regions. In order to determine the lower and upper limits of the shear layer and the limit of the boundary layer, a threshold criterion of $(\frac{\partial p_t}{\partial y})_{rel} = -0.002$ was adopted. A relative total pressure gradient $(\frac{\partial p_t}{\partial y})_{rel}$ is considered, as it is dimensionless using the minimum (negative) total pressure gradient measured in the area of the primary flow, from the axis to the dividing streamline. The minimum total pressure gradient is located near the dividing streamline. The dividing streamline ideally represents the separation line between the primary and secondary flow in inviscid conditions. According to studies by Baguet et al. (1), the shear layer is symmetrically distributed with respect to this line.

Based on the Baguet e al. (1) consideration, the lower limit of the shear layer was identified at the first point below the dividing streamline where the $(\frac{\partial p_t}{\partial y})_{rel}$ exceeds the -0.002 threshold. Similarly, the upper limit of the shear layer was determined as the first point above the dividing streamline where the $(\frac{\partial p_t}{\partial y})_{rel}$ exceeds the same threshold. For the definition of the boundary layer thickness was considered the first point, moving from the wall towards the center of the duct, where the relative total pressure gradient exceeds the established threshold .

The limitations of this methodology are acknowledged, which provides an approximate and qualitative estimation, acceptable for the evaluation of the preliminary mixing reported in this study. More research is needed for a more vigorous evaluation.

The main goal of this treatment is to analyze how the contact point between shear layer-boundary layer varies with the variation of the operating conditions, thus varying the total pressure ratio at the inlet. Figure (4.6) shows zoomed-in sections of the Mach number fields in the area of interest to highlight the contact point between the two layers. For ease of visualization, the cases related to Campaign 8 and 7 are shown.

The dotted-red lines indicate an approximation of the free stream lines for the primary and secondary streams, the white line represents the dividing streamline, the blue line marks the boundary layer limit, and the two orange lines depict the shear layer limits. The figures show the on-design cases of the respective campaigns. From the visualization of the Mach fields, it is clearly observed that, as the total pressure ratio at the inlet decreases, the interaction point between boundary layer and shear layer progressively shifts downstream.

(a)

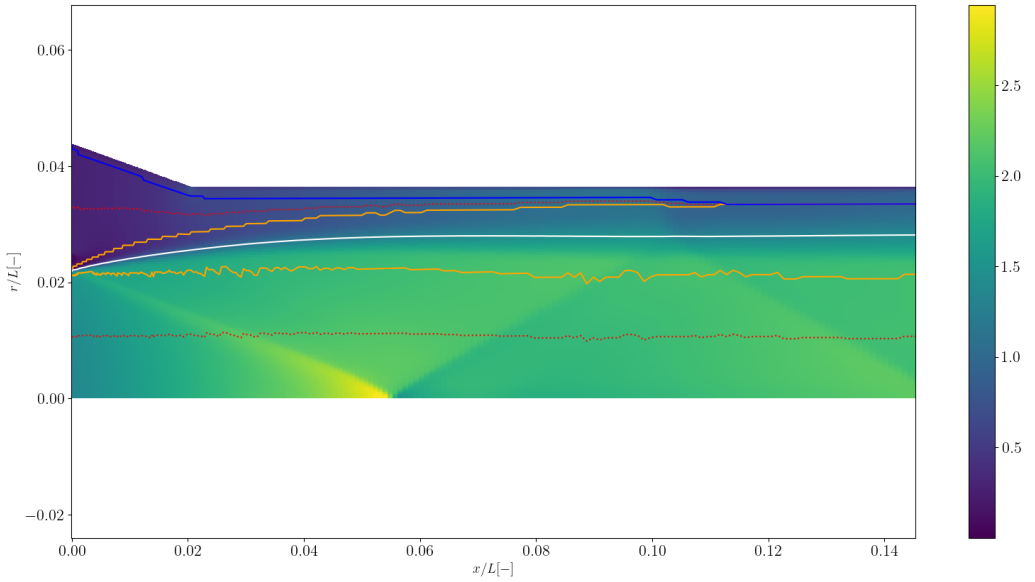

(b)

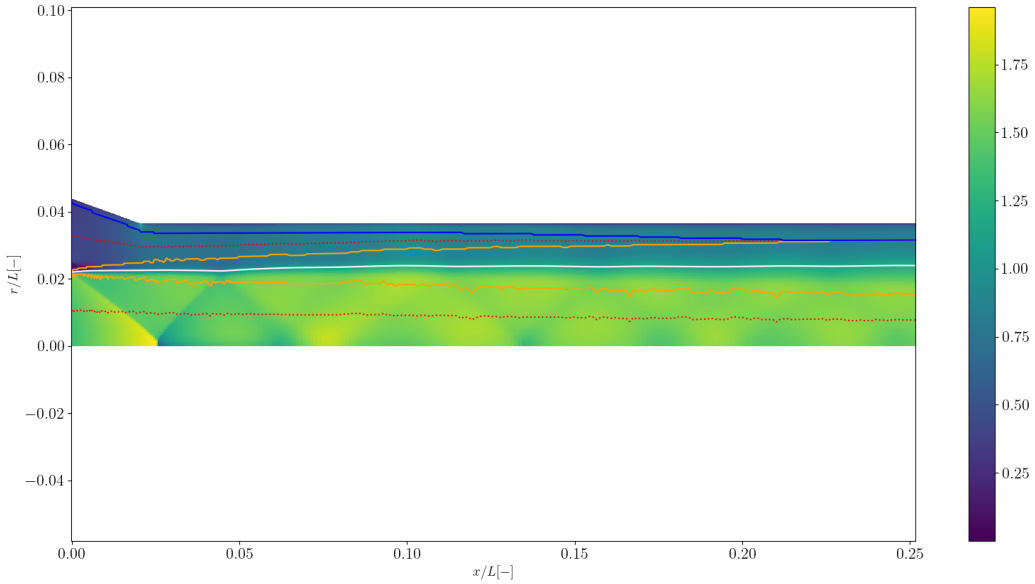

Figure 4.6: Shear layer-boundary layer interaction plotted on on-design Mach number fields: (a) Campaign 8 ($p_{0,1}/p_{0,2} = 4.582$), (b) Campaign 7 ($p_{0,1}/p_{0,2} = 2.668$)

Figure (4.7)) shows the growth of the shear layer and boundary layer radii, showing in more detail the point of contact between the two layers. In this representations, the details of all the Campaigns considered are shown.

A more detailed analysis of the evolution of the radii shows that, in cases characterized by under-expanded primary flow and higher velocity (Campaign 8), the boundary layer remains thinner, as expected for high velocities in the duct, and the interaction point occurs at $x/L = 0.111$.

However, as the flow progresses along the duct, the boundary layer thickness increases, in particular due to the formation of the "Y-wave pattern", near $x/L = 0.1$ as shown in case (a) of figure (4.1). In under-expanded primary flow conditions, the shear layer tends to be pushed towards the secondary flow, limiting the growth of its lower portion (shear layer_{down}), while the upper portion (shear layer_{up}) has more pronounced growth.

In cases with lower velocities inside the ejector (e.g., in Campaigns 3, 7 and 6), the contact point between the two layers occurs progressively further downstream, respectively at $x/L = 0.165$, $x/L = 0.224$ and $x/L = 0.221$. The shear layer behavior follows a consistent pattern: in cases with low total pressure ratios at inlet, the shear layer_{up} grows less rapidly, while the boundary layer tends to increase in thickness, as expected for flows at lower speed. In over-expanded cases, the the shear layer growth is more uniform and the interaction point is shifted further downstream.

These observations are crucial for the design of the mixing duct. In cases of over-expanded primary flow, gradual and slow mixing is evident in the first parts of the duct, implying that the mixing process require a longer distance to be completed. Consequently, a sufficient long mixing duct will be required to ensure the complete mixing.

The considerations derived from this analysis, combined with the characterization of the flow topology and the performance of the ejector [4.2.2.1], are key elements in guiding the choice of an "optimal" operating condition. The choice must therefore balance mixing efficiency, duct length, in order to obtain an ejector with reliable and efficient performance.

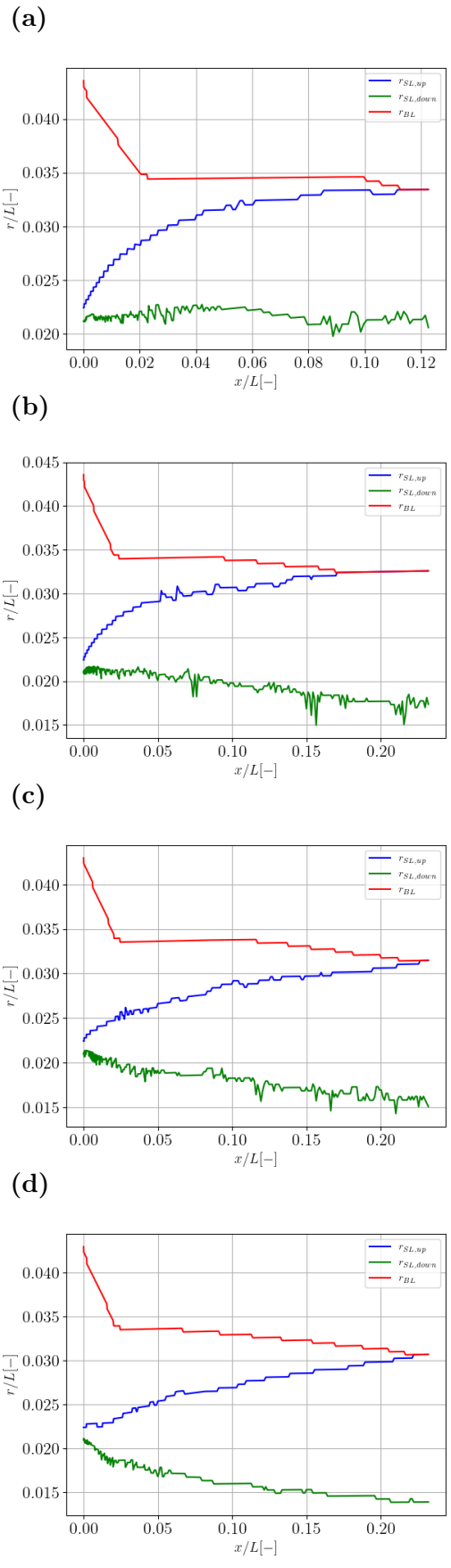

Figure 4.7: Shear layer-boundary layer interaction point: (a) Campaign 8 ($p_{0,1}/p_{0,2} = 4.582$), (b) Campaign 3 ($p_{0,1}/p_{0,2} = 3.553$), (c) Campaign 7 ($p_{0,1}/p_{0,2} = 2.668$), (d) Campaign 6 ($p_{0,1}/p_{0,2} = 1.928$)

4.2.2.1 Mass flow rates and characteristic curves

Relying on the numerical setup reported in section [3], various simulations were conducted, at the same conditions of the experimental campaign. In particular, the numerical treatment specially focused on the transition from on-design to off-design, and the malfunctioning zone, characteristic of the latest off-design cases (figure (2.3)).
Especially for Campaigns 8 and 3, the ejector performance was analyzed at additional back pressure values, located in the on-design to off-design transition area, defining the critical back pressure p^*_{out}. The performance assessment, dictated by the determination of the entrainment ratio, is linked to the determination of the respective mass flow rates for primary and secondary nozzles (ER= $\frac{\dot{m}_s}{\dot{m}_p}$). The mass flow rates are represented in dimensionless form as in (9), normalized with respect to the maximum expected flow rate in an isentropic expansion. This approach allows the generalization of the performance analysis, making immediate the identification of the choking condition, i.e. dimensionless mass flow rate close to 1.

$$\hat{\dot{m}}_1 = \frac{\dot{m}_1}{p_{0,1} A_{th} \sqrt{\frac{\gamma}{RT_{0,1}}} \left(\frac{\gamma+1}{2}\right)^{-\frac{1}{2}\frac{\gamma+1}{\gamma-1}}} \tag{4.1}$$

$$\tag{4.2}$$

$$\hat{\dot{m}}_2 = \frac{\dot{m}_2}{p_{0,2} (A_y - A_{th}) \sqrt{\frac{\gamma}{RT_{0,2}}} \left(\frac{\gamma+1}{2}\right)^{-\frac{1}{2}\frac{\gamma+1}{\gamma-1}}} \tag{4.3}$$

The cross-sections reported in the formulas [4.1] represent: A_{th} is the primary nozzle throat section while A_y represents the section of the constant area mixing duct.
Figure (4.8) shows the characteristic curves and the relative dimensionless mass flow rates for the numerical Campaign 8 and 3. The uncertainties depend essentially on the sensors, prescribed by the manufacturers. Details on uncertainties and sensors used are reported in a appropriate section in Angiero's thesis (9). The characteristic curves, obtained using the inlet condition specified in section [4.1], for the two campaigns with low total pressure ratio showed discrepancies when compared to the respective experimental measurements. With the aim of analyzing what could be the possible cause of the vertical shift in the ER values, additional numerical simulations were carried out, focusing mainly on off-design cases, for the campaigns that showed the highest discrepancy, i.e. Campaign 6 and 7. At first was chosen an off-design case of the Campaign 7, with back pressure value $p_{out} = 144868$ Pa.

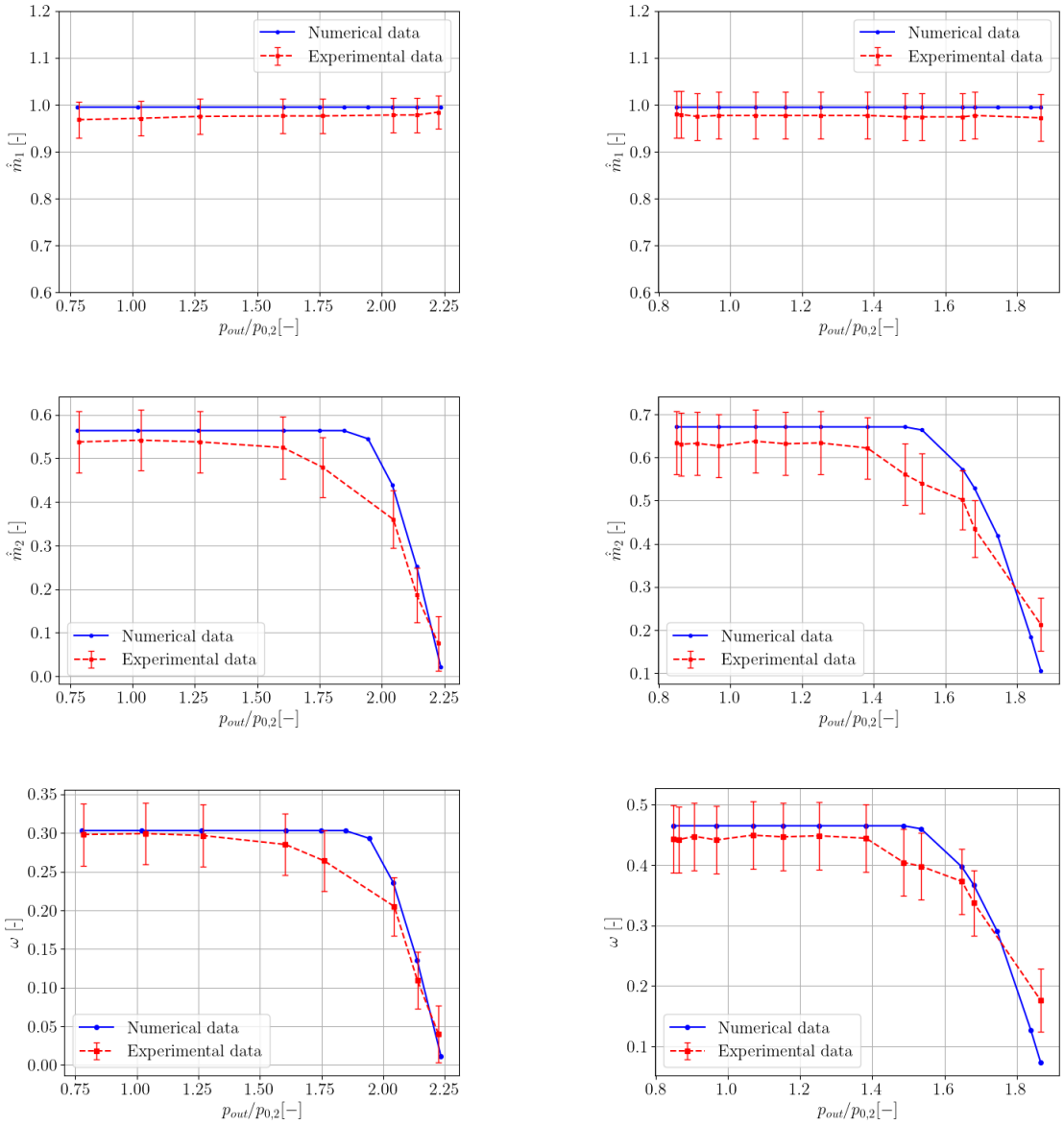

Figure 4.8: Performance analysis: dimensionless primary mass flow rate, dimensionless secondary mass flow rate and entrainment ratio for Campaign 8 (left) and Campaign 3 (right)

Initially, two possible causes for the discrepancy were identified: **the turbulence intensity (TI)** as inlet condition of the two nozzles, and, secondly, the significant and increasingly marked **difference in the total pressure conditions of the secondary nozzle**, between numerical simulation and experimental campaigns (Appendix B [5]).
As specified in the boundary section [3.2.1.2], the TI chosen for the numerical analysis was 5%. Maintaining the same conditions, new numerical simulation were conducted, appro-

priately changing the TI values at the inlet to 1% and 10%.
Observing the two tables reporting the inlet condition [5], is evident the difference in the secondary total pressure between numerical and experimental data. This variation is not accompanied by the variation of the primary total pressure, leading to an inconsistency analysis since it alters the total pressure ratio at inlet, preventing a fixed operating conditions assessment. The inlet conditions used at first for the numerical campaigns were chosen to obtain an operating curve while keeping the inlet condition fixed (which is difficult to achieve in the experiments). These curves serve as reference curves for the development of the 1D model.
New numerical simulations were therefore launched using the exact conditions of total secondary and primary pressure as in the experimental case.
The table (4.1) reports the primary and secondary mass flow rate variations, following the appropriate adjustments declared before, comparing them with the relative experimental values with related uncertainties.
The **TI** variation as inlet condition of the two nozzles does not generate substantial changes in the estimation of the secondary mass flow rate, on the contrary a slight underestimation is noted when moving to higher TI values. Using the exact conditions from the experimental test, significantly improved the secondary mass flow rate estimation, completely reducing the discrepancy underlined in the previous curves.
Following this finding, additional numerical simulations for Campaign 6 and Campaign 7 were carried out at the exact experimental conditions, giving priority to cases in which the $p_{0,2,}$ difference between the numerical case and the experimental test.
The figures (4.9) illustrate the corrected mass flow rate and the estimated entrainment ratio, revising the previous results, obtained taking into account the conditions specified in section [4.1].

Cases	$p_{0,1}$ **[Pa]**	$p_{0,2}$ **[Pa]**	p_{out} **[Pa]**	$\dot{m}_1$ **[kg/s]**	$\dot{m}_2$ **[kg/s]**
Experiment	246078	109460	144868	0.352 ± 0.079	0.139 ±0.079
TI 5%	244661	91961	144868	0.356	0.029
TI 1%	244661	91961	144868	0.356	0.029
TI 10%	244661	91961	144868	0.356	0.028
Experiment like	246078	109460	144868	0.358	0.189

Table 4.1: Critical back pressure estimation from numerical and experimental data

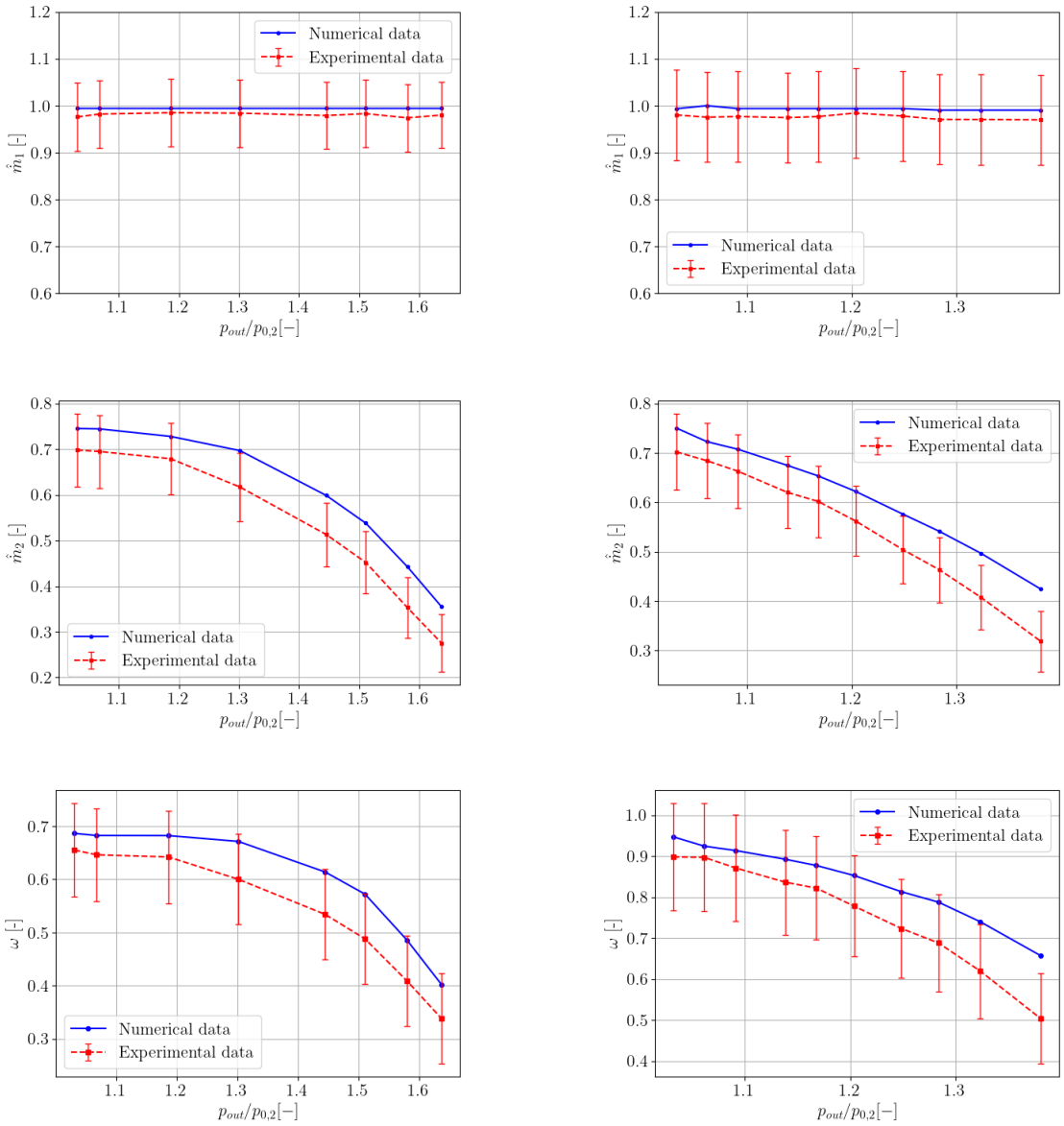

Figure 4.9: Updated performance analysis: dimensionless primary mass flow rate, dimensionless secondary mass flow rate and entrainment ratio for Campaign 7 (left) and Campaign 6 (right)

The analysis of the characteristic curves of each campaign reveals that the transition from on-design to off-design conditions is predicted at higher back pressure values for campaigns with high total pressure ratio at the inlet.

The table (4.2) highlights how the estimation of the transition between on-design and off-design conditions varies, as the total pressure ratio at inlet changes. The $p_{out}/p_{0,2}$ value is obtained by referring to the respective $p_{0,2}$ value of each campaign [4.1].
Notably, the estimation of the critical back pressure is overestimated as the total pressure ratio at inlet increases. For campaigns with higher total pressure ratios (Campaign 8 and 3),

$p_{0,1}/p_{0,2}$	$p^*_{out}/p_{0,2}$ (EXP)	$p^*_{out}/p_{0,2}$ (RANS)
1.928	1.07	1.08
2.668	1.18	1.18
3.553	1.48	1.53
4.582	1.61	1.84

Table 4.2: Estimation of the critical back pressure, comparison between experimental and numerical data

the transition between on-design and off-design occurs later than observed in experimental tests carried out. For Campaign 3 the critical back pressure value is $p^*_{out}/p_{0,2} = 1.53$, while the experimental test reports the transition to an earlier value, $p^*_{out}/p_{0,2} = 1.48$. With regard to Campaign 8, the experimental campaign defines the transition at $p^*_{out}/p_{0,2} = 1.61$, while the numerical results detect this transition for slightly higher value, $p^*_{out}/p_{0,2} = 1.84$. Mazzelli et al. (3) attribute the transition delay to the limitations of 2D RANS simulations, which fail to accurately capture wall roughness, better measured by 3D simulations. In the case in question these effects are however less evident due to the 2D axisymmetric configuration as in (1), (55). Due to wall effects caused by the wall roughness, a part of the moment of the two flows is lost due to friction with the walls, thus causing an underestimation of both entrainment ratio (ER) and critical back pressure. The effect of wall roughness becomes more evident at higher speeds, resulted in increasing losses, which could explain the differences on the estimation of the critical back pressure for cases with higher velocities inside the ejector for Campaigns 8 and 3.

4.2.2.2 Impact of the operating conditions on the performance

In order to study the direct influence of the operating conditions ($\frac{p_{0,1}}{p_{0,2}}$), the characteristic curves of all campaigns are plotted in the same graph (figure (4.10)). The back pressure is dimensionless with the total secondary pressure of Campaign 8. From the figure (4.10) it is evident as the off-design conditions exhibit an almost perfectly linear trend, with an

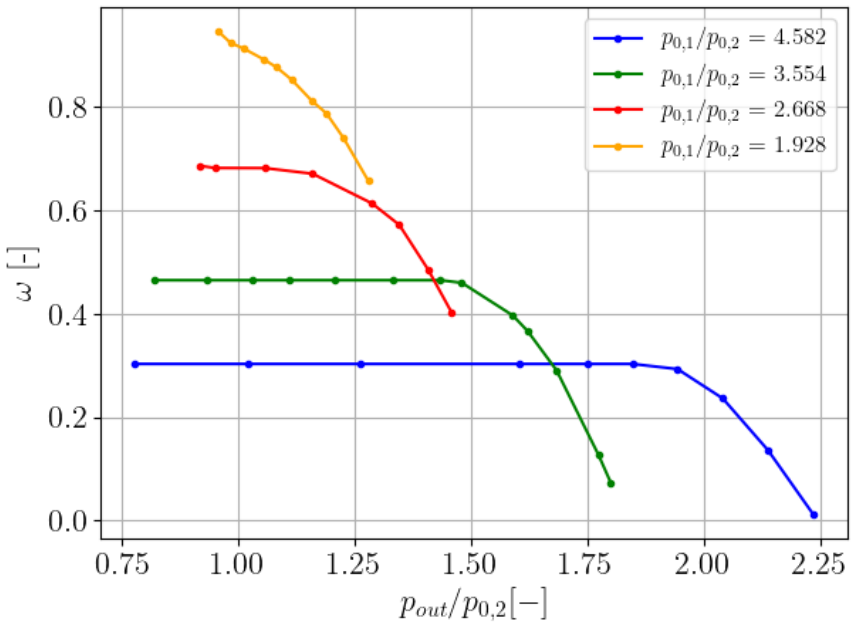

Figure 4.10: Updated ejector performance at $\frac{p_{0,1}}{p_{0,2}}$ variation

increasing slope as the total pressure ratio at inlet increases. An increase in the total pressure ratio at the inlet generates a shift of the curve downwards and to the right, decreasing the value of the entrainment ratio (ω), while significantly extending the operational range of back pressure.

The high total pressure ratios at the inlet allow for the maintenance of the choking condition over a wide back pressure range. This should allow a robust preservation of the choking condition even at high back pressure values.

With the support of the figure (4.10) it is possible to add considerations, complementing the flow topology analysis [4.2.1]. Ideally, the main interest would be to have a maximization of the entrainment ratio while maintaining the choking condition the widest back pressure range. In this regard, the Campaigns exhibited different characteristics. The Campaigns 6, distinguished by a highly over-expanded primary flow at the primary nozzle outlet, allows the achievement of the highest ER when compared with other campaigns. At the same time, the choking condition is essentially reached for the first or the firsts two back pressure values, reaching malfunction condition low back pressure. Conversely, Campaign 8 is characterized by under-expanded primary flow at the primary nozzle outlet. The plateau that defines the choking conditions of the system extends over the widest range of back pressure, characterized however by a maximum ER of about 0.3, the lowest

among the numerical campaigns.

Campaigns 7 and 3 seem to provide a good compromise regarding what are the main interests. The Campaign 7 allows the achievement of a maximum ER of about 0.7, maintaining the choking condition up to the value of back pressure between $p_{out} = 97895$ Pa and $p_{out} = 108774$ Pa. The Campaign 3 achieves a maximum ER around 0.46 for a range of back pressure that extends up to the value of $p_{out} = 147453$ Pa.

However, a definitive evaluation requires the earlier analysis on flow topology and mixing. The formation of shocks at the outlet of the primary nozzle, typical of cases with over-expanded primary flow (Campaign 6 and 7), is certainly more dissipative than the formation of expansions typical of cases of under-expanded primary flow (Campaign 8 and 3) [4.2.1]. Additionally, shear layer-boundary layer interaction occurs later for over-expanded primary flow cases, compared to under-expanded primary flow cases [4.2.2], so a longer duct for the mix completion is required.

The high speed gradients between the two flows, Campaign 8 and 3, allow an acceleration in the mixing, due to earlier shear layer-boundary layer interaction, reducing the required duct length.

However, identify an optimal operating condition is relative, as it depends on the intended ejector application. If the priority is maximizing performance for relatively low back pressure ranges, the optimal choice would be to operate at low total pressure ratio at the inlet, considering the requirement for a longer mixing duct. If stable performance with a shorter mixing duct is preferred, selecting medium-high total pressure ratio would be the better option.

4.2.2.3 Wall pressure profiles

An analysis of the wall pressure profiles along the constant area mixing duct provides important information about the local evaluation of the ejector operations. By examining the curves of the wall pressure profiles, it is possible to directly assess the flow behavior within the ejector, representing a boundary analysis of flow topology. The pressure profile allows to deduce the choking section position and represents the only local comparison with experimental data.

The following discussion presents the pressure profiles relating to each campaign, focusing on two on-design cases, the on-design to off-design transition case, and two off-design cases. The legend in the figures (4.11) and (4.12) includes the $\frac{p_{out}}{p_{0,2}}$ corresponding to the five selected cases. The black dashed line defines the sonic pressure, which for an isentropic compressible flow, is defined as follows.

$$\frac{p^*}{p_{0,2}} = \left(\frac{2}{\gamma+1}\right)^{\frac{\gamma}{\gamma-1}} \tag{4.4}$$

Where p^* denotes the aforementioned sonic pressure.

The limit defined by the sonic pressure indicates that, for curves falling below this threshold, the secondary flow has reached the sonic condition. It should be noted that the non-dimensionalisation was achieved using $L = 0.686$ m as reference length, highlighting the region from the primary nozzle outlet to the outlet of the ejector. The origin of the axes $x/L = 0$ coincides with the primary nozzle outlet, while the beginning of the diffuser returns to $x/L = 0.567$.

The wall pressure profiles for Campaign 8 clearly illustrate details previously in the flow topology section [4.2.1]. The curve's inflection, visible for the first on-design cases, indicates the presence of what had been defined as the "Y-wave pattern", typical of Fabri-choking theory. The formation of the normal shock, localized in the secondary flow, defines the "bump" visible in the trend of the pressure profiles. A second inflection, observed for x/L greater than 0.567, corresponds to the formation of the unsteady shock localized within the diffuser for the first on-design case, shifting leftward in the subsequent case (as discussed in section [4.2.1]. The visible oscillations define the succession of shocks-expansions, i.e. the shock train that occurs from the exit of the primary nozzle.

The definition of choking section, i.e. when both flows can be considered chocked, can be deduced near the point after which the transition curve begins to diverge. It is evident that the green curve, representing the transition case, deviates in behavior around $x/L = 0.1$,

where for the previous case, the "Y-wave pattern" takes place. The two on-design curves overlap along the entire mixing duct, while the transition curve shows a distinct growth. However, for the definition of these graphs takes into account the consideration in section [4.2.2.1], regarding the delay in estimating the critical back pressure (p^*_{out}) for which transition from on-design to off-design occurs. The experimental curve indicates the case of $p_{out} = 164962$ Pa, while the numerical one suggests $p_{out} = 190000$ Pa. If the numerical curve of $p_{out} = 165000$ Pa had been included, the pressure profile would align with the two on-design cases shown in figure (4.11), as demonstrated by figure (4.8), confirming that this case still highlights an on-design condition. The two off-design curves display a more regular trend, reflecting the absence of shock train in the secondary stream, with a net growth, due to the momentum exchange between the compound-subsonic streams (31). Similar considerations can be in part applied to the wall pressure profiles relating to campaign 3. It is immediately evident that the sonic pressure line is not encountered by the on-design curves in the constant area duct, indicating that the secondary flow does not reach the sonic condition, consistent with the compound-chocking theory. Also for this case the critical back pressure estimation exceeds the experimental measured value, the green numerical curve shows the case of $p_{out} = 152330$ Pa, while the experimental one is the case of $p_{out} = 137191$ Pa. Nevertheless, the numerical simulations show a remarkable agreement with the experimental data, despite the difference in critical back pressure.
For the remaining two campaigns, the over-expanded primary flow at the nozzle outlet in Campaign 7 reveals in a pronounced bump, caused by the formation of the Mach diamond. This effect is more evident for Campaign 6, due to the formation of the normal-curved shock. In the first on-design case of Campaign 7, an inflection near the diffuser inlet is observed, due to the unsteady shock formation (figure (4.3)).
Compared to the two previous campaigns, the transition from the on-design to the off-design regime is smoother (figure (4.9)), as the green curve deviates in a less pronounced way from the on-design cases, than in Campaigns 8 and 3.
As evidence from the performance figure (4.9), the estimated critical back pressure is almost the same when comparing numerical and experimental data, both green curves indicate the same p_{out} value.

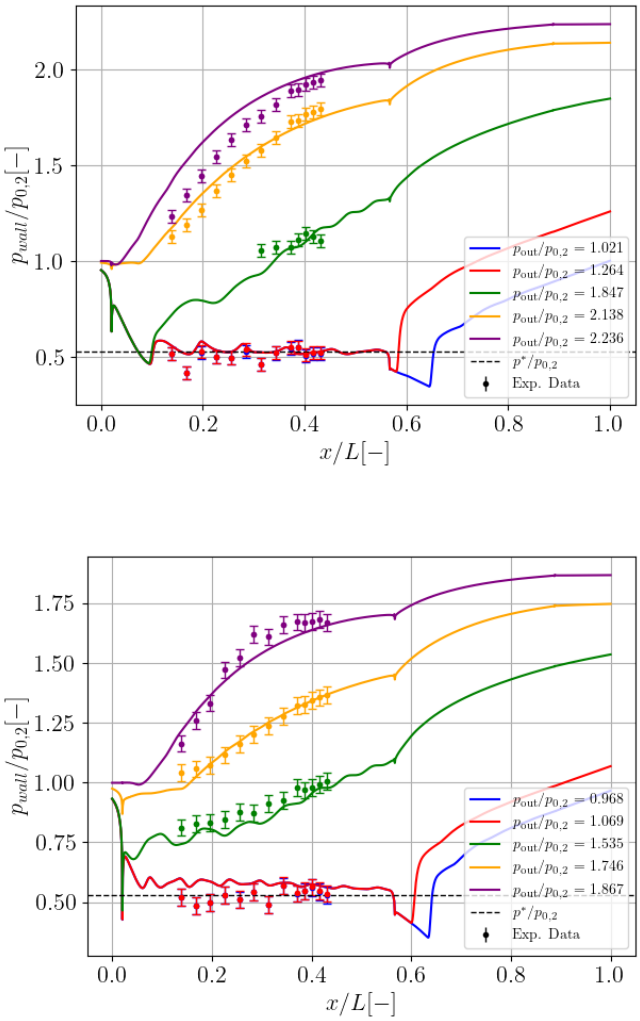

Figure 4.11: Wall pressure profiles: (top) Campaign 8, (bottom) Campaign 3

While oscillations due to successive shock-expansion wave interactions are present for pressure profile of the Campaign 7, they are mitigated for campaign. In particular, a strong pressure bump appears at the primary nozzle exit, due to the formation of normal-curved shock. The wall pressure profile graphs represent the internal flow behavior within the ejector, confirming the findings in the flow topology analysis, which is further supported by the Mach fields visualization. Additionally, the pressure profiles deriving from the numerical evaluation closely match the experimental measurements, and the reported findings show analogies with the results obtained and discussed by Brosteaux et al. (55).

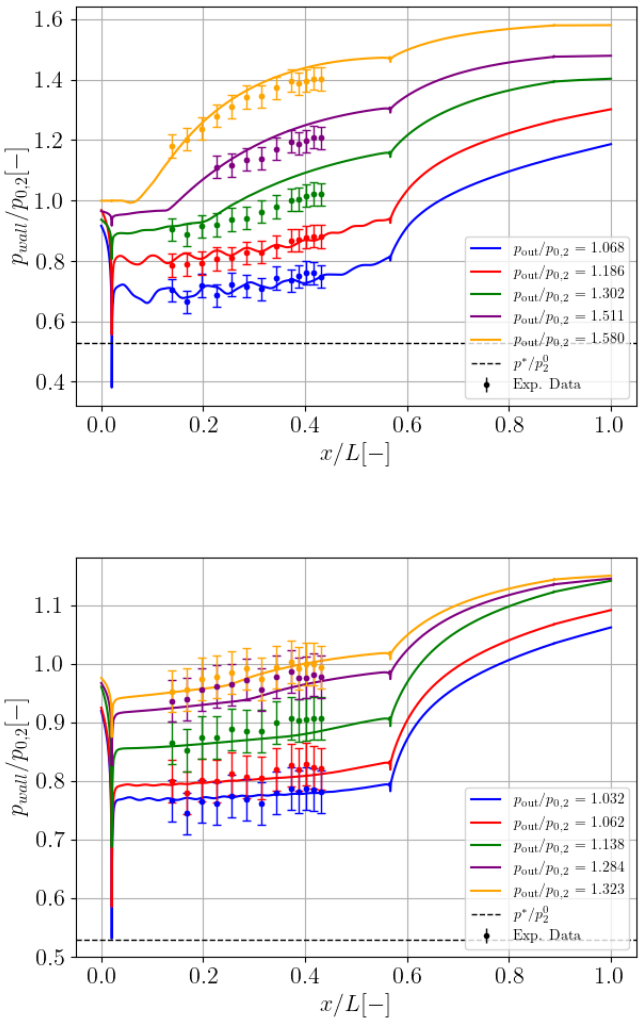

Figure 4.12: Wall pressure profiles: (top) Campaign 7, (bottom) Campaign 6

5

Conclusion and future work

The EJEMOD project is one of the pioneers for the complete characterization of the supersonic ejector internal flow, a rather complex task due to complex and variable phenomena involved.

This thesis supports the research started by Jan Van den Berghe and Professor Miguel Alfonso Mendez in developing low-order models (1D), complementing the evaluations conducted in Angiero's thesis (9). It should be noted that for this work a converging-diverging geometry for the primary nozzle is considered, unlike the simply convergent type used by previous works in the context of EJEMOD project, such as those by Angiero (9) and Schillaci et al. (8). The main objective is to performs as many simulations as possible, to provide a comprehensive numerical database for comparison with experimental campaigns. To achieve this, the initial question posed is whether a wall-modeled approach is satisfactory in order to characterize the internal flow within the ejector, or whether a wall-resolved approach is necessary, which would entail prohibitive computational cost.

Therefore, as initial step, the analysis focused on two different approaches for wall grid refinement, comparing the wall-modeled and the wall-resolved approach. An accurate mesh convergence study was conducted to asses the impact of each approach on the flow characterization, while also considering the computational cost associated to each approach. The results demonstrated that the wall-modeled approach guarantees excellent accuracy in representing internal flow of the ejector, accompanied by a substantial reduction in computational cost, leading to the selection of the medium wall-modeled mesh.

Based on the experimental database, four experimental campaigns characterized by different total pressure ratio at the inlet were selected, and numerical investigations were subsequently conducted using RANS simulations in the open-source software OpenFOAM v9, with the mesh implemented in 2D axisymmetric configuration.

5. CONCLUSION AND FUTURE WORK

A Python post-processing script was employed to convert the data from the .VTK to .npy format, allowing the extraction of flow variables required for analysis. In this regard, the flow topology and its variation with the operating conditions were analyzed, demonstrating how the Fabri-choking theory is suitable only to cases with high total pressure ratio at the inlet. On the other hand, compound-choking theory offers a more general but suitable framework for the characterization of the ejector flow, although it is subject to strong assumptions.

The presentation of ejector performance and pressure profiles allowed for a substantial comparison with experimental data, achieving a strong correlation. It was primarily observed that the numerical predictions tend to overestimate experimental ones, especially for on-design cases, and that the estimation of the critical p_b occurs at slightly higher values, especially for high total pressure ratio values at the inlet. As demonstrated by the simulations, the flow appears to be relatively insensitive to the variations of turbulence intensity (TI) at the inlet. Therefore, the observed discrepancy could be due to the inherent limitations of the RANS equations, which prove to be inadequate if applied to this complex problem, particularly in terms of turbulence modeling. Debroeyer et al. (20) showed that even through the use of LES simulations, it is not possible to achieve a perfect match with the experimental data. Future studies could focus on accurately estimating these effects, to achieve a precise prediction of the critical back pressure.

The study of the mixing between the two flows is a topic of primary importance but characterized by absolute complexity. Accurate mixing prediction is linked to understanding the internal flow behavior, to the final selection of the the mixing duct geometry, which could positively influence the ejector performance. The preliminary analysis provided in this study [4.2.2] follows a rather approximate approach, providing numerical data regarding the first interaction point between the boundary layer and shear layer. It has been demonstrated that the interaction point shifts progressively downstream as the total pressure ratio at the inlet decreases. Further and more precise studies could be beneficial for a comprehensive understanding of the mixing process.

Regarding the question of the "optimal" operating condition, the answer cannot be unequivocal, as it is highly dependent on the specific application of the ejector. Low total pressure ratios at the inlet define the highest entrainment ratios, though these are only sustained over a small back pressure ranges and require a longer mixing duct. High total pressure ratios at the inlet cause reduced ejector performance, but ensure grater stability over a wide range of back pressure, imposing fewer constraints on the mixing duct length.

References

[1] N. Baguet, G. Querinjean, Y. Bartosiewicz, and G. Winckelmans. *Experimental and numerical characterization of an axisymmetric supersonic ejector.* PhD thesis, École polytechnique de Louvain, 2023. iii, 5, 7, 9, 12, 18, 34, 53, 64, 72

[2] Z. Aidoun, K. Ameur, M. Falsafioon, and M. Badache. **Current advances in ejector modeling, experimentation and applications for refrigeration and heat pumps. Part 1: Single-phase ejectors.** *Inventions, 4(1), 15.*, 2019. iii, 8, 9, 15

[3] F. Mazzelli, A. B. Little, S. Garimella, and Y. Bartosiewicz. **Computational and experimental analysis of supersonic air ejector: Turbulence modeling and assessment of 3D effects.** *International Journal of Heat and Fluid Flow, 56, 305-316.*, 2015. iii, 10, 21, 72

[4] A. Bouhanguel. *Etude numérique et expérimentale de l'interaction entre deux écoulements compressibles dans un éjecteur supersonique.* PhD thesis, Doctoral dissertation, Université de Franche-Comté., 2013. iii, 11, 12

[5] O. Lamberts, P. Chatelain, and Y. Bartosiewicz. **Numerical and experimental evidence of the Fabri-choking in a supersonic ejector.** *International Journal of Heat and Fluid Flow, 69, 194-209.*, 1982. iii, 17, 18, 19, 20

[6] O. Lamberts, P. Chatelain, N. Bourgeois, and Y. Bartosiewicz. **The compound-choking theory as an explanation of the entrainment limitation in supersonic ejectors.** *Energy, 158, 524-536.*, 1982. iii, 16, 18, 19

[7] **EJEMOD project**, 2025. 1, 4

[8] E. Schillaci, C. Oliet, J. B. Vemula, M. Duponcheel, Y. Bartosiewicz, and P. Planquart. **Air ejector analysis in normal and abnormal modes,**

oriented to control purposes in aircraft systems. *European Conference for AeroSpace Sciences (EUCASS) (pp. 1-12)*, 2022. 1, 4, 79

[9] Angiero T. **Numerical and experimental comparison between a convergent and a convergent-divergent primary nozzle for a supersonic axisymmetric ejector.**, 2023. 1, 4, 41, 43, 51, 68, 79

[10] James R. Napier. **The ejector condenser for steam engines.** *Journal of the Franklin Institute*, 1869, 88(5), 357-IN6. 3

[11] Macia Li, R. Castilla, P. J. Gamez-Montero, S. Camacho, and E. Codina. **Numerical simulation of a supersonic ejector for vacuum generation with explicit and implicit solver in openfoam.** *Energies, 12(18), 3553.*, 2019. 3

[12] V. Lijo, H. D. Kim, S. Matsuo, and T. Setoguchi. **A study of the supersonic ejector–diffuser system with an inlet orifice.** *Aerospace Science and Technology, 23(1), 321-329.*, 2012. 3

[13] L. T. Chen. **A heat driven mobile refrigeration cycle analysis.** *Energy Conversion, 18(1), 25-29.*, 1978. 3

[14] S. Aphornratana. **Theoretical study of a steam-ejector refrigerator.** *International Energy Journal, 18(1).*, 1996. 4

[15] K. Chunnanond and S. Aphornratana. **Ejectors: applications in refrigeration technology.** *Renewable and sustainable energy reviews, 8(2), 129-155.*, 2004. 4

[16] J. G. Del Valle, J. Sierra-Pallares, P. G. Carrascal, and F. C. Ruiz. **An experimental and computational study of the flow pattern in a refrigerant ejector. Validation of turbulence models and real-gas effects.** *Applied Thermal Engineering, 89, 795-811.*, 2015. 4

[17] Y. Bartosiewicz, Z. Aidoun, P. Desevaux, and Y. Mercadier. **Numerical and experimental investigations on supersonic ejectors.** *International Journal of Heat and Fluid Flow, 26(1), 56-70.*, 2005. 6, 20

[18] J.H. Keenan, E.P. Neumann, and F. Lustwerk. **An investigation of ejector design by analysis and experiment.** *J. Appl. Mech., 72, 299–309.*, 1950. 6

[19] V. Kumar, S. K. Yadav, and S. Ram. **A comprehensive studies on constant area mixing (CAM) and constant pressure mixing (CPM) Ejectors: A review.** *Materials Today: Proceedings, 69, 513-518.*, 2022. 6

[20] R. Debroeyer, T. Toulorge, M. Rasquin, G. Winckelmans, and Y. Bartosiewicz. **Analysis of entrainment and mixing in a supersonic air ejector using large-eddy simulation.** *Available at SSRN 4877056*, 2024. 7, 80

[21] O. Lamberts, P. Chatelain, and Y. Bartosiewicz. **New methods for analyzing transport phenomena in supersonic ejectors.** *International Journal of Heat and Fluid Flow, 64, 23-40.*, 2017. 7

[22] T. Sriveerakul, S. Aphornratana, and K. Chunnanond. **Performance prediction of steam ejector using computational fluid dynamics: Part 1. Validation of the CFD results.** *International Journal of Thermal Sciences, 46(8), 812-822.*, 2007. 9

[23] K. MATSUO, K. Sasaguchi, Y. KIYOTOKI, and H. MOCHIZUKI. **Investigation of supersonic air ejectors: Part 2, effects of throat-area-ratio on ejector performance.** *Bulletin of JSME, 25(210), 1898-1905.*, 1982. 12, 13, 14

[24] J. Fabri and R. Siestrunck. **Supersonic air ejectors.** *Advances in applied mechanics, 5, 1-34.*, 1958. 13, 16

[25] L. Crocco. **One-dimensional treatment of steady gas dynamics.** *Fundamentals of gas dynamics, 3, 105.*, 1958. 13

[26] K. Matsuo, Y. Miyazato, and H. D. Kim. **Shock train and pseudo-shock phenomena in internal gas flows.** *Progress in aerospace sciences, 35(1), 33-100.*, 1999. 13, 14

[27] A. Weiss, A. Grzona, and H. Olivier. **Behavior of shock trains in a diverging duct.** *Experiments in fluids, 49, 355-365.*, 2010. 14

[28] F. Gnani, H. Zare-Behtash, and K. Kontis. **Pseudo-shock waves and their interactions in high-speed intakes.** *Progress in Aerospace Sciences, 82, 36-56.*, 2016. 14

[29] B. J. Huang, J. M. Chang, C. P. Wang, and V. A. Petrenko. **A 1-D analysis of ejector performance.** *International journal of refrigeration, 22(5), 354-364.*, 1999. 16, 19

[30] A. Bernstein, W. H. Heiser, Hevenor, and Charles. **Compound-compressible nozzle flow.** 1967. 16, 17

[31] J. Van den Berghe, M. A. Mendez, and Y. Bartosiewicz. **An extension of the compound flow theory with friction between the streams and at the wall.** *Journal of Fluid Mechanics, 1000, A85.*, 2024. 18, 26, 76

[32] F. R. Menter. **Two-equation eddy-viscosity turbulence models for engineering applications.** *AIAA journal, 32(8), 1598-1605.*, 1994. 20

[33] G. Besagni, N. Cristiani, L. Croci, G. R. Guédon, and F. Inzoli. **Computational fluid-dynamics modelling of supersonic ejectors: Screening of modelling approaches, comprehensive validation and assessment of ejector component efficiencies.** *Applied Thermal Engineering, 186, 116431.*, 2021. 21, 22

[34] G. Besagni and F. Inzoli. **Computational fluid-dynamics modeling of supersonic ejectors: Screening of turbulence modeling approaches.** *Applied Thermal Engineering, 117, 122-144.*, 2017. 22

[35] F. De Vanna, M. Cogo, M. Bernardini, F. Picano, and E. Benini. **Unified wall-resolved and wall-modeled method for large-eddy simulations of compressible wall-bounded flows.** *Physical Review Fluids, 6(3), 034614.*, 2021. 22

[36] S. Croquer, S. Poncet, and Z. Aidoun. **Turbulence modeling of a single-phase R134a supersonic ejector. Part 1: Numerical benchmark.** *International journal of refrigeration, 61, 140-152.*, 2016. 22

[37] Y. Han, X. Wang, H. Sun, G. Zhang, L. Guo, and J. Tu. **CFD simulation on the boundary layer separation in the steam ejector and its influence on the pumping performance.** *Energy, 167, 469-483.*, 2019. 22

[38] OpenFOAM contributors. **OpenFOAM guide/Finite volume method (OpenFOAM)**, 2010. 25

[39] OpenFOAM contributors. **OpenFOAM**, 2025. 25

[40] A. Kurganov and E. Tadmor. **New high-resolution central schemes for nonlinear conservation laws and convection–diffusion equations.** *Journal of computational physics, 160(1), 241-282.*, 2000. 26, 36

[41] B. Zang, U. S. Vevek, H. D. Lim, X. Wei, and T. H. New. **An assessment of OpenFOAM solver on RANS simulations of round supersonic free jets.** *Journal of computational science, 28, 18-31.*, 2018. 26

[42] L. F. G. Marcantoni, J. P. Tamagno, and S. A. Elaskar. **High speed flow simulation using openfoam.** *Mecánica Computacional, 31(16), 2939-2959.*, 2012. 28, 37

[43] H. K. Versteeg. *An introduction to computational fluid dynamics the finite volume method, Second Edition.* Pearson Education India., 2007. 28, 41, 42

[44] GMSH contributors. **GMSH, A three-dimensional finite element mesh generator with built-in pre- and post-processing facilities**, 2025. 30

[45] C. Geuzaine and J. F. Remacle. **Gmsh: A 3-D finite element mesh generator with built-in pre-and post-processing facilities.** *International journal for numerical methods in engineering, 79(11), 1309-1331.*, 2009. 30

[46] openFOAM contributors. **openFOAM, 6.2 numerical schemes**, 2025. 36

[47] A. Kurganov, S. Noelle, and G. Petrova. **Semidiscrete central-upwind schemes for hyperbolic conservation laws and Hamilton–Jacobi equations.** *SIAM Journal on Scientific Computing, 23(3), 707-740.*, 2001. 36

[48] C. J. Greenshields, H. G. Weller, L. Gasparini, and J. M. Reese. **Implementation of semi-discrete, non-staggered central schemes in a colocated, polyhedral, finite volume framework, for high-speed viscous flows.** *International journal for numerical methods in fluids, 63(1), 1-21.*, 2010. 37

[49] OpenFOAM contributors. **OpenFOAM Thermophysical**, 2025. 37

[50] OpenFOAM contributors. **OpenFOAM Transport**, 2025. 38

[51] openFOAM contributors. **openFOAM, Boundary conditions, waveTransmissive**, 2025. 40

[52] openFOAM contributors. **openFOAM, kLowReWallFunction**, 2025. 41

[53] D. C. Wilcox. **Reassessment of the scale-determining equation for advanced turbulence models.** *AIAA journal, 26(11), 1299-1310.*, 1988. 42

[54] D. W. Bogdanoff. **Compressibility effects in turbulent shear layers.** *AIAA journal, 21(6), 926-927.*, 1983. 57

[55] L. Brosteaux, Q. Doucet, Y. Bartosiewicz, and G. Winckelmans. **Experimental characterization of an axisymmetric supersonic air ejector.**, 2023. 72, 77

Appendices

Appendix A

In this appendix the turbulent kinetic energy (k) and the static pressure (p) fields are presented for three cases: an on-design case, the transition from on-design to off-design and the off-design case. These fields were included to support the flow topology analysis.

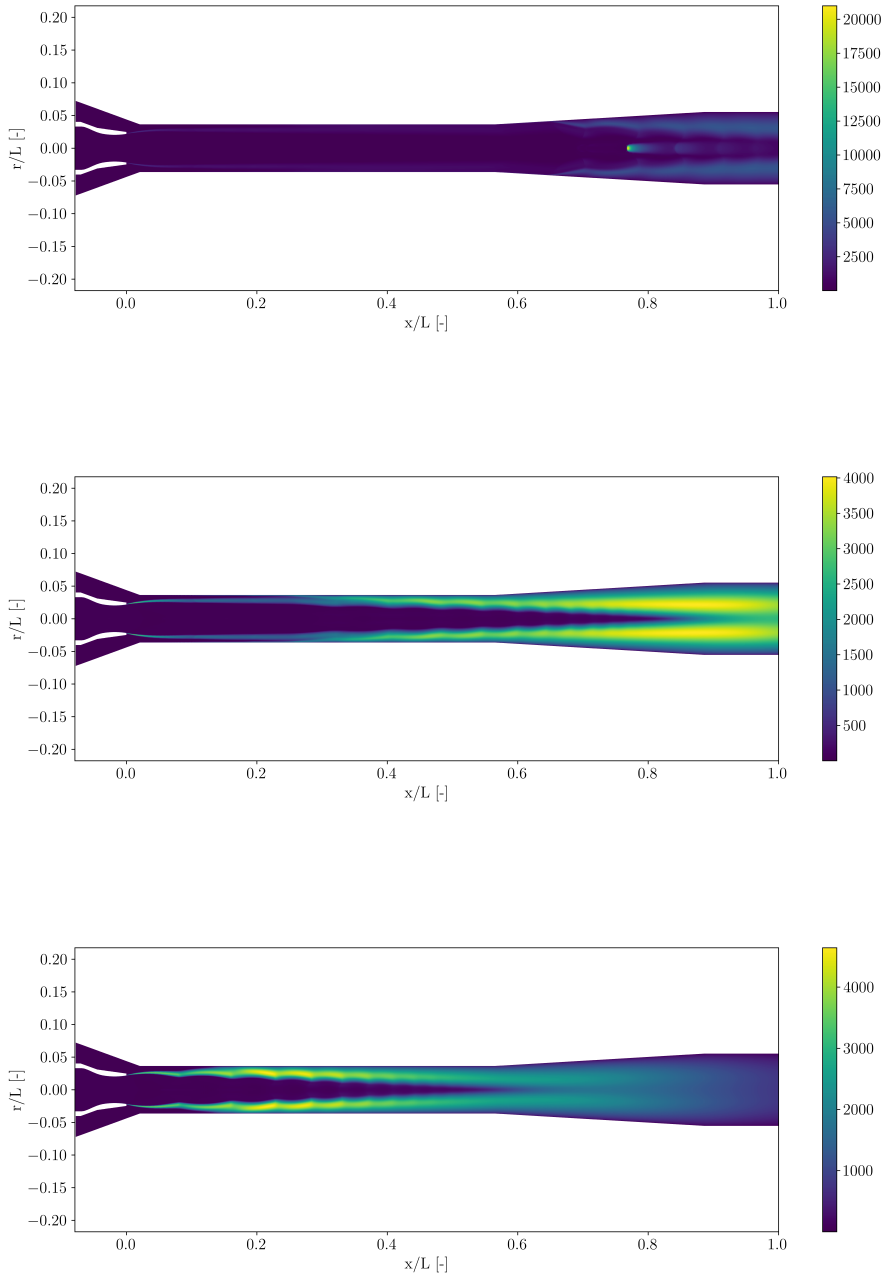

Figure 5.1: Turbulence kinetic energy (k), Campaign 8: (top) $p_{out} = 105000$ Pa, (middle) $p_{out} = 180000$ Pa, (bottom) $p_{out} = 210000$ Pa

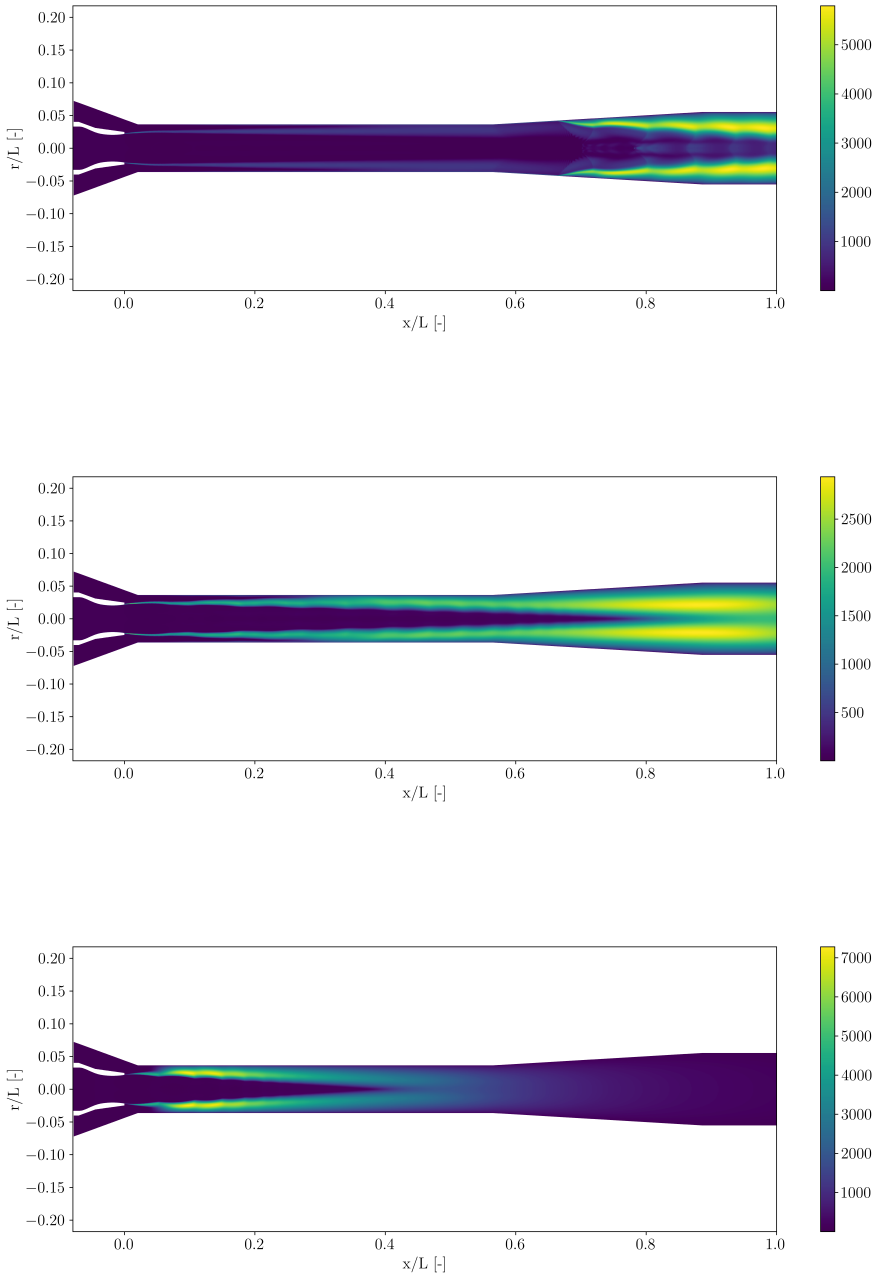

Figure 5.2: Turbulence kinetic energy (k) fields, Campaign 3: (top) p_{out} = 84235 Pa, (middle) p_{out} = 152330 Pa, (bottom) p_{out} = 185241 Pa

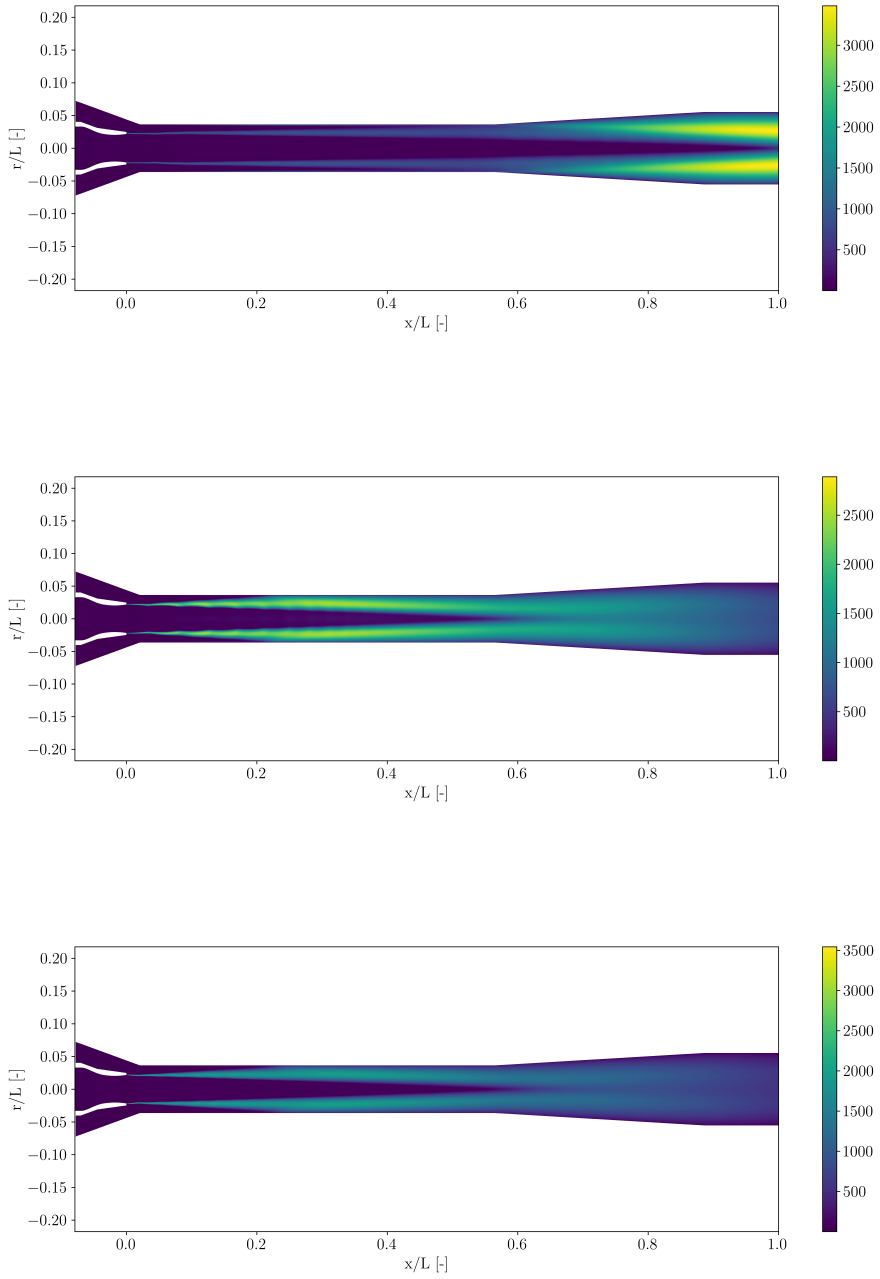

Figure 5.3: Turbulence kinetic energy (k) fields, Campaign 7: (top) p_{out} = 97895 Pa, (middle) p_{out} = 132498 Pa, (bottom) p_{out} = 144868 Pa

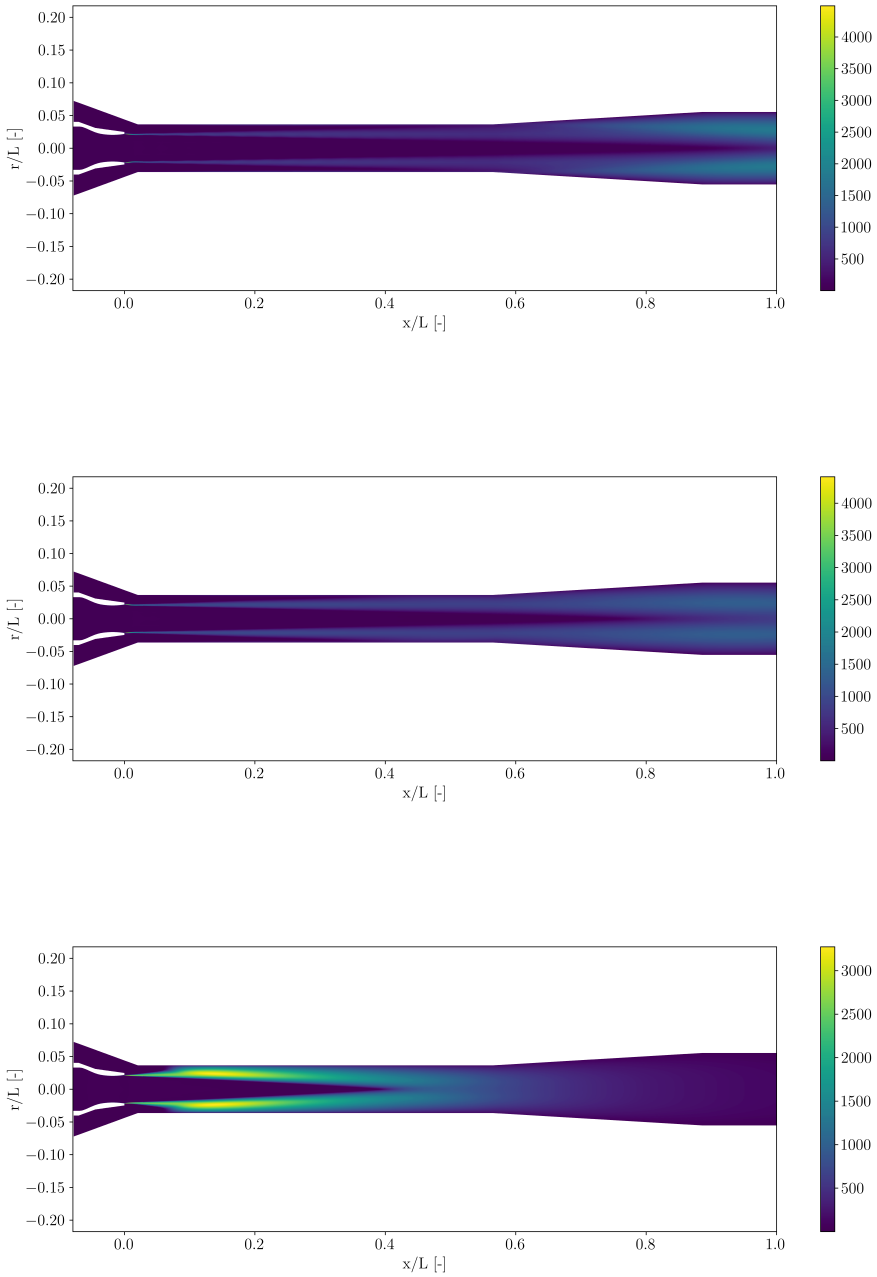

Figure 5.4: Turbulence kinetic energy (k) fields, Campaign 6: (top) p_{out} = 98472 Pa, (middle) p_{out} = 108581 Pa, (bottom) p_{out} = 126207 Pa

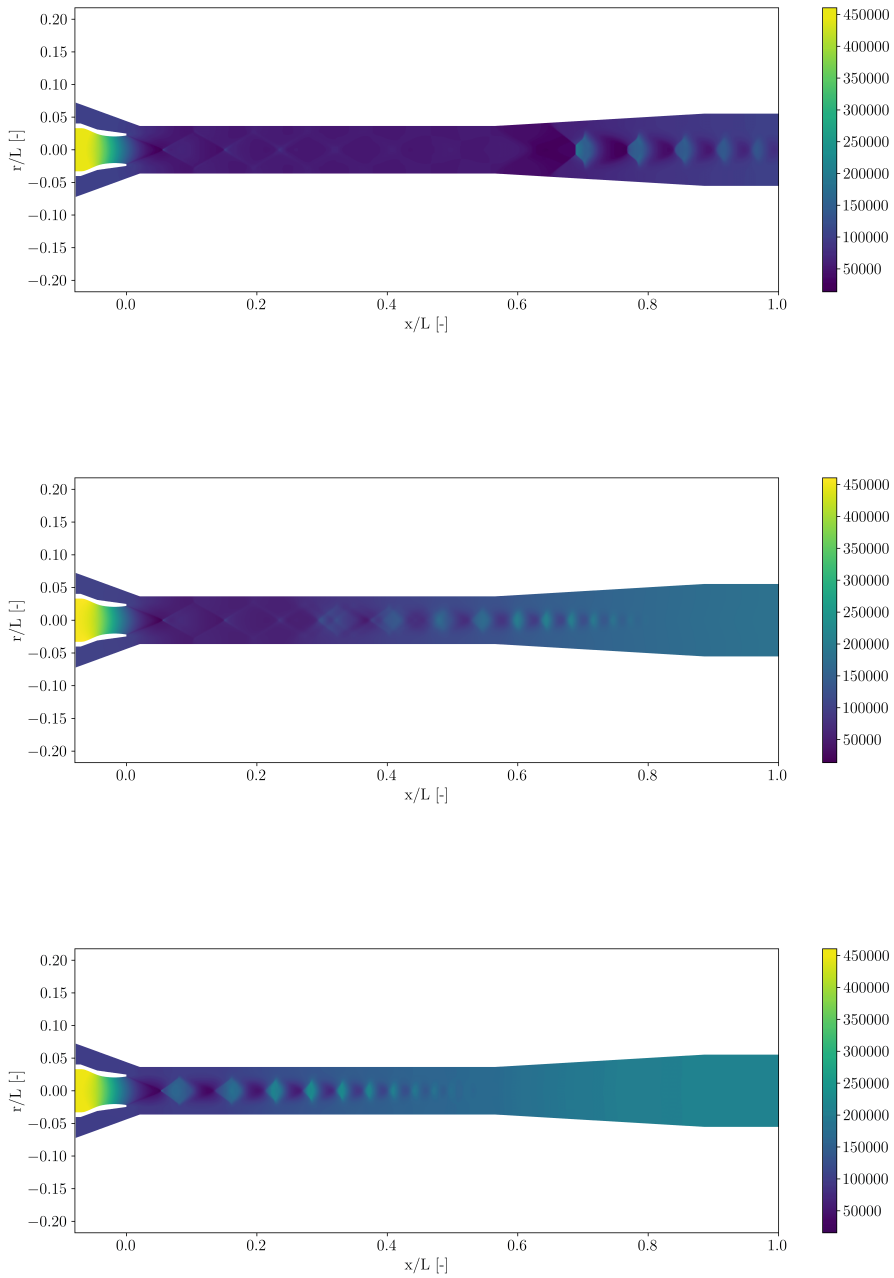

Figure 5.5: Static pressure (p) fields, Campaign 8: (top) $p_{out} = 105000$ Pa, (middle) $p_{out} = 180000$ Pa, (bottom) $p_{out} = 210000$ Pa

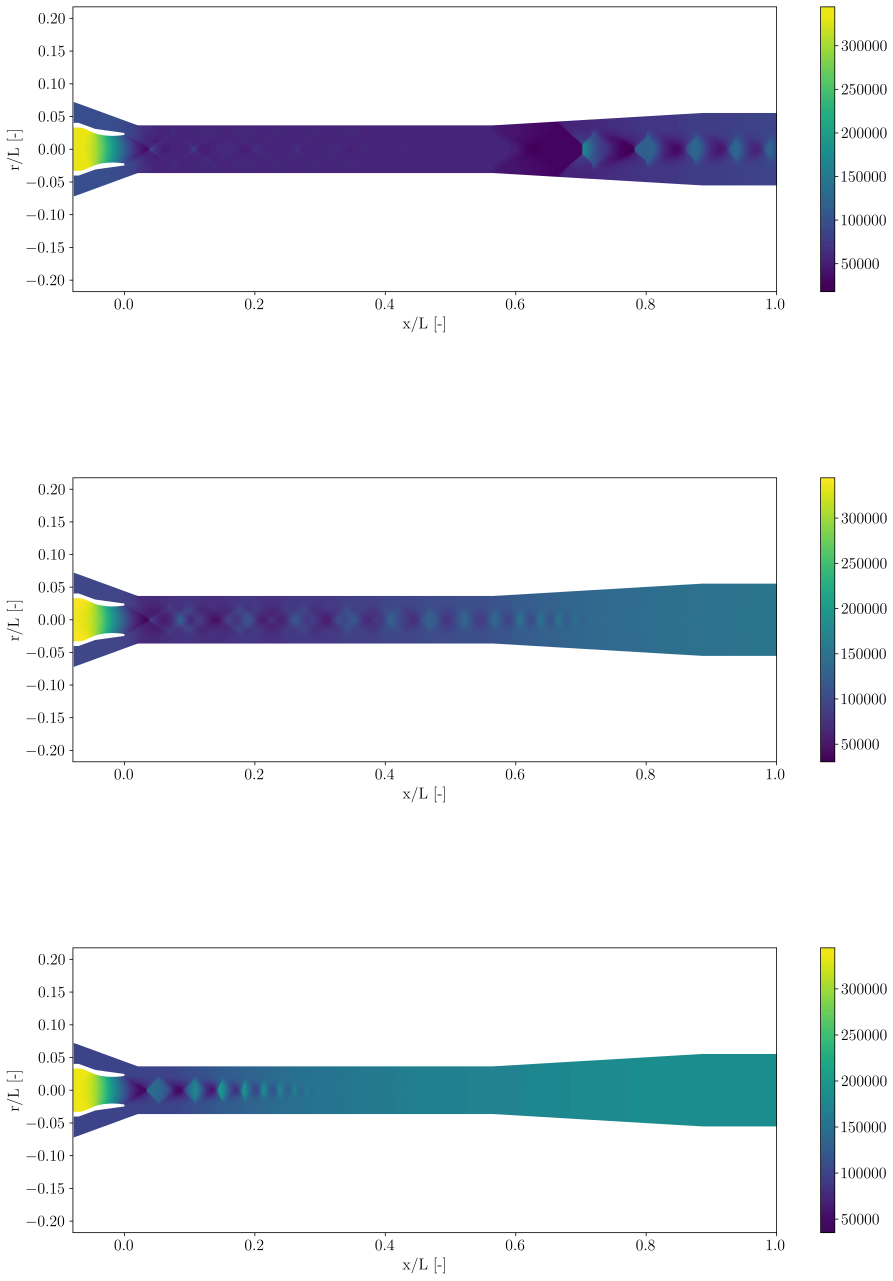

Figure 5.6: Static pressure (p) fields, Campaign 3: (top) $p_{out} = 84235$ Pa, (middle) $p_{out} = 152330$ Pa, (bottom) $p_{out} = 185241$ Pa

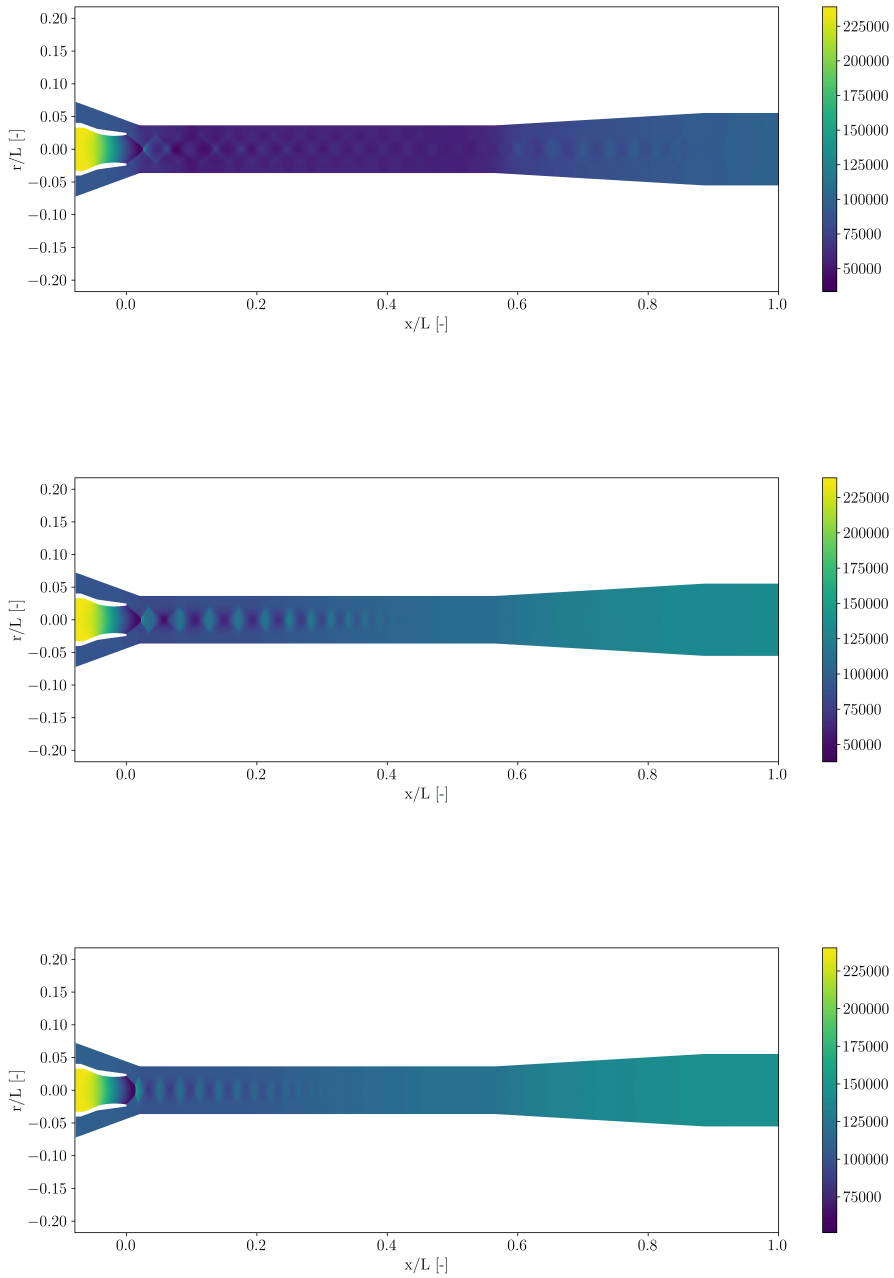

Figure 5.7: Static pressure (p) fields, Campaign 7: (top) $p_{out} = 97895$ Pa, (middle) $p_{out} = 132498$ Pa, (bottom) $p_{out} = 144868$ Pa

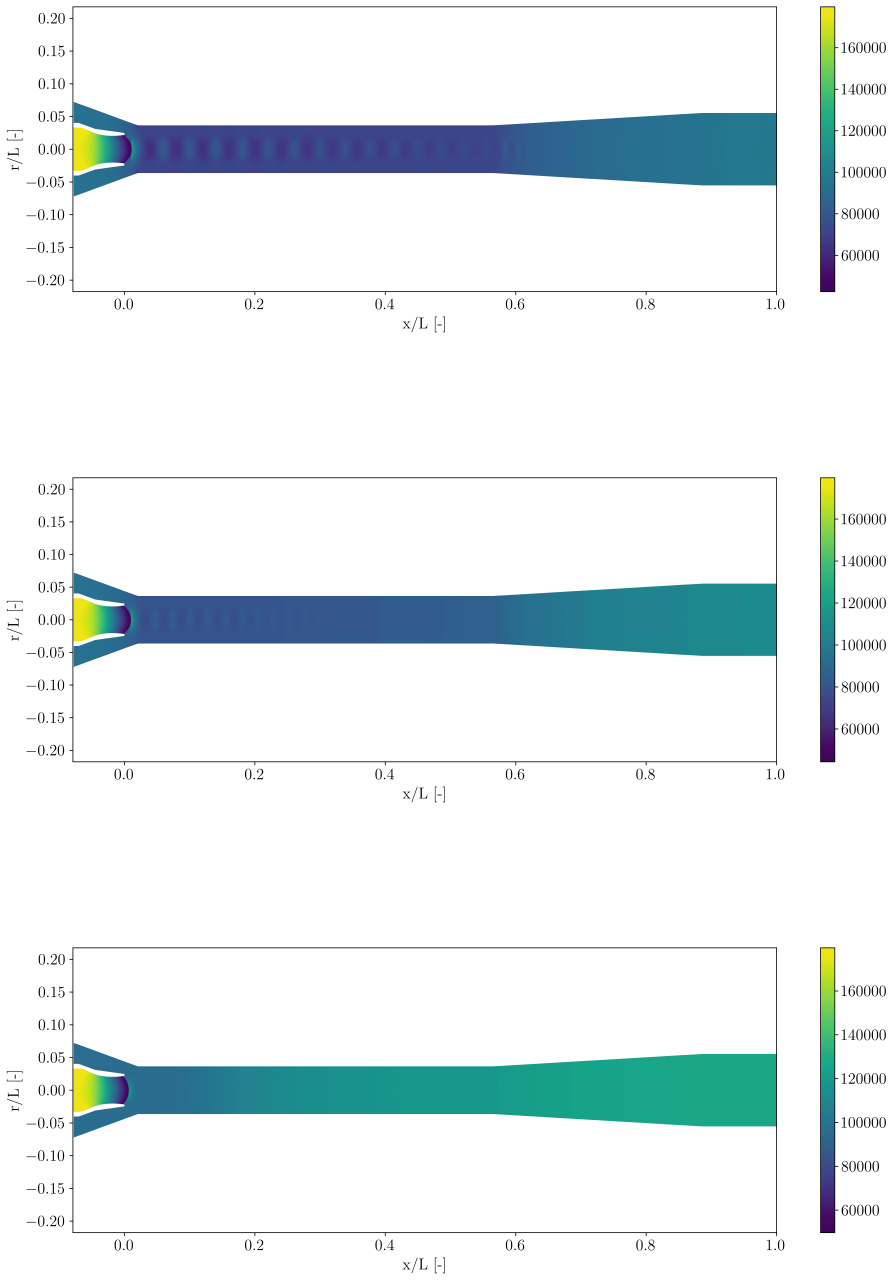

Figure 5.8: Static pressure (p) fields, Campaign 6: (top) $p_{out} = 98472$ Pa, (middle) $p_{out} = 108581$ Pa, (bottom) $p_{out} = 126207$ Pa

Appendix B

This appendix contains the boundary conditions of both numerical and experimental campaigns. The tables of the experimental conditions are shown first, displaying the total pressure values of the primary and secondary inlet, varying the back pressure at the ejector outlet. Subsequently, the inlet conditions of the numerical campaigns are reported, including bthe total temperature values for both nozzles.

Experimental campaigns

CAMPAIGN 3			
Test Number	$p_{0,1}$ **[Pa]**	$p_{0,2}$ **[Pa]**	p_{out} **[Pa]**
1	353130	98865	84235
2	354361	99392	85604
3	353115	99097	89990
4	352040	98987	96061
5	351952	99114	106073
6	353456	99326	114344
7	351826	99234	124199
8	351516	99927	137191
9	352240	100983	147543
10	351106	102827	152330
11	352249	103923	163591
12	351529	108561	166862
13	352092	115049	185241

Table 5.1: Boundary conditions for the experiments of the Campaign 3

CAMPAIGN 6			
Test Number	$p_{0,1}$ **[Pa]**	$p_{0,2}$ **[Pa]**	p_{out} **[Pa]**
1	184348	94214	98472
2	183166	95476	101260
3	184279	86439	104083
4	184039	98606	108581
5	184297	100240	111392
6	184290	102338	114794
7	184098	105254	119087
8	184147	108209	122434
9	184166	110734	126207
10	183579	114824	131673

Table 5.2: Boundary conditions for the experiments of the Campaign 6

CAMPAIGN 7			
Test Number	$p_{0,1}$ **[Pa]**	$p_{0,2}$ **[Pa]**	p_{out} **[Pa]**
1	243705	90953	94506
2	245289	91095	97895
3	244990	93024	108774
4	246082	96060	119345
5	246736	102486	132498
6	246482	106219	138516
7	246078	109460	144868
8	246078	113471	150085

Table 5.3: Boundary conditions for the experiments of the Campaign 7

CAMPAIGN 8			
Test Number	$p_{0,1}$ **[Pa]**	$p_{0,2}$ **[Pa]**	p_{out} **[Pa]**
1	472256	102852	69574
2	469671	102718	80574
3	471376	102902	106384
4	468327	102887	130611
5	471403	101759	164962
6	475527	104144	181173
7	478632	108796	210452
8	481936	112987	220116
9	497140	107374	228935

Table 5.4: Boundary conditions for the experiments of the Campaign 8

Numerical campaigns

CAMPAIGN 3					
Test Number	$p_{0,1}$ **[Pa]**	$p_{0,2}$ **[Pa]**	p_{out} **[Pa]**	$T_{0,1}$ **[K]**	$T_{0,2}$ **[K]**
1	352675	99243	84235	288	288
2	352675	99243	96061	288	288
3	352675	99243	106073	288	288
4	352675	99243	114344	288	288
5	352675	99243	124199	288	288
6	352675	99243	137191	288	288
7	352675	99243	147543	288	288
8	352675	99243	152330	288	288
9	352675	99243	163591	288	288
10	352675	99243	166862	288	288
11	352675	99243	173273	288	288
12	352675	99243	182526	288	288
13	352675	99243	185241	288	288
14	352675	99243	190062	288	288

Table 5.5: Boundary conditions for the numerical analysis, Campaign 3

CAMPAIGN 6					
Test Number	$p_{0,1}$ **[Pa]**	$p_{0,2}$ **[Pa]**	p_{out} **[Pa]**	$T_{0,1}$ **[K]**	$T_{0,2}$ **[K]**
1	183931	95376	98472	288	288
2	183931	95376	101260	288	288
3	183931	95376	104083	288	288
4	183931	95376	108581	288	288
5	183931	95376	111392	288	288
6	183931	95376	114794	288	288
7	183931	95376	119087	288	288
8	183931	95376	122434	288	288
9	183931	95376	126207	288	288
10	183931	95376	131673	288	288

Table 5.6: Boundary conditions for the numerical analysis, Campaign 6

CAMPAIGN 7					
Test Number	$p_{0,1}$ **[Pa]**	$p_{0,2}$ **[Pa]**	p_{out} **[Pa]**	$T_{0,1}$ **[K]**	$T_{0,2}$ **[K]**
1	244661	91691	94506	288	287
2	244661	91691	97895	288	287
3	244661	91691	108774	288	287
4	244661	91691	119345	288	287
5	244661	91691	132498	288	287
6	244661	91691	138516	288	287
7	244661	91691	144868	288	287
8	244661	91691	150085	288	287

Table 5.7: Boundary conditions for the numerical analysis, Campaign 7

CAMPAIGN 8					
Test Number	$p_{0,1}$ **[Pa]**	$p_{0,2}$ **[Pa]**	p_{out} **[Pa]**	$T_{0,1}$ **[K]**	$T_{0,2}$ **[K]**
1	471427	102877	80000	287	287
2	471427	102877	105000	287	287
3	471427	102877	130000	287	287
4	471427	102877	165000	287	287
5	471427	102877	180000	287	287
6	471427	102877	190000	287	287
7	471427	102877	200000	287	287
8	471427	102877	210000	287	287
9	471427	102877	220000	287	287
10	471427	102877	230000	287	287

Table 5.8: Boundary conditions for the numerical analysis, Campaign 8